THE HONG KONG
POLYTECHNIC UNIVERSITY
香港理工大學
Pao Yue-kong Library
包玉剛圖書館

Copyright Undertaking

This thesis is protected by copyright, with all rights reserved.

By reading and using the thesis, the reader understands and agrees to the following terms:

1. The reader will abide by the rules and legal ordinances governing copyright regarding the use of the thesis.
2. The reader will use the thesis for the purpose of research or private study only and not for distribution or further reproduction or any other purpose.
3. The reader agrees to indemnify and hold the University harmless from and against any loss, damage, cost, liability or expenses arising from copyright infringement or unauthorized usage.

IMPORTANT

If you have reasons to believe that any materials in this thesis are deemed not suitable to be distributed in this form, or a copyright owner having difficulty with the material being included in our database, please contact lbsys@polyu.edu.hk providing details. The Library will look into your claim and consider taking remedial action upon receipt of the written requests.

Pao Yue-kong Library, The Hong Kong Polytechnic University, Hung Hom, Kowloon, Hong Kong

http://www.lib.polyu.edu.hk

ULTRASENSITIVE BIODETECTION AND SONODYNAMIC THERAPY FOR PATHOGENIC AGENTS BASED ON LANTHANIDE-DOPED NANOMATERIALS

LAO XINYUE

PhD

The Hong Kong Polytechnic University

2025

The Hong Kong Polytechnic University

Department of Applied Physics

Ultrasensitive Biodetection and Sonodynamic Therapy for Pathogenic Agents Based on Lanthanide-Doped Nanomaterials

LAO Xinyue

A thesis submitted in partial fulfillment of the requirements for the degree of Doctor of Philosophy

August 2024

CERTIFICATE OF ORIGINALITY

I hereby declare that this thesis is my own work and that, to the best of my knowledge and belief, it reproduces no material previously published or written, nor material that has been accepted for the award of any other degree or diploma, except where due acknowledgement has been made in the text.

_____(Signed)

Lao Xinyue (Name of student)

Abstract

Outbreaks of pathogenic organisms including viruses and bacteria provide a formidable challenge to public healthcare systems. The early detection of infectious pathogens and the subsequent therapy are essential for preventing propagation. For the biodetection assay, FRET has been commonly used for biosensing as the luminescent intensity of fluorophore varies with the approach or separation of the energy pairs. Therefore, FRET biodetection assay based on upconversion nanoparticles (UCNPs) and gold nanoparticles is developed for the detection of viruses in this thesis. As for the therapy of the pathogens, sonodynamic therapy (SDT) has tremendous potential in preventing multidrug-resistant bacterial infections considering it is non-invasive and requires no antibiotic dependence, which can effectively solve the problem of bacterial resistance. Hence, an antibacterial application is conducted both in vitro and in vivo using Bi_2WO_6 nanosheets as sonosensitizer for sonodynamic therapy.

In the first part of the thesis, an ultrasensitive plasmon-enhanced fluorescence resonance energy transfer (FRET) biosensor based on core-shell upconversion nanoparticle (csUCNP) and gold nanoparticle (AuNP) for accurate detection of SARS-CoV-2 viral RNA is presented. In this biodetection assay, the Tm^{3+}/Er^{3+} co-doped csUCNP $NaGdF_4$:Yb/Tm@$NaYF_4$:Yb/Er acts as an energy donor and AuNP serves as an energy acceptor. The upconversion emission of Tm^{3+} and the design of the core-shell structure led to a simultaneous surface plasmon effect of AuNP. The localized surface plasmon resonance (LSPR) arising from collective oscillations of free electrons

significantly enhanced FRET efficiency between Er^{3+} and AuNP. The as-prepared biosensor obtained a limit of detection (LOD) as low as 750 aM, indicating that the integration of FRET and surface plasmon into one biodetection assay significantly boosted the sensitivity of the biosensor. In addition, samples extracted from clinical samples are also utilized to validate the effectiveness of the biosensor. Therefore, this innovative plasmon-enhanced FRET biosensor based on Tm^{3+}/Er^{3+} co-doped csUCNP may pave the way for rapid and accurate biodetection applications.

In the second section, 2-dimensional (2D) Bi_2WO_6 nanosheets (BWO NSs) were synthesized through the hydrothermal method as the sonosensitizer, and varying concentrations of Ytterbium ions were doped (BWO-x%Yb, x=1,2,5,10,20) to improve the sonodynamic activity. The Yb ions were verified to occupy the position of Bi by both calculation and XRD characterization. The reactive oxygen species (ROS) produced by BWO-x%Yb under ultrasound (US) irradiation were examined. It was shown that at a concentration of 10% Yb, the nanosheets generated the highest amount of ROS. ROS has the ability to cause oxidation of lipids in the bacterial cell membrane, resulting in the deterioration of membrane integrity. This can result in the release of intracellular substances and ultimately lead to cellular demise. In vitro experiments have verified that the BWO-10%Yb NSs are capable of eliminating both Methicillin-resistant *Staphylococcus aureus* (MRSA) and Escherichia coli (*E. coli*) through ROS generation. The RNA sequencing transcriptome analysis was conducted with MRSA to acquire further understanding of the biological mechanism of the sonodynamic

antimicrobial activities of BWO-10%Yb NSs.

In the third part of the thesis, the BWO-10%Yb NSs are combined with polyvinyl alcohol (PVA) hydrogel to improve biocapacity for further in vivo antibacterial applications. The resulting BWO-Yb-PVA hydrogel also showed remarkable efficacy in killing bacteria. In the in vivo test, the BWO-Yb-PVA hydrogel expedited the healing process of wounds infected with MRSA. Therefore, our work highlights a novel sonosensitizer for enhanced sonodynamic bacteria elimination and wound healing.

List of Publication

1. **Xinyue Lao**, Yuan Liu, Lihua Li, Menglin Song, Yingjin Ma, Mo Yang, Guanying Chen, and Jianhua Hao, “Plasmon-enhanced FRET biosensor based on Tm^{3+}/Er^{3+} co-doped core-shell upconversion nanoparticles for ultrasensitive virus detection”, Aggregate 5, e448 (2024).
2. **Xinyue Lao**, Qianqian Bai, Yifei Zhao, Xinyi Dai, Xiao Han, Yuan Liu, and Jianhua Hao, “Enhanced Sonodynamic Bacterial Elimination and Wound Healing Therapy Based on Lanthanide Ion Doped Bi_2WO_6 Nanosheets and Hydrogel Platform”. (Submitted to Advanced Functional Materials, under revision)
3. Qianqian Bai, **Xinyue Lao**, Sing-Yi Pang, Yifei Zhao, Yuan Liu, Xiao Yu Tian, Jianhua Hao*, “Plaque-Targeted Delivery of Fluoride-Free MXene Nanozyme for Alleviating Atherosclerosis via Sonocatalytic Therapy” (Submitted to Advanced Materials, under revision)
4. Yuan Liu, **Xinyue Lao**, Man-Chung Wong, Menglin Song, Huang Lai, Pui Wang, Yingjin Ma, Lihua Li, Mo Yang, Honglin Chen, and Jianhua Hao, "Microfluidic chip-assisted upconversion luminescence biosensing platform for point-of-care virus diagnostics”, Adv. Healthcare Mater. DOI: 10.1002/adhm.202303897 (2024) (Featured on the back cover and also appears in: Hot Topic: Microfluidics).

5. Yuan Liu, Man-Chung Wong, **Xinyue Lao**, Menglin Song, Yifei Zhao, Yingjin Ma, Qianqian Bai, Jianhua Hao*, "Intelligent Point-of-care Biosensing Platform Based on Luminescent Nanoparticles and Microfluidic Biochip with Machine Vision Algorithm Analysis" (Submitted to Nano-micro Letters, under revision)
6. Lihua Li, Yao Lu, **Xinyue Lao**, Sin-Yi Pang, Menglin Song, Man-Chung Wong, Feng Wang, Mo Yang, and Jianhua Hao, "A magnetic-enhanced FRET biosensor for simultaneous detection of multiple antibodies", Smart Materials in Medicine 5, 196 (2024).
7. Yingjin Ma, Menglin Song, Lihua Li, **Xinyue Lao**, Yuan Liu, Man-chung Wong, Mo Yang, Honglin Chen, and Jianhua Hao, "Attomolar-level detection of respiratory virus long-chain oligonucleotides based on FRET biosensor with upconversion nanoparticles and Au-Au dimer", Biosensors and Bioelectronics, 243, 115778 (2024).
8. Yi Wei, Menglin Song, Lihua Li, Yingjin Ma, **Xinyue Lao**, Yuan Liu, Guogang Li, and Jianhua Hao, "Enhanced long-lasting luminescence nanorods for ultrasensitive detection of SARS-CoV-2 N protein", Sci. China Mater. 68, 253 (2025)
9. Menglin Song, Man-Chung Wong, Lihua Li, Feng Guo, Yuan Liu, Yingjing Ma, **Xinyue Lao**, Pui Wang, Honglin Chen, Mo Yang, and Jianhua Hao, "Rapid point-of-care detection of SARS-CoV-2 RNA with smartphone-based upconversion luminescence diagnostics", Biosensors and Bioelectronics 222, 114987 (2023).

10. Qin Zhang, Chuanqi Li, Bohan Yin, Jiaxiang Yan, Yutian Gu, Yingying Huang, Jiareng Chen, **Xinyue Lao**, Jianhua Hao, Changqing Yi, Yi Zhou, James Chung Wai Cheung, Siu Hong Dexter Wong, Mo Yang, “A biomimetic upconversion nanoreactors for near-infrared driven H2 release to inhibit tauopathy in Alzheimer's disease therapy”, Bioactive Materials, 42, 165-177 (2024).
11. Yingjin Ma, Menglin Song, Lihua Li, **Xinyue Lao**, Man-Chung Wong, and Jianhua Hao, "Advances in upconversion luminescence nanomaterial-based biosensor for virus diagnosis", Exploration 2, 20210216 (2022).
12. Lihua Li, Menglin Song, **Xinyue Lao**, Sin-Yi Pang, Yuan Liu, Man-Chung Wong, Yingjin Ma, Mo Yang, and Jianhua Hao, “Rapid and ultrasensitive detection of SARS-CoV-2 spike protein based on upconversion luminescence biosensor for COVID-19 point-of-care diagnostics”, Materials & Design 223, 111263 (2022).

Acknowledgements

First and foremost, my deepest appreciation extends to my supervisor, Prof. Hao Jianhua, for providing an invaluable chance to complete my doctoral study and offering invaluable guidance during my study. Thanks to his professionalism and kindness, I was able to pursue my research in an atmosphere that encourages creativity and open-mindedness. His profound insight and inspiring ideas provide important guidance in my research.

I would like to express my thanks to my group mates, Dr. Liu Yuan, Dr. Bai Qianqian, Ms. Ma Yingjin, Dr. Pang Sing-Yi, Dr. Han Xiao, Dr. Dai Xingyi, Mr. Zhao Yifei, Dr. Song Menglin, Dr. Guo Feng, Dr. Wong Man-Chung, and Dr. Liu Duanzijing for their friendship and valuable support in my experiment. I also want to thank the technicians and colleagues at the Hong Kong Polytechnic University Shenzhen Research Institutes for their support in my experiments.

I would also like to thank my friends, Ms. Guo Xiaohui, Dr. Zhou Mo, and Dr. Zhang Xiao, for their company. I am grateful for their presence in my life.

Lastly, I would like to express my gratitude to my parents and my brother for their unconditional support of my decision. Their unwavering love and consideration contributed to my success in accomplishing my doctoral study.

Table of Contents

List of Figures

List of Tables

Chapter 1 Introduction

1.1 Infectious Pathogens

Infectious diseases are medical conditions resulting from the presence of pathogenic microorganisms, including viruses, bacteria, fungi, and parasites [1]. The pathogenic microorganisms can be spread between organisms by direct or indirect contact, resulting in a range of fatal illnesses [2-4]. Despite notable progress in preventive and therapeutic interventions, infectious illnesses persist and present an ongoing risk to public health and the global economy [5, 6].

1.1.1 Infectious Virus

The worldwide pandemic coronavirus disease 2019 (COVID-19) caused by the severe acute respiratory syndrome coronavirus 2 (SARS-CoV-2) claimed the lives of millions of people and caused hundreds of millions of total cases all over the world [7-9]. The pandemic again emphasizes the significant negative impact of the virus on the lives of individuals as well as the development of the global economy [10]. In addition, other viruses, such as norovirus [11], Ebola virus [12, 13], human immunodeficiency virus (HIV) [14], and Middle East respiratory syndrome (MERS) coronavirus [15], also spread widely and cause fatal illnesses[16]. Viral infections lead to immune system dysfunction and inflammation, they can also be associated with serious sequelae such as cardiovascular diseases and malignancies [17, 18]. In the fight against infectious virus diseases, early and accurate diagnosis is the most effective way to break the chain of

transmission and mitigate the impacts of these diseases [19].

1.1.2 Infectious Bacteria

Infections of bacteria are prevalent in humans and a serious threat to human health because they can cause a variety of infectious diseases, ranging from skin infections to those that impact internal organs, or even brains [20-24]. Penicillin is the first antibiotic discovered by British microbiologist Alexander Fleming in 1928 [25], and since then antibiotics have been considered for the clinical prevention and treatment of bacterial infections [26, 27]. Nevertheless, the worldwide community is increasingly alarmed by the rise of multidrug-resistant (MDR) bacteria as a result of the overuse and misuse of antibiotics [28, 29]. Families of antibiotic-resistant bacterial pathogens include *mycobacterium tuberculosis*, *Salmonella*, *Neisseria gonorrhoeae*, *Pseudomonas aeruginosa*, and *Staphylococcus aureus* (*S. aureus*) [30]. Consequently, it is essential to create antimicrobial therapies that combat bacterial infections without fostering MDR bacteria.

The WHO announced the top ten threats to global health in 2019, in which infectious pathogens and antimicrobial resistance are both included [31]. Thus, early and accurate diagnostics and a new generation of treatments against infectious pathogens are essential for the global clinical system.

1.2 Detection of Infectious Pathogens

1.2.1 Conventional Detection Methods

Current reliable and accessible techniques for virus detection and analysis are

reverse transcription polymerase chain reaction (RT–PCR) and immunoassay methods (IA) [32]. By amplifying the viral gene sequences, RT-PCR is considered the gold standard for any pathogen detection, with a response time of around 2 h [33, 34]. However, several downsides of RT-PCR also exist, such as the requirement for a constant reagent supplement such as primers and polymerase enzymes, highly specialized and high-cost equipment, trained personnel for sample analysis, limited capacity, and time-consuming.

The enzyme-linked immunosorbent assays (ELISA) and lateral flow immunoassays (LFA) are currently used immunological tests for the detection of viral infection [35-38]. LFAs are a preferred method for on-site viral detection and controlling the spread of infectious diseases owing to their cheap cost, lack of need for instruments, and convenience of use [39]. LFAs utilize virus-specific biorecognition components, such as antibodies, to quickly identify antigens and provide speedy results. Nevertheless, the limited precision, sensitivity, and specificity caused by cross-reactivity with comparable pathogens are impeding progress [40]. Therefore, currently available direct antigen tests and serological assays cannot replace RT-PCR testing, but they may be used as additional diagnostic tools. The presence of these constraining variables, together with concerns over the supply chain and discrepancies in test findings, prompted the exploration of alternative technologies such as biosensors. These biosensors have the ability to address the limitations of traditional diagnostic techniques for viral infectious illnesses.

Detection and diagnosis of viruses at an early stage are essential for minimizing the threat caused by viruses. Hence, it is imperative to develop new biosensing

technologies using cutting-edge materials to identify viruses and other biomarkers associated with viral pathogens. This would enable us to effectively manage and prevent future pandemics caused by viral infectious illnesses.

1.2.2 Biosensors Based on Nanomaterials

Recently, biosensors based on nanomaterials for the detection of viruses and bacteria have been widely studied, including colorimetric biosensors, electrochemical biosensors, SERS-based biosensors, and fluorescent biosensors [41]. Nanomaterials such as metal nanomaterials, carbon-based nanomaterials, quantum dots, and upconversion nanoparticles could be modified with antibodies, nucleic acid, and peptide to realize selective detection (Figure 1-1).

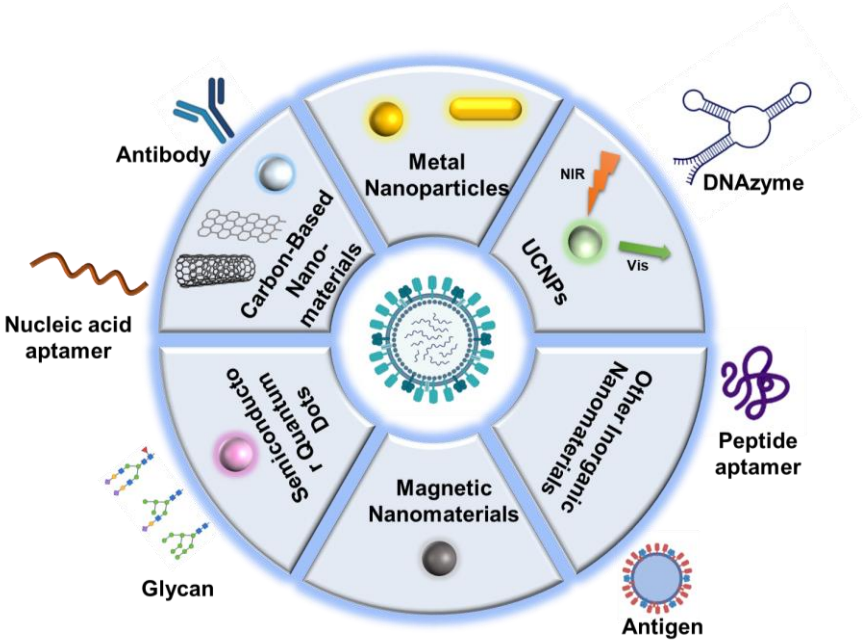

Figure 1-1 Schematic illustration of biosensors based on nanomaterials for the detection of viruses.

Colorimetric biosensors are low-cost and rapid methods for the detection of infectious pathogens, capable of producing signals that are visible to the naked eye [42]. Unfortunately, the constrained sensitivity of conventional colorimetric biosensors imposes limitations on their use across various situations. AuNPs are a great candidate material for colorimetric biosensors due to their unique surface plasmon resonance (SPR) properties. The absorption of AuNPs exhibits variability in the range of visible light based on their size and shape. Recently, sensitive colorimetric biosensors employing AuNPs as probes have been developed. Moitra et al. developed an AuNPs-based colorimetric biosensor for the detection of SARS-CoV-2 nucleic acids by naked-eyes (Figure 1-2) [43]. In this biodetection assay, the AuNPs are capped with thiol-modified antisense oligonucleotides that can specifically target to the Nucleocapsid gene (N-gene) of SARS-CoV-2. In the presence of the target N-gene sequence, the AuNPs agglomerate, causing the colour of the solution changed from violet to blue. Afterwards, the RNase H treatment cleaves the RNA sequence from the DNA-RNA hybrid, resulting in the formation of visible precipitate owing to the further clumping of the AuNPs. The total detection time is less than 10 min from the RNA isolation and the LOD of the biosensor is 0.18 ng/μL with a detection range of 0.2–3 ng/μL. The selectivity of this assay is also assessed using viral RNA from Middle East respiratory syndrome coronavirus (MERS-CoV). This colorimetric biosensor enables rapid detection of SARS-CoV-2 RNA without amplification.

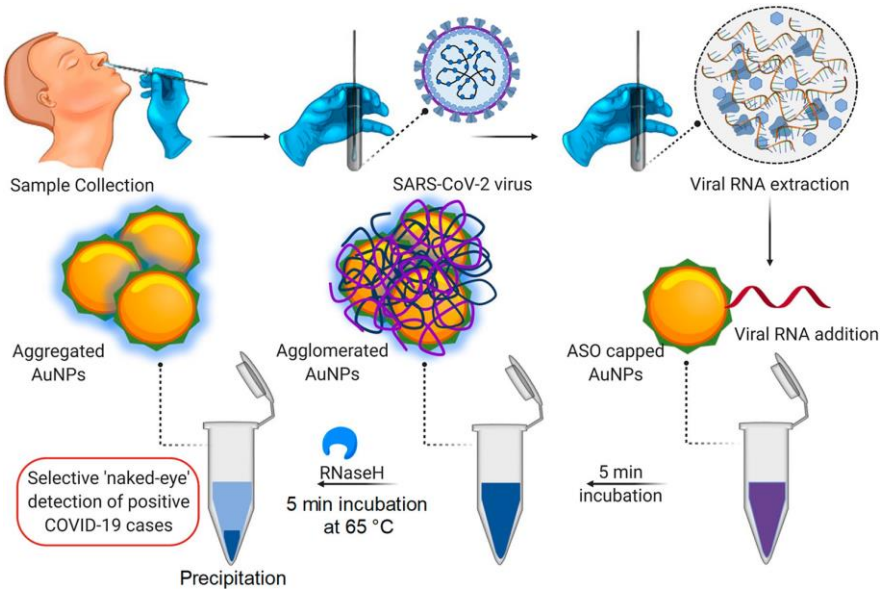

Figure 1-2 Illustration of the detection of SARS-Cov-2 viral RNA using ASO-capped AuNPs [43].

The electrochemical biosensor is another sensitive platform for detecting infectious pathogens, which may convert the target substance into detectable electrochemical signals, including potential, current, or impedance [44, 45]. An electrochemical immunosensor based on functionalized multiwall carbon nanotube-chitosan was reported for the detection of uropathogenic *E. coli* [46]. The glassy carbon electrode is coated with the composite and then modified with thionine dye for rapid detection of uropathogenic *E. coli*. Uropathogenic E. coli is immobilized using chitosan, then treated with polyclonal antibody and horseradish peroxidase (HRP) labeled secondary antibody. The reduction of H_2O_2 on the electrode is facilitated by using thionine as the mediator. C The concentration of uropathogenic *E. coli* is determined using the cyclic voltammetry technique. The biosensor exhibited excellent linearity in a range of

10^2–10^9 CFU of uropathogenic *E. coli* mL^{-1} with a current sensitivity of 7.162 μA $[\log(CFU\ mL^{-1})]^{-1}$, as well as good specificity.

Surface enhanced Raman scattering (SERS) is another kind of sensitive detection method based on noble metal structures [47-49]. When the reporter molecules are absorbed on the surface of a SERS substrate, the intensity of Raman scattering signals can be amplified by 10^6–10^{14}, enabling an ultrasensitive biosensing [50]. A self-assembly SERS-immune substrate is reported for the detection of SARS-CoV-2 virus[47]. The substrate was produced using a unique oil/water/oil (O/W/O) three-phase liquid-liquid interfaces technique, resulting in the creation of two layers of compact and homogenous gold nanoparticle films, which guarantees the consistency and sensitivity of the SERS immunoassay. The SERS-based biosensor successfully identified the presence of the SARS-CoV-2 spike protein at concentrations of 0.77 fg mL^{-1} in PBS and 6.07 fg mL^{-1} in untreated saliva. The SERS-based biosensor demonstrated exceptional specificity and sensitivity for the SARS-CoV-2 virus, requiring no sample preparation. This makes it a promising option for the early detection of COVID-19.

1.3 FRET Biosensors Based on Lanthanide-Doped Upconversion Nanoparticles

1.3.1 FRET Biosensing Systems

Fluorescence resonance energy transfer (FRET) is a nonradiative energy transfer process that is highly related to the distance between fluorophore molecules. During the FRET process, the excited donor fluorophore transferred energy to the acceptor

fluorophore via the intermolecular non-radiative dipole-dipole coupling. The transfer occurs without the emission or absorption of a photon. The effectiveness of energy transfer decreases exponentially with the sixth power of the distance (within 1-10 nm) between the donor and acceptor fluorophore molecules. This makes FRET very sensitive to even small changes in detachment. The Forster equation is often used to quantify the efficiency of the energy transfer process:

$$E = \frac{1}{1 + \left(\frac{R}{R_0}\right)^6}$$

in which R is the distance between the donor and acceptor fluorophore, whereas R_0 represents the specific distance at which there is a 50% energy transfer efficiency. The energy transfer in FRET process is depicted in Figure 1-3. Therefore, FRET is very valuable in biosensing to measure the changes in distance of fluorescent probes at the nanoscale.

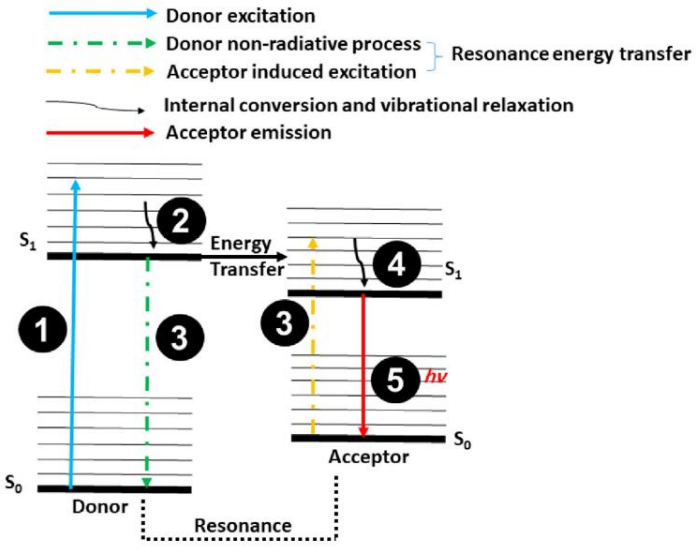

Figure 1-3 Schematic illustration of fluorescence resonance energy transfer process [51].

1.3.2 Lanthanide Doped Upconversion Nanoparticles

Lanthanide (Ln^{3+}) activated upconversion nanoparticles (UCNPs) are typically composed of an optically inert inorganic host matrix doped with optically active trivalent lanthanide ions and able to convert the near-infrared (NIR) simulation with long wavelengths into short wavelengths emission in the UV or visible range, as shown in Figure 1-4 [52]. Compared with conventional fluorophores, UCNPs exhibit superior photoluminescence properties, including sharp emission spectrum, low auto-fluorescence, high resistance to photo-bleaching, photo-thermal stability, and exceptional biocompatibility. Moreover, the emission wavelengths of UCNPs can be adjusted by changing the Ln^{3+} dopants, including Er^{3+}, Tm^{3+}, or Ho^{3+}, or the irradiation wavelengths [53]. The tunable emission properties and novel luminescence characteristics of UCNPs provide significant prospects for the development of new probes in the fields of bioimaging and biosensing applications. In addition, the development of nanotechnology has enabled precise control over the nanostructure, size distribution, optical properties, and surface modifications of UCNPs, making UCNPs promising bioprobes for a wide range of biological applications [54].

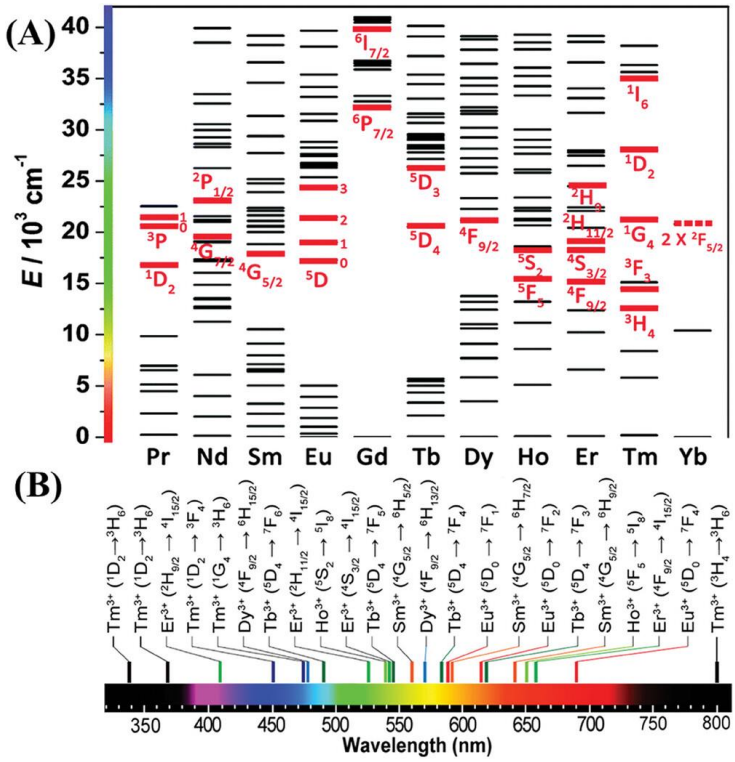

Figure 1-4 (a) Energy levels of Ln^{3+}. The highlighted energy levels are at which UCL occurs. (b) The Ln^{3+} generates significant upconversion luminescence and their corresponding energy level transitions in the UV–Vis region [55].

1.3.3 FRET Biosensors Based on Upconversion Nanoparticles

UCNPs are regarded as very sensitive bioprobes in the field of FRET biosensors owing to their distinct upconverting and photostability properties [56-58]. A prototypical UCNP-FRET biosensor is shown in Figure 1-5 [54]. UCNP-FRET has the potential to combine the benefits of UCNPs in biosensing with enhanced sensitivity and ease of tests. The lanthanoids exhibit emission bands that are narrow and may be adjusted, making them compatible with a wide range of FRET acceptors [59].

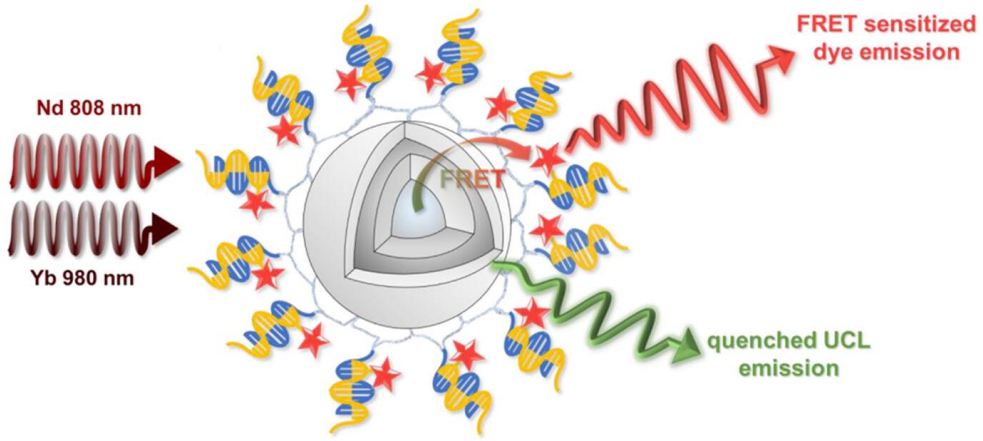

Figure 1-5 Prototypical UCNP–dye FRET DNA assay [54].

A FRET system based on novel UCNPs and graphene oxide (GO) was constructed for detecting H5N1 Influenza A virus (IAV) hemagglutinin (HA) (Figure 1-6) [60]. Small (sub-20 nm) sandwich-structured UCNPs with a high energy transfer efficiency were synthesized and functionalized amino-modified H5N1 HA aptamers. The π–π stacking interaction between the aptamer and GO shortens the distance between the UCNPs and the GO receptor, thereby realizing FRET. When HA is present, the aptamer preferentially bonds to HA, and UCNPs move away from the GO surface, resulting in a recovery of the fluorescence of UCNPs. Fluorescence signals showed a linear relationship between the concentration of HA within the range of 0.1–15 ng mL^{-1} and a LOD of 60.9 pg mL^{-1}. The biosensor also demonstrated its suitability for use in human serum samples with a linear range of 0–12 ng mL^{-1} and a LOD of 114.7 pg mL^{-1}. This strategy suggested the promising prospect of the FRET biosensor based on UCNPs in clinical applications because of the excellent sensing performance and sensitivity.

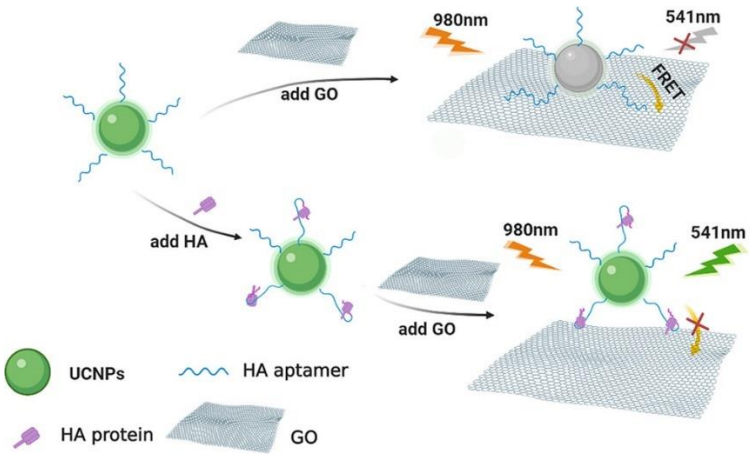

Figure 1-6 Schematic illustration to detect HA of influenza based on the FRET method [60].

A novel detection platform based on FRET for ultrasensitive and specific bacteria detection was developed using AuNPs as acceptor, while UCNPs functionalized with corresponding complementary DNA (cDNA) as donor [61]. The spectrum overlaps between the fluorescence emission of UCNPs and the absorption of AuNPs allows the occur of FRET when the targeted aptamer and cDNA hybridize, resulting in the decreasing of upconversion fluorescence. With the presence of target bacteria, the aptamers selectively attach to the bacteria, creating a three-dimensional structure. The combination causes the separation of UCNPs-cDNA and AuNPs-aptamers, leading to the recovery of upconversion fluorescence. The FRET aptasensor employing UCNPs effectively identified *Escherichia coli* ATCC 8739 (used as a representative analyte) within a detection range of 5–106 CFU/mL and a detection limit of 3 CFU/mL. The FRET aptasensor was further used to identify *E. coli* in actual tap/pond water, milk samples in a time frame of 20 min. Therefore, the UCNPs based FRET aptasensor has

the capability to detect a wide variety of targets, including entire cells and metal ions, by using various aptamer sequences. This technology shows significant promise in the fields of environmental monitoring, medical diagnostics, and food safety studies.

Liu et. al presented FRET biosensing platform based on peptide-functionalized UCNP@SiO_2@Cy5-pep for the detection of caspase-9 activity in vitro and in vivo [62]. A peptide tagged with Cy5 and possessing the particular motif LEHD for caspase-9 cleavage was intentionally developed and chemically attached to UCNP@SiO2 by covalent bonding. The red upconversion emission of UCNP@SiO_2 can be suppressed by Cy5 and the green upconversion emission of UCNP@SiO_2 remains unaffected. Following the cleavage of LEHD by caspase-9, the Cy5 dissociated from the surface of UCNP@SiO_2, leading to the recovery of red upconversion emission of UCNP@SiO_2. The UCNP@SiO_2@Cy5-pep was also used to track the changes of caspase-9 activity levels in apoptotic cancerous cells (MG-63 and SW480) induced by cisplatin. Under identical experimental conditions, the intracellular caspase-9 activity level in MG-63 cells treated with cisplatin is higher than that of cisplatin-treated SW480, which is consistent with the results of commercial caspase-9 activity kits. The UCL signal intensity ratio of red emission to green emission of UCNP (R/G) shows a linear relationship with the number of MG-63 cells in the range of 5×10^3 to 1×10^6 cells (0.5–100 U mL^{-1} caspase-9). The LOD is 675 cells (0.068 U mL^{-1} caspase-9). In addition, the feasibility of using UCNP@SiO_2@Cy5-pep for detecting caspase-9 activity in tumor tissues in living organisms is established, and favorable outcomes are achieved.

1.4 Sonodynamic Therapy for Antibacterial Applications

The rapidly growing spread and uncontrollable adaptation of bacteria that are resistant to antibiotics have already emerged as a pressing worldwide concern in the treatment of bacterial illnesses. The drug-resistant bacteria could develop enzymes that prevent antibiotics from entering their cells, alter their membrane barrier and permeability, or create drug efflux pumps to protect themselves from the antibacterial agents during the evolution of the bacteria [63]. Therefore, developing potent antibacterial methods and antibiofilm therapies that do not induce drug tolerance is a significant objective in the scientific community.

In recent times, there have been advancements in the development of antibiotic-free and non-invasive antibacterial techniques, including photodynamic therapy (PDT) [64, 65], photothermal therapy (PTT) [66, 67], as well as ultrasound-triggered sonodynamic therapy (SDT), or the synergistic therapy [63, 68]. Among these approaches, SDT has the greatest potential for the treatment of bacterial infection because of its excellent tissue-penetrating properties and effectiveness against drug-resistant bacteria.

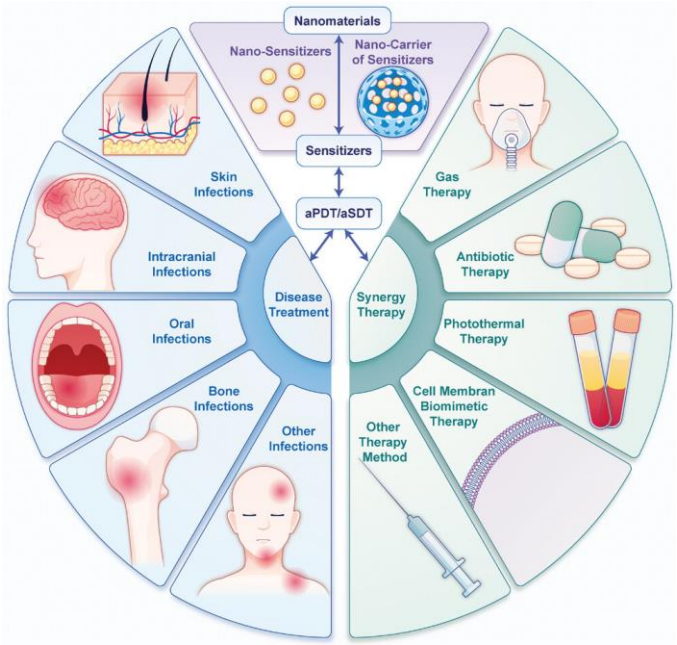

Figure 1-7 Nanomaterials in antibacterial photodynamic therapy and antibacterial sonodynamic therapy [69].

Sonodynamic therapy (SDT) is a non-invasive and effective therapeutic approach that utilizes ultrasound (US) in combination with a sonosensitizer to deal with antibiotic-resistant bacteria and biofilms. Designing a sonosensitizer nanoplatform to achieve an efficient SDT effect has significant importance (Figure 1-7). The SDT-based nanoplatforms have the potential to become a very effective next-generation noninvasive therapeutic tool for fighting bacterial illness.

1.4.1 Mechanism of Sonodynamic Therapy

The mechanisms of SDT have been extensively debated in recent years, although the precise operational concept of this process remains uncertain due to its inherent complexity. The reactive oxygen species (ROS) dependent damage and

mechanical/thermal damage is the most frequently acknowledged mechanism (Figure 1-8) [63].

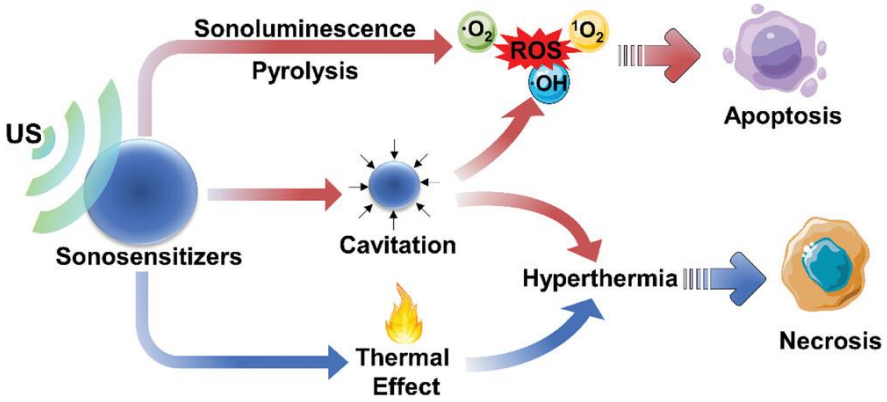

Figure 1-8 Schematic diagram of potential mechanisms of SDT [70].

ROS is a group of potent substances that includes singlet oxygen ($^1O_2$), hydroxyl radical (•OH), superoxide anion radical($\bullet O^{2-}$), hydrogen peroxide (H_2O_2), and other similar compounds. The primary cause of bacterial death and biofilm eradication based on SDT is the generation of ROS triggered by US.

During the SDT process, the sonosensitizer absorbs energy and transits from its ground state to a high-energy state. As it returns to its low-energy state, it releases a significant amount of energy, along with reactive oxygen species (ROS). The ROS produced can effectively promote lipid peroxidation in bacteria cells, damage intracellular DNA and protein, and induce apoptosis of target cells to realize SDT.

One significant way that SDT works is by producing cavitation effects using ultrasound [71]. Inertial and non-inertial cavitation, two components of the cavitation effect's intricate process, are intimately associated with gas oscillation. The quick deflation of gas bubbles exposed to the US causes them to release energy. The outcome

is elevated temperatures and pressures, which cause the death of certain cells. Intense microbubble fragmentation has other effects, such as facilitating the entry of extracellular sonosensitizers into bacterial cells, where they generate sonosensitive activity and hasten the demise of target cells. Thermal effects are another kind of SDT; they kill the target tissue by heating it up with ultrasound. Tissue undergoes mechanical energy absorption and subsequent thermal energy release during US absorption and transformation. The lesions are heated to a higher temperature using low-energy ultrasound, which causes permanent thermal damage to the target tissue [72].

1.4.2 Sonosensitizers for Sonodynamic Therapy

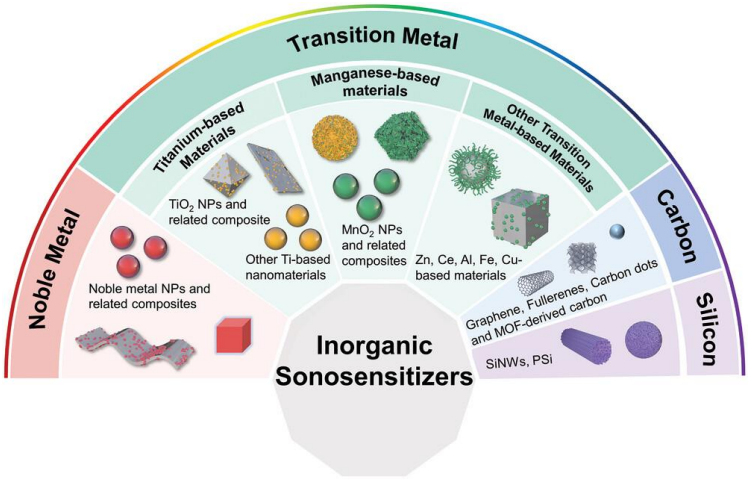

Figure 1-9 Classification diagram of inorganic nanomaterials applied to SDT [73].

According to the mechanism of SDT, sonosensitizer plays a crucial role in determining the effectiveness of SDT since the quantity of ROS generated by sonosensitizers under the irradiation of ultrasound has a direct impact on the effectiveness of SDT. Currently, sonosensitizers are primarily classified into two

categories: organic and inorganic sonosensitizers. Organic sonosensitizer often consist of porphyrin derivatives, anthocyanins, chlorophyll derivatives, and other organic molecules [74, 75]. In addition. extensive studies have been conducted in recent years on a wide range of inorganic nanostructures that are more stable and have specific physiochemical properties, such as titanium dioxide (TiO_2) [76-78], zinc oxide (ZnO_2) [78, 79], $BaTiO_3$ [80-82], C-based, and Si-based materials (Figure 1-9).

1.4.3 Sonodynamic Therapy for Antibacterial Applications

An ultrasmall platinum-copper alloy nanoparticles (PtCu NPs) as sonosensitizer was developed for enhanced sonodynamic bacterial elimination and tissue repair [83]. The PtCu NPs with high sonodynamic activity performance are synthesized and modified with poly (maleic anhydridealt-1-octadecene)-polyethylene glycol (C_{18}PMH-PEG). The PtCu- NPs can efficiently kill both gram-positive and gram-negative bacteria under the irradiation of US. Additionally, the PtCu NPs develop favorable Fenton-like catalytic performance and exceptional glutathione-depleting capacity due to the partial oxygenation on their surface, resulting in an increased production of ROS. Additionally, the PtCu- NPs also remove *S. aureus* infection by producing ROS and then promote wound healing in the *S. aureus*-infected wound model (Figure 1-10).

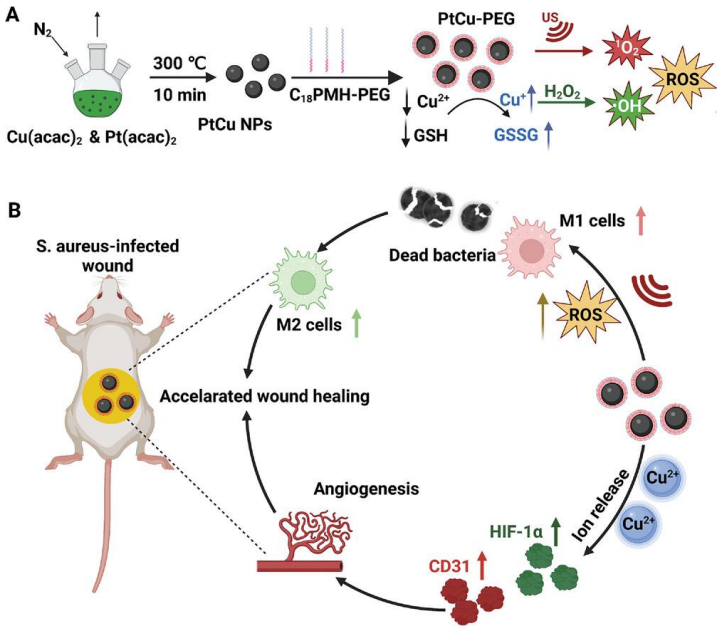

Figure 1-10 Scheme illustrating the PtCu-PEG NPs for sonodynamic bacteria elimination and tissue repair [83].

Conferring catalytic defects in sonosensitizers is of paramount importance in reinforcing sonodynamic therapy. Mao et. al designed a 2D catalytic planar defects with abundant Ti^{3+} species (Ti_3C_2-SD(Ti^{3+})) within Ti_3C_2 sheets (Figure 1-11) [84]. These specific planar slip dislocations can produce surface-bound O by effectively activating O_2, leading to a substantial amount of $^1O_2$ generation. The bactericidal elimination efficiency achieved 99.72% ± 0.03% when subjected to US stimulation. By applying neutrophil membrane (NM) proteins to the surface of Ti_3C_2-SD(Ti^{3+}) sheets, there is a significant decrease of 6-$\log_{10}$ in the amount of methicillin-resistant *Staphylococcus aureus* in the infected bony tissue.

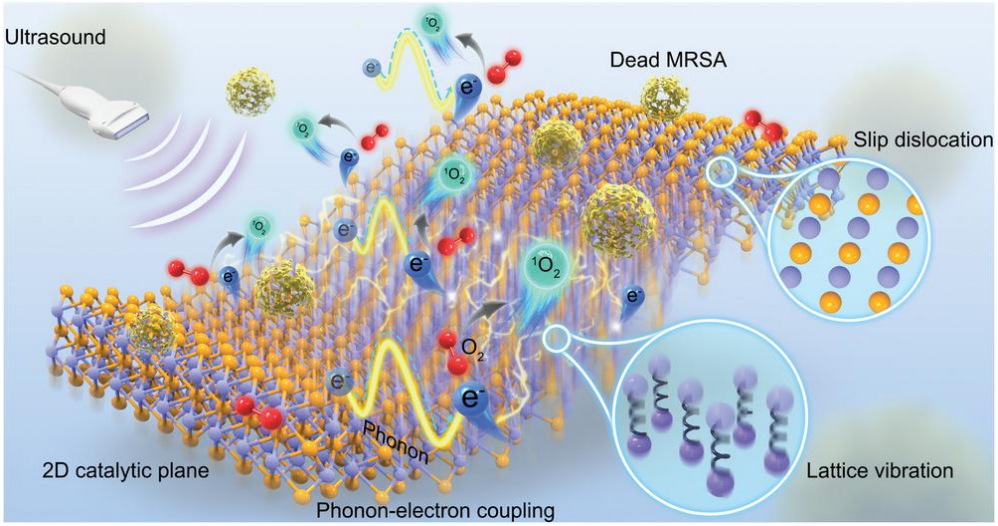

Figure 1-11 Mechanism and antibacterial performance of 2D catalytic planar defects-mediated SDT [84].

1.5 Motivation and Structure of Work

1.5.1 Research Motivation

Public healthcare systems face a significant problem when harmful organisms, such as viruses and bacteria, experience outbreaks. Infectious diseases caused by viruses or bacteria have been the most threatening to global health, and early diagnosis and therapy are crucial to cut off the spreading of the infected disease. The early detection of infectious pathogens and the subsequent therapy are essential for preventing propagation. For the biodetection assay, FRET has been commonly used for biosensing as the luminescent intensity of fluorophore varies with the approach or separation of the energy pairs. In addition, UCNPs are biocompatible and photostable luminescence materials that are suitable for bioprobes. Therefore, developing FRET

biodetection assay based on UCNPs for the detection of viruses will be studied in this thesis. As for the therapy of the pathogens, SDT has tremendous potential in preventing multidrug-resistant bacterial infections, considering it is non-invasive and requires no antibiotic dependence, which can effectively solve the problem of bacterial resistance. However, efficient sonosensitizers for the generation of ROS under the trigger of US are still changes for the current sonodynamic antibacterial research. Hence, designing an effective sonosensitizer for sonodynamic antibacterial application is conducted in this work.

1.5.2 Structure of Work

The main objective of the present work is

a) To construct an ultrasensitive FRET biosensor based on csUCNPs and AuNPs for the detection of SARS-CoV-2 RNA.
b) To construct sonosensitizers with excellent ROS generation performance for sonodynamic antibacterial applications

The chapters of the thesis are organized as follows:

Chapter 1: Introduction. This chapter introduces the categorization of infectious pathogens, biosensors for virus detection, biosensors based on upconversion nanoparticles, and sonodynamic therapy for antibacterial applications. In addition, the current challenges for the diagnosis and treatment of infectious pathogens and the motivation for this work are also presented.

Chapter 2: Methodology. This chapter introduces the coprecipitation method for

the synthesis of UCNPs and hydrothermal synthesis of BWO NSs. The characterization instruments and techniques include X-ray scattering techniques, UV-Vis absorption, photoluminescence spectroscopy, transmission electron microscopy (TEM) and scanning electron microscopy (SEM), X-ray photoelectron spectroscopy (XPS), zeta potential measurement and confocal laser scanning microscopy (CLSM).

Chapter 3: Ultrasensitive FRET Biosensor based on Upconversion Nanoparticles. This chapter reports on an ultrasensitive FRET biosensor based on UCNPs for the detection of SARS-Cov-2 virus RNA. The sensitivity of this biosensor is greatly improved to as low as 750 aM by incorporating the core-shell structure of UCNPs and using the LSPR effect to increase the efficiency of FRET.

Chapter 4: *In vitro* Sonodynamic Antibacterial Applications Based on Yb-doped Bi_2WO_6 Nanosheets. This chapter describes a Yb doped Bi_2WO_6 NSs sonosensitizer with enhanced ROS generation performance for sonodynamic antibacterial. The Yb-doped Bi_2WO_6 NSs demonstrated broad-spectrum antibacterial activity *in vitro* within 5 minutes of exposure to the US trigger.

Chapter 5: *In vivo* Sonodynamic Antibacterial Therapy Based on Bi_2WO_6 Nanosheets Modified Hydrogel. This chapter discusses that Yb-doped Bi2WO6 NSs sonosensitizer combined with hydrogel has low cytotoxicity and is applied to the *in vivo* sonodynamic antibacterial therapy. Yb-doped Bi2WO6 NSs sonosensitizer combined with hydrogel significantly accelerated the wound healing process in bacteria-infected models.

Chapter 6: Conclusion and outlook. This chapter provides a summary and recommendations for future research based on the previous work discussed in Chapters 3-5.

Chapter 2 Methodology

2.1 Synthesis Methods of Nanomaterials

2.1.1 Coprecipitation Method

Coprecipitation is a synthesis procedure where multiple chemicals are simultaneously precipitated in a solvent (Figure 2-1). Coprecipitation often occurs when a solution becomes supersaturated, leading to the formation, enlargement, and clustering of particles by nucleation. The nucleation process is the crucial step in coprecipitation, as it marks the initiation of particle creation. Subsequently, secondary processes such as Ostwald ripening and aggregation come into play. These secondary processes play a crucial role in shaping the size, shape, and characteristics of particles. The particle size distribution, shape, and sizes of particles are influenced by reaction circumstances, such as the rate at which reactants are added and the intensity of stirring. The coprecipitation method is a straightforward and efficient technique for synthesizing UCNPs due to its favourable reaction conditions, cost-effectiveness in terms of equipment, uncomplicated procedures, and quick reaction times. Therefore, the coprecipitation method is employed in this work for synthesizing UCNPs and core-shell UCNPs.

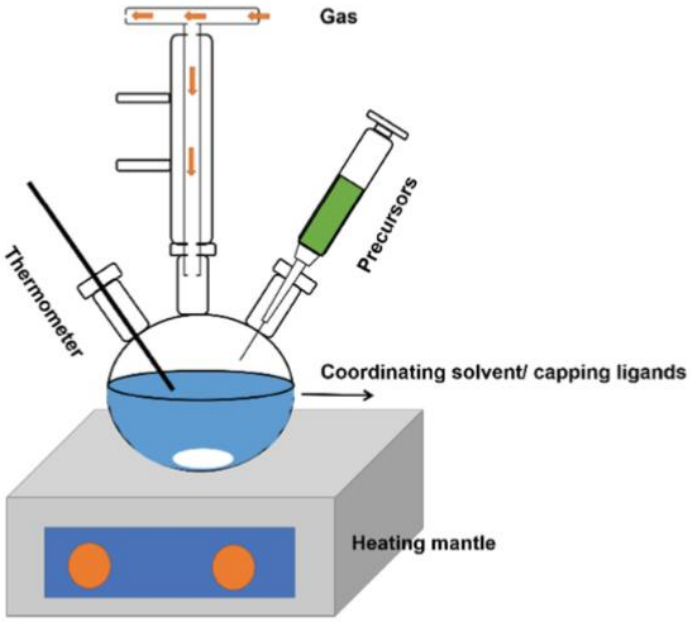

Figure 2-1 A schematic illustration of co-preparation synthesizing of UCNP [85].

2.1.2 Hydrothermal Method

Hydrothermal synthesis involves subjecting aqueous precursors in a vessel to a high-pressure and high-temperature autoclave reactor. The size distribution, shape, and crystallinity of the products can easily be managed by adjusting factors like the type of surfactant, temperature, reaction time, pressure, or type of solvent. The Bi_2WO_6 nanosheets with different doping concentrations of Yb were synthesized using the hydrothermal method in this work.

2.2 Characterization Techniques

2.2.1 X-ray Diffraction

X-ray diffraction (XRD) is a technique used to examine the scattering of X-rays by crystalline substances. Diffraction and absorption by molecular or crystalline

microstructures are both possible with X-rays due to their wavelength being very close to that of most molecules or unit cells. Every crystalline substance has a unique set of X-ray fingerprints, which are determined by the intensity of X-rays scattered at different angles. A XRD pattern is produced when X-rays from a beam irradiated on a sample surface at a certain angle and interact with the crystalline planes at various angles of incidence. Bragg's law is used to compute the angle at which X-rays undergo diffraction when interacting with a crystal, so enabling the determination of the atomic positions inside the crystal lattice. The reflection of X-rays only occurs on a certain crystal plane, when the Angle θ of the incident X-ray, the crystal plane spacing d, and the wavelength λ of the incoming ray conform to the following formula:

$$2d \sin\theta = n\lambda$$

It is possible to distinguish between different crystalline materials by analyzing the X-ray diffraction (XRD) pattern. This research employed XRD analysis equipment using CuK radiation (wavelength = 0.154 nm) from the SmartLab system from Rigaku Co., Japan, to evaluate the crystalline structures of the UCNP, AuNP, and BWO NSs.

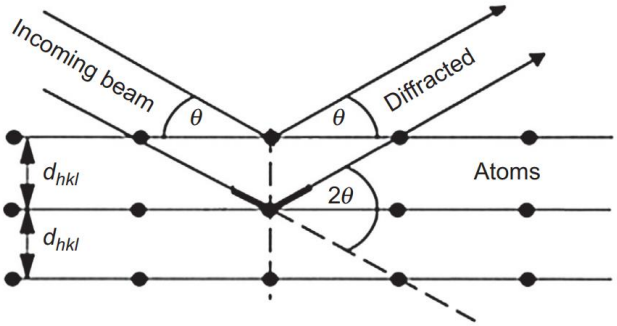

Figure 2-2 Geometrical condition for diffraction from lattice planes [86].

2.2.2 UV-vis Absorption

The absorption characteristics of the materials in this research were assessed using a PerkinElmer UV-Vis-NIR spectroscopy (Figure 2-3(a)), which is able to analyze wide range absorption nm of the samples. The UV-Vis absorption spectrum quantifies the reduction in light intensity after it traverses a substance. The detector captures the transmitted light, which is then analyzed for absorption throughout the scanned range of wavelengths. The three detector modules cover a wide wavelength range of 175~3300 nm, including a photomultiplier tube (PMT) detector for the UV-Vis range (175~860.8 nm) and an indium gallium arsenide (InGaAs) detector (860.9~1800 nm) and a lead sulfide (PbS) detector (1800~330 nm) for the NIR range. The optical system of the UV-Vis-NIR spectroscopy detector modules is depicted in Figure 2-3(b).

The absorption characteristic is crucial in constructing biosensing platform, including the synthesis of AuNPs and the fabrication of the biosensing probes. AuNPs with varied particle sizes exhibit varying absorption peaks due to plasmonic features. Hence, the absorbance serves as an indicator of the size of the AuNPs. Furthermore, as the fluorescence quenchers in the FRET biosensor, the absorption of AuNPs is crucial in an LRET-based biosensing system. As for the construction of the biosensing probes, the absorbance of the oligos at ~260 nm was measured to verify the conjugation oligo on the surface of UCNPs and the AuNPs.

Figure 2-3 (a) The photograph of PerkinElmer UV-vis-NIR spectrometer. (b) Schematic of the optical system of the detector module.

2.2.3 Photoluminescent Spectroscopy

The photoluminescent (PL) spectroscopy of the synthesized UCNPs were obtained by a PL measurement system FLS920, Edinburgh Instruments (Figure 2-4).The instrument has four channels, two of which are connected to external lasers and the Xenon lamp, while the other two are connected to external lasers and the Xenon lamp individually. The left arm of this device is not used in this experiment, but the right arm is connected to the photomultiplier tube, which amplifies the emission signal before it reaches the optical detector. As an excitation source, we used a Xenon lamp and a 980 nm diode laser (MDL-III, CNI Optoelectronics Tech. Co., China). The 980 nm diode laser has two modes: pulse mode for lifespan measurements and continuous wave for photoluminescence measurements, and the modulator's mode can be simply changed by the modulator. The emission intensities of FAM-MXene and UCNPs-MXene hybrids are evaluated in aqueous solution since drying the functionalized samples destroys the surface groups and causes hybrids to collapse, which has a significant impact on emission intensities. Therefore, different modified UCNPCs can be dispersed

either in water or in cyclohexane for PL measurement.

In this study, polystyrene disposable cuvettes and quartz cuvettes were employed. When measuring UCNPs in cyclohexane, however, it is worth mentioning that quartz cuvettes are preferable to polystyrene disposable cuvettes since cyclohexane causes polystyrene to swell. There should be no residual UCNPs on the cuvette to ensure the accuracy of the data, hence the polystyrene disposable cuvette is more appropriate for measuring the emission intensity throughout the biodetection.

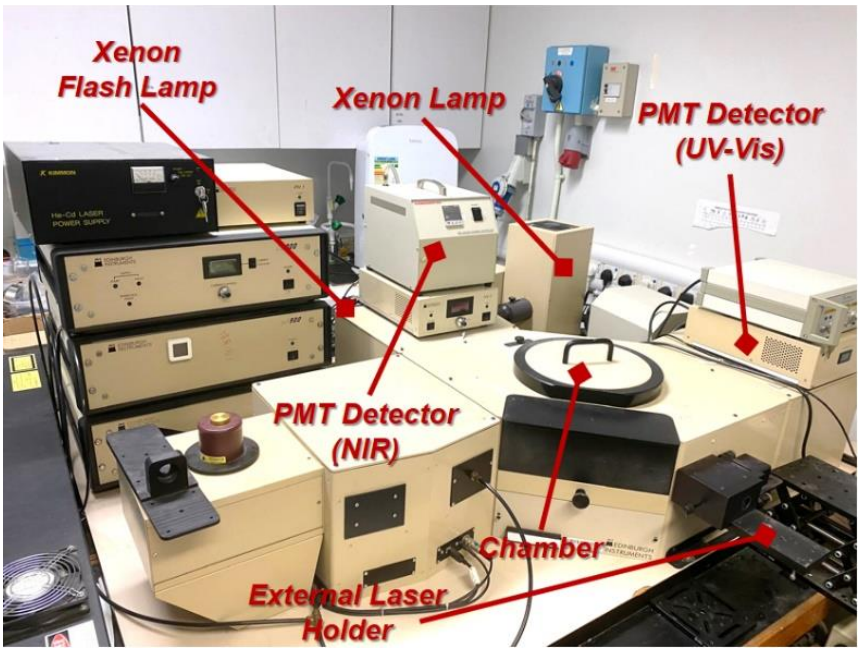

Figure 2-4 The photograph of FLS920 PL spectroscopy (Edinburgh Instruments).

2.2.4 Transmission electron microscopy and scanning electron microscopy

The transmission electron microscopy (TEM) is an essential technology for examining the size, structure and compositions of nanoscale materials. The morphology of the UCNPs, AuNPs and BWO NSs was captured using a field emission transmission

electron microscopy, JEOL JEM-2100F, Japan (Figure 2-5). with a 200 Kev field emission gun. The collision of a high-voltage electron beam with nanoparticles and a carbon grid results in the generation of secondary signals including X-rays, diffracted electrons, and transmitted electrons. In particular, morphologies of the nanoparticles revealed by the signal of transmitted electrons, and the crystalline structures of the nanoparticles could be confirmed by analyzing the electron diffraction patterns formed by diffracted electrons interacted with the samples.

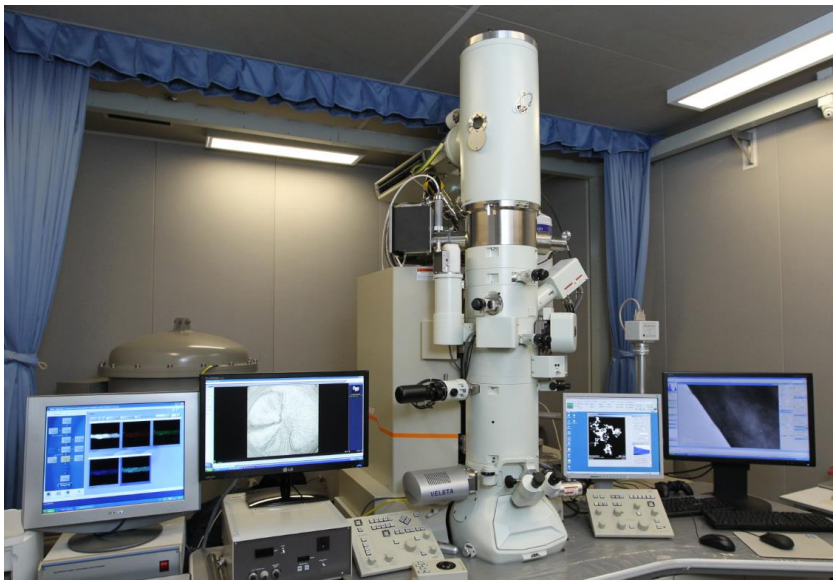

Figure 2-5 The photograph of field emission transmission electron microscopy (JEOL JEM-2100F)

The scanning electron microscope (SEM) is an additional instrument to investigate and analyze characterizations of microscopic shapes and elements. The morphology characterizations and elemental distributions of the materials in this research were studied using a field emission SEM, Tescan CLARA, coupled with an energy-

dispersive X-ray spectroscopy (EDX) system. EDX can be accomplished in the SEM to provide an EDX can be accomplished in the SEM which can give a rough result to estimate the element compositions.

2.2.5 X-ray Photoelectron Spectroscopy

X-ray photoelectron spectroscopy (XPS) is a technique used to analyze the chemical composition of the surface of a material. XPS is capable of identifying the elemental composition, chemical formula, electronic configuration, and chemical state of a given substance. XPS spectra are generated by irradiating a surface with an X-ray beam and simultaneously capturing the kinetic energy and electrons emitted from the near surface of the materials. The emitted electron carries a distinct amount of kinetic energy that is correlated to both the photo energy and the binding energy of the electron. By performing calculations on the emitted electrons over a range of kinetic energies, a photoelectron spectrum may be generated. This spectrum displays peaks corresponding to the released electrons with certain energy levels. In this work, XPS was employed to identify the surface terminals and the composition of the Yb doped Bi_2WO_6 nanosheet using a Thermo ScientificTM NexsaTM X-Ray photoelectron spectrometer system, connected to monochromatic and microfocus Al K X-ray source (1486.2 eV).

2.2.6 Zeta Potential Measurement

The surface charge of nanomaterials is also an important indicator during the surface modification process. A method for determining the surface charge during the functionalization of UCNPs and AuNPs is zeta potential measurement. Zeta potential

(ξ) is a quantitative measure of the electric charge on the surface of a particle in a certain solvent. The surface charges of the surface modification of UCNPs play a crucial role in determining the effectiveness of the modification. In this work, the surface zeta potential of UCNPs and AuNPs after each step of modification or conjugation was obtained using a Malvern Dynamic Light Scattering (DLS) Zetasizer with a Malvern Panalytical Folded Capillary Zeta Cell DTS1070.

2.2.7 Confocal Laser Scanning Microscopy

A contemporary confocal microscope generally comprises an epifluorescence microscope equipped with multiple laser sources and a confocal scan head. The scan head includes fluorescent filter sets, a galvanometer-based raster scanning mechanism, multiple or adjustable pinhole apertures, and photomultiplier tube (PMT) detectors for different wavelength ranges. The laser beam is enlarged to completely cover the rear opening of the objective lens. The objective lens then concentrates this enlarged beam into a concentrated spot on the object plane. This spot is moved in a pattern that covers the whole object, thus the phrase "point scanning confocal." The focused spot on the object emits fluoresced light, which passes through the pinhole aperture. However, the out of focus light, which is more scattered, does not pass through the aperture and is therefore excluded from the image. This is because the pinhole is located just before the image plane of the objective, where the PMT is positioned. The PMT produces a voltage corresponding to image intensity at that spot on the image at a specific time. The voltage varies as the laser beam is scanned in both space and time. An analog-to-

digital converter is used to convert the analog voltages acquired from the PMT into a digital signal. This conversion occurs at certain intervals that correspond to the intensities of the picture display (pixels) viewed on a computer monitor. The live/dead staining of bacteria in this article was observed using a Nikon AXE Laser Confocal Microscope (Figure 2-6).

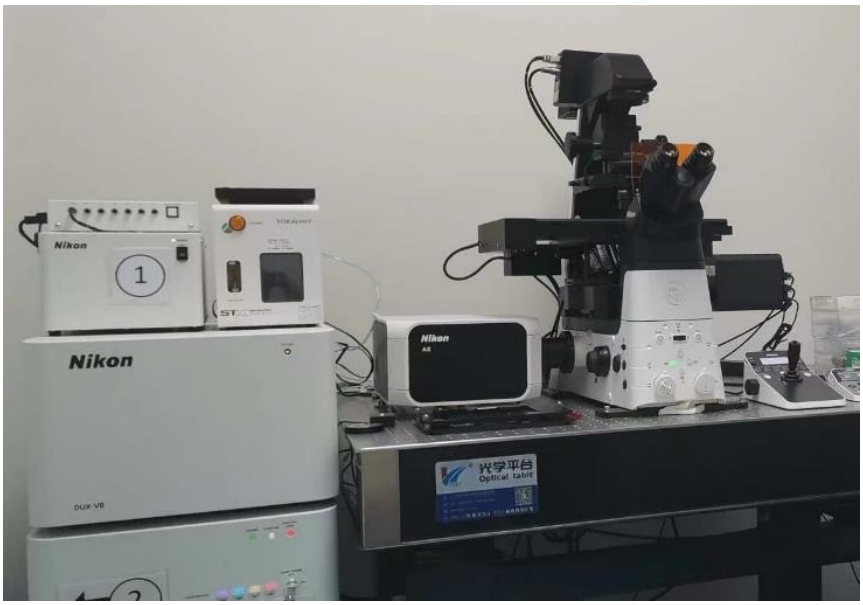

Figure 2-6 Nikon AXE Laser Confocal Microscope.

Chapter 3 Ultrasensitive FRET Biosensor Based on Upconversion Nanoparticles

3.1 Introduction

Fluorescence resonance energy transfer (FRET) is a nonradiative energy transfer process between energy donor and energy acceptor pairs that are located within a distance of 2-10 nm[87-89]. FRET has been commonly used in biosensing due to its ability to detect changes in the luminescent intensity of fluorophore in response to the proximity or separation of the energy donor and energy acceptor pairs[90-92]. Lanthanide-doped upconversion nanoparticles (UCNPs) are capable of converting low-energy near-infrared (NIR) light into high-energy ultraviolet (UV) or visible light. They also process distinctive upconversion luminescence properties, including significant anti-Stokes shift, narrow emission band, high photostability, and long luminescence lifetime[93, 94]. Moreover, UCNPs that are triggered by low-energy NIR irradiation result in a minimum impact on biomarkers and living organisms, making UCNPs very attractive for bioanalytical and biomedical applications[51, 95, 96]. Accordingly, UCNPs have been extensively utilized as the energy donor in FRET biosensors to detect biological samples[97-99]. The Au-based nanomaterials, such as Au nanospheres and Au nanorods, display size/shape-regulated optical, electrical, and catalytic properties, high extinction coefficient, and aggregation-dependent color change[100]. The precise control

over the size range and optical properties of gold-based nanoparticles has made them widely applicable and extremely suitable as acceptors in FRET biosensors.[101, 102].

Improving the efficiency of FRET is a viable strategy for enhancing the sensitivity of FRET sensors. FRET efficiency is greatly affected by spectrum overlap between the emission of donor and the absorption of acceptor, as well as the distance between donor and acceptor. Significant endeavors have been undertaken to enhance the limit of detection (LOD) of FRET biosensors by the optimization of the UCNP architecture, employing suitable energy acceptors, and refinement of the biosensor design.[54, 98]. Surface plasmon resonance (SPR) refers to the collective oscillations of the conducting electrons in metallic structures at resonant conditions. Localized surface plasmon resonance (LSPR) is a specific type of SPR that is localized to a metallic nanostructure with dimensions smaller than the wavelength of incident light [103, 104]. LSPR has the ability to concentrate the incident electromagnetic (EM) field around the metallic nanostructure and impact the optical process, resulting in plasmon enhanced fluorescence (PEF), surface enhanced Raman scattering (SERS), as well as plasmon enhanced FRET (PE-FRET). PE-FRET provides the potential to increase the efficiency of FRET and thereby improve the sensitivity of biosensing. Hou et al. reported a novel self-assembled plasmonic substrate that can enhance FRET efficiency, enabling ultrasensitive detection of DNA hybridization and imaging in living cells with

improved temporal and spatial resolution[105]. Nevertheless, little research has been undertaken on PE-FRET biosensors using UCNPs for the purpose of virus detection.

Here, an ultrasensitive PE-FRET biosensor for the detection of SARS-CoV-2 viral Ribose Nucleic Acid (RNA) is constructed. The biosensor utilizes the core-shell UCNPs (csUCNPs) $NaGdF_4$:Yb/Tm@$NaYF_4$:Yb/Er as energy donor and the gold nanoparticles (AuNP) as energy acceptor. The design of the core-shell structure of UCNPs, together with the incorporation of AuNPs as the energy acceptor, offers multiple attributes that are necessary for enhancing the sensitivity of the biosensor. Er^{3+} was introduced into the shell of UCNP to provide an optimal distance between the energy donor and energy acceptor for FRET process. The purpose of coupling the inner core UCNP $NaGdF_4$:Yb/Tm with AuNP was to facilitate plasmon modulated FRET and improve the efficiency of energy transfer between energy pairs[105, 106]. With the increase of target oligonucleotide concentration, the quenching efficiency of the biosensor based on Tm^{3+}/Er^{3+} co-doped csUCNP exceeded 90%, which was much higher compared to that of FRET biosensors without plasmon enhancement. Consequently, the LOD of the biosensor was enhanced to 750 aM. Moreover, a clinical sample containing SARS-CoV-2 viral RNA was also analyzed to further confirm the sensitivity of the biosensor.

3.2 Experimental

3.2.1 Materials

Lanthanide acetates including $Y(Ac)_3 \cdot 4H_2O$, $Gd(Ac)_3 \cdot 4H_2O$, $Yb(Ac)_3 \cdot 4H_2O$, $Tm(Ac)_3 \cdot 4H_2O$, $Er(Ac)_3 \cdot 4H_2O$, NH_4F, 1-octacene (ODE), oleic acid (OA), cyclohexane, hydrochloric acid (HCl, 37 %) and Poly(acrylic acid) (PAA, Mw=1800) were purchased from Sigma Aldrich. 1-Ethyl-3-(3-dimethylaminopropyl)-carbodiimide hydrochloride (EDC), N-hydroxysulfosuccinimide sodium salt (sulfo-NHS) and tetrachloroauric acid ($HAuCl_4$) were obtained from TCI. Sodium citrate, potassium carbonate (K_2CO3), tannic acid, NaOH, dithiothreitol (DTT), 2-(N-morpholino)ethanesulfonic acid (MES) were purchased from Aladdin. DNA oligos were purchased from the University of Hong Kong, Faculty of Medicine, LKS Center for PanorOmic Sciences. None of the aforementioned compounds underwent further purification before usage. DEPC water was used for all the procedures involving oligonucleotides (oligos).

3.2.2 Synthesis of the Nanoparticles

3.2.2.1 Synthesis of UCNP

Synthesis of the core $NaGdF_4$:Yb/Tm nanocrystals: The core UCNP $NaGdF_4$:Yb/Tm were synthesized by the coprecipitation method according to a previously reported article[107]. Lanthanide^{3+} (Ln^{3+}) acetates, including yttrium (Y), gadolinium (Gd), ytterbium (Yb), terbium (Tm), and erbium (Er) were dissolved in de-ionized (DI) water to form 0.2 M aqueous solution for further usage. In a typical

synthesis procedure, 1 ml of 0.2 M $Gd(CH_3COO)_3$, 0.98 ml of 0.2 M $Yb(CH_3COO)_3$, 0.02 ml of 0.2 M $Tm(CH_3COO)_3$, 4 ml of OA and 6 ml of ODE were added into a 50-ml flask. Under magnetic stirring (1500rpm), the solution was slowly heated from room temperature to 150 °C and maintained for 40 minutes. Then the reaction mixture was allowed to cool to room temperature after removing the heating mantle. At room temperature, a mixture of 1 ml of 1 M NaOH-methanol solution and 3.3 ml of 0.4 M NH_4F-methanol solution was quickly injected into the reaction flask after 10 seconds of vortex. The mixture was then heated to 50 °C and maintained for 30 minutes with vigorous stirring to evaporate methanol. After that, the mixture was heated to 100 °C, followed by a 10-minute vacuum degassing to evaporate the residual moisture and methanol. The flask was then heated to 290 °C at a rate of 10 °C/min under the protection of argon gas and maintained for 1.5 hours before cooling to room temperature. The synthesized UCNPs were precipitated by adding 5ml of ethanol and collected by centrifugation. The UCNPs were further purified with cyclohexane and ethanol three times and dispersed in cyclohexane for the synthesis of core-shell UCNPs.

Synthesis of the core-shell $NaGdF_4$:Yb/Tm@$NaYF_4$:Yb/Er UCNPs: The core-shell $NaGdF_4$:Yb/Tm@$NaYF_4$:Yb/Er UCNPs were synthesized approximately the same as the procedure of core UCNPs. Briefly, 1.6 ml of 0.2 M $Y(CH_3COO)_3$, 0.36 ml of 0.2 M $Yb(CH_3COO)_3$, 0.04 ml of 0.2 M $Er(CH_3COO)_3$, 4 ml of OA and 6 ml of ODE were added into a 50-ml flask. Under magnetic stirring (1500 rpm), the solution was slowly heated from room temperature to 150 °C and maintained for 40 minutes. Then the reaction mixture was allowed to cool to room temperature after removing the heating mantle. At

room temperature, the as-prepared core UCNPs $NaGdF_4$:Yb/Tm were injected into the flask. Then, a mixture of 1 ml of 1 M NaOH-methanol solution and 3.3 ml of 0.4 M NH_4F-methanol solution was quickly injected into the reaction flask after 10 seconds of vortex. The mixture was heated to 50 °C and maintained for 30 minutes with vigorous stirring and then heated to 100 °C followed by a 10-minute vacuum degassing. The flask was then heated to 290 °C at a rate of 10 °C/min under the protection of argon gas and maintained for 1.5 hours before cooling down to room temperature. The synthesized csUCNPs were precipitated by adding 5ml of ethanol and collected by centrifugation. The csUCNPs were further purified with cyclohexane and ethanol three times for surface modification.

3.2.2.2 Synthesis of AuNPs

The citrate-stabilized AuNPs were synthesized according to the previous report [108]. Briefly, tannic acid (20 μL, 2.5 mM), potassium carbonate (200 μL, 150 mM) and sodium citrate solution (30 mL, 2.2 mM) were added to a 50 ml flask under vigorous stirring. The mixture was heated to 70 °C and 100 μL $HAuCl_4$ (25 mM) was added two times every 10 minutes interval. The solution then turns pink and naturally cools to room temperature for continued use.

3.2.3 Surface Modification of csUCNP

The as-synthesized csUCNP was precipitated in 15 mL ethanol with the addition of 112 μL HCl (2 M). After sonication for 30 min, the csUCNPs were precipitated by centrifugation and redispersed in 15 mL ethanol. After that, 11.2 μL HCl (2 M) was

added and sonicated for 30 min. Then the ligand-free csUCNP were collected using high-speed centrifugation. After that, PAA (20 mg) dissolved in NaOH (0.2 M) was added to the ligand-free csUCNPs. The colloidal solution was stirred overnight and PAA-csUCNPs were collected by high-speed centrifugation, followed by 3 successive purifications with water. The PAA-csUCNPs were dispersed in water (1 mL) for storage.

3.2.4 Conjugation of csUCNP with Amino-Modified Oligos

PAA-csUCNPs (200 μL) were buffer-exchanged in MES buffer (pH 5, 500 μL). After that, EDC (3 mg) and NHS (6 mg) were added to the csUCNPs under stirring for 30 min. Then, 1 nmol of P2 was added to the tube and stirred for another 2.5 h to ensure a complete coupling reaction. The csUCNPs-P2 were collected by high-speed centrifugation and washed with water three times. The csUCNPs-P2 were then dispersed in water for further use.

3.2.5 Conjugation of AuNPs with Sulfhydryl-Modified Oligos

DTT solution (10 μL, 0.1 M) was added to P1 (10 nmol) for S-S bond cleavage reaction for 1 h. The cleaved P1 was purified and recovered by illustra microspin G-25 column (GE Healthcare). Then, the AuNPs were modified with a previously reported instantaneous oligo modification [109]. The DTT-treated P1 (10 μL) was added to citrate-stabilized AuNPs (200 μL) with PB buffer (4 μL, 50 mM) and citrate buffer (pH 3, 10 μL). The mixture was incubated for 5 min and the AuNPs-P1 was recovered by high-speed centrifugation. The washing step was repeated three times. The AuNPs-P1 was dispersed in water (200 μL) for further use.

3.3 Characterization of the Nanoparticles

The core-shell UCNP was synthesized using the coprecipitation method, and TEM was utilized to characterize the morphology of the as-synthesized UCNP. The core UCNPs $NaGdF_4$:Yb/Tm exhibit a uniform hexagonal structure (Figure 3-1(a)) with an average dimension of 15.7 nm (Figure 3-1(c)). The corresponding high-resolution transmission electron microscope (HRTEM) image in Figure 3-1(b) demonstrates that the UCNP is highly crystalline, with a lattice space of 0.29 nm, corresponding to the (101) lattice plane of $NaGdF_4$:Yb/Tm. The subsequently synthesized csUCNPs $NaGdF_4$:Yb/Tm@$NaYF_4$:Yb/Er also exhibit a hexagonal structure (Figure 3-1(d)). The high-angle annular dark-field imaging (HAADF) in Figure 3-1(f) clearly illustrates the core-shell structure of the csUCNPs. The thickness of the shell is calculated to be ~6.5 nm based on the size distribution results in Figure 3-1(c) and (f).

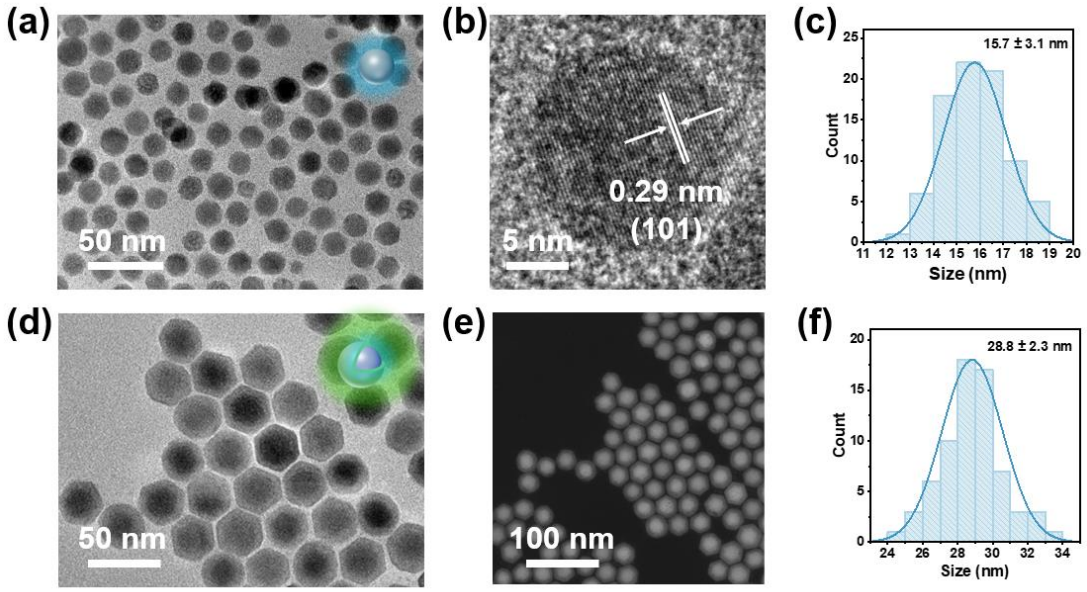

Figure 3-1 (a) TEM image; (b) HRTEM image; (c) corresponding size distribution of core UCNP $NaGdF_4$:Yb/Tm. (d) TEM image; (b) HAADF image; (c) corresponding size distribution of core-shell UCNP $NaGdF_4$:Yb/Tm@$NaYF_4$:Yb/Er.

Citrate-stabilized AuNPs with precisely regulated size were prepared and served as the energy acceptor probe in the PE-FRET detection system. As depicted in Figure 3-2(a), the TEM image indicated that the uniform sphere AuNPs with an average size of 5 nm were successfully synthesized. The HRTEM of AuNP in Figure 3-2(b) revealed a lattice space of 0.23 nm, corresponding to the (111) lattice plane of AuNP. The resultant AuNPs processed a broad absorption in the visible region, with the absorption peak centered at 518 nm (Figure 3-2(c)).

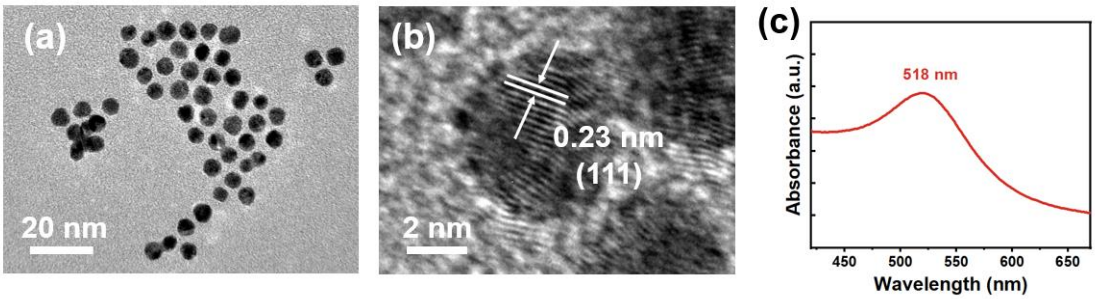

Figure 3-2 (a) TEM image; (b) HRTEM image; (c) UV-vis absorption spectrum of AuNPs.

Under the trigger of near-infrared (NIR) 980 nm laser, the emission peaks of the synthesized Tm^{3+}/Er^{3+} co-doped csUCNP were located at 451 nm (Tm^{3+}, $^1D_2 \rightarrow {}^3F_4$), 542nm ($Er^{3+}$,$^2H_{11/2} \rightarrow {}^4I_{15/2}$) and 654 nm ($Er^{3+}$, $^4F_{9/2} \rightarrow {}^4I_{15/2}$), respectively (Figure 3-3, blue curve). The absorption of AuNPs (Figure 3-3, red curve) matched well with the

upconversion emission of Er^{3+}, assuring efficient energy transfer between csUCNP and AuNPs. Additionally, the upconversion emission of Tm^{3+} might operate as the incident light and trigger the LSPR of AuNPs. This would concentrate the electromagnetic (EM) field, which in turn increases the efficiency of FRET between the energy pairs.

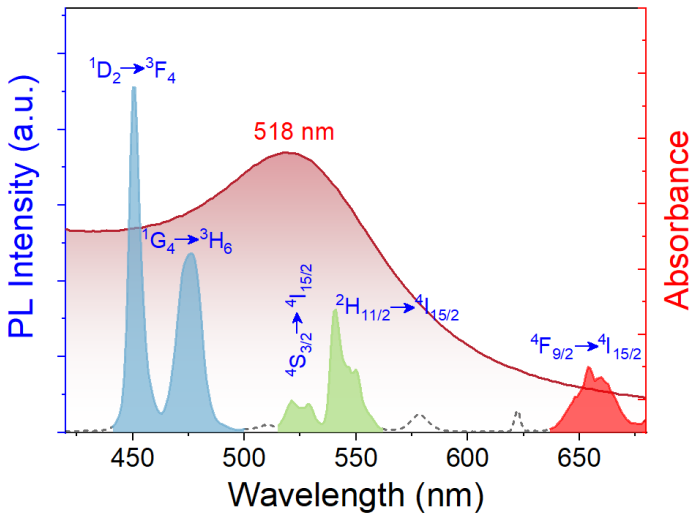

Figure 3-3 Upconversion emission spectrum of csUCNP (blue) and UV-vis absorption spectrum of AuNP (red).

3.4 Biodetection of SARS-CoV-2 RNA

3.4.1 Biomarker of SARS-CoV-2

The genome of SARS-CoV-2 RNA is single-stranded with positive sense. It contains around 30 kilobases in length and encodes around 9860 amino acids (Figure 3-4) [110], including spike glycoprotein gene (S gene), envelop protein gene (E genes) and nucleocapsid protein gene (N genes), and the non-structural RNA-dependent RNA polymerase (RdRp) and replicase open reading frame 1a/b (ORF1a/b) genes. It is the primary biomarker for diagnosing COVID-19. Designed primers targeting these genes

are demonstrated to be specific and sensitive for the novel SARS-CoV-2 and ruled out most of the other coronaviruses and influenza viruses (H1N1, H3N2, H5N1, etc.)

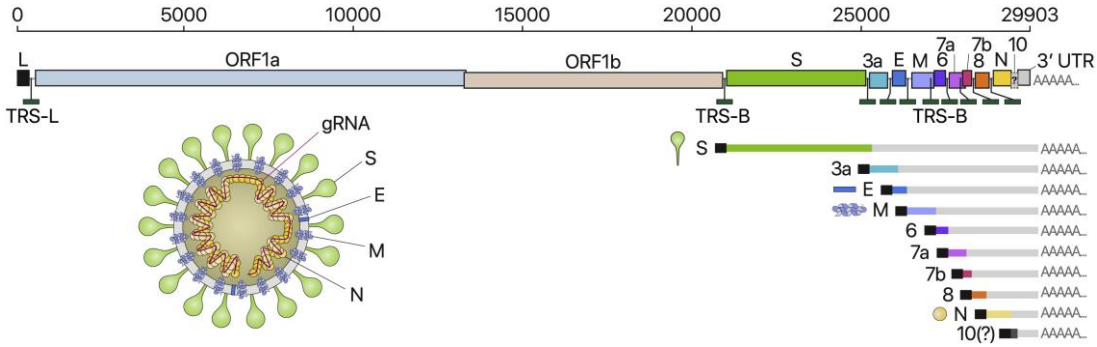

Figure 3-4 Schematic Presentation of the SARS-CoV-2 Genome Organization, the Canonical Subgenomic mRNAs, and the Virion Structure [110].

3.4.2 Detection Scheme

The detection scheme of this work is depicted in Figure 3-5. A FRET and LSPR dual-effected PE-FRET biosensing system was fabricated for the sensitive detection of SARS-CoV-2 RNA, with the csUCNP $NaGdF_4$:Yb/Tm@$NaYF_4$:Yb/Er and AuNP as the probes. The oligonucleotide-modified csUCNP and AuNP could be conjugated by target oligo to form csUCNP-AuNP composite, resulting in a shorter distance between csUCNP and AuNP. The Er^{3+} in the shell of the UCNP acted as the energy donor, and AuNP served as the energy acceptor, leading to the FRET process between csUCNP and AuNP. Hence, the upconversion emission could be quenched with the increase of the target sequence concentration. Furthermore, the energy transfer efficiency could be further enhanced through the coupling between the inner core of csUCNP and the LSPR of AuNP. As a result, the increased FRET efficiency significantly improved the LOD of

the biosensor, which is an essential performance metric for biosensors.

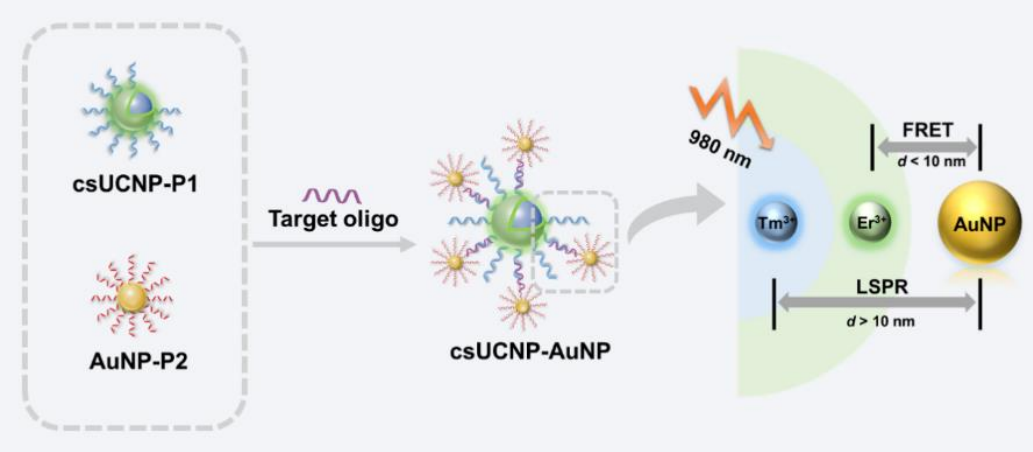

Figure 3-5 Schematic of the plasmon-enhanced FRET biodetection assay.

The N gene of SARS-CoV-2 was chosen as the target sequence for detection since the N gene sequence is conserved and less prone to mutation [111]. A 41-base oligonucleotide sequence was selected from the N gene sequence of SARS-CoV-2 based on a reported methodology [43]. Two oligonucleotides complementary to the target sequence are selected according to their banding energies, termed as P1 and P2, respectively. In order to modify the complementary oligonucleotides on the surface of csUCNP and AuNP, P1 is functionalized with amino groups at the 3' end while P2 is with the sulfhydryl group, collectively called P1-NH_2 and P2-SH. P1-NH_2 will be further attached with csUCNP, and P2-SH will connect with AuNP to fabricate the sandwich biodetection assay. The target and complementary sequences with detailed base order information are displayed in Table 3-1.

Table 3-1 The oligonucleotide sequences of the N gene target of *SARS-CoV-2* and the complementary probe sequences.

	Sequence (5'-3')
Target Sequence	5'-ACA CCA AAA GAT CAC ATT GGC ACC CGC AAT CCT GCT AAC AA-3'
P1-NH_2	5'-TTG TTA GCA GGA TTG CGG /3AmMC6T/-3'
P2-SH	5'-GTG ATC TTT TGG TGT /3ThioMC3-D/-3'

3.4.3 Surface Modification of csUCNPs and AuNPs

Before constructing the sandwich biodetection assay, the oleate-capped csUCNP (csUCNP-OA) will undergo several surface modification procedures, including acid treatment, surface carboxylation, and conjugating with *P1-NH_2*, as illustrated in Figure 3-6(a). As shown in Figure 3-6(b), the UV-vis absorption spectrum of the oligonucleotide-modified csUCNP exhibited an absorption peak at 260 nm, which is the characteristic absorption peak of the oligonucleotide, indicating that *P1-NH_2* has been successfully attached on the surface of csUCNP. In addition, zeta potential was utilized to verify the successful surface modification of csUCNP at each step, as displayed in Figure 3-6(c).

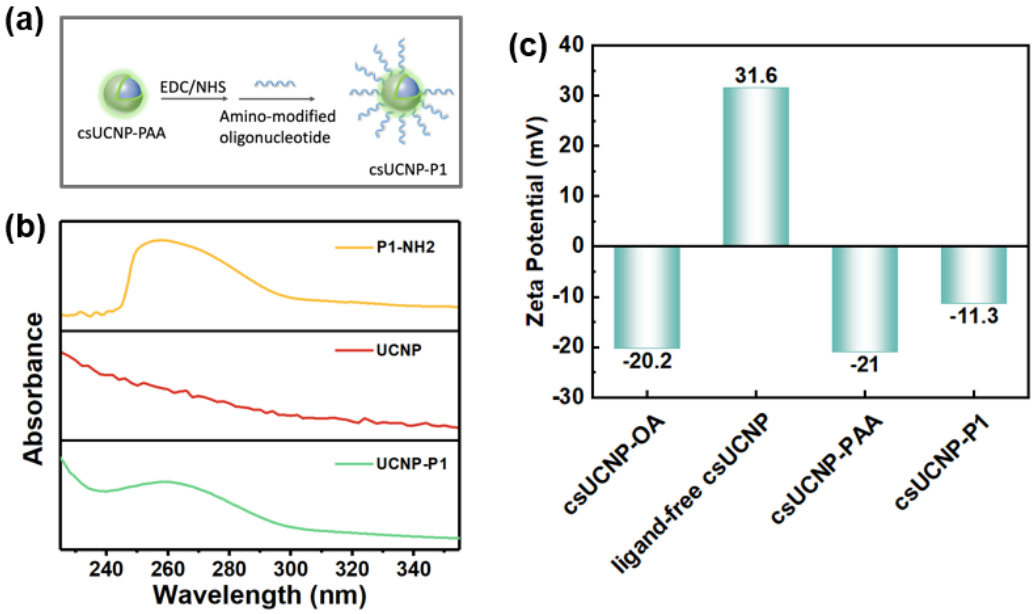

Figure 3-6 (a) Schematics of attaching amino-modified oligonucleotide to csUCNP-PAA; (b) UV-vis spectra of P1-NH_2, csUCNP, and csUCNP-P2; (c) Zeta potential for the relative nanoparticles during the modification procedure.

As for the construction of the AuNP probe, the oligonucleotide P2-SH was connected on the surface of AuNP by forming solid gold-sulfur bonds. The simplified bonding procedure can be completed within 30 min using a pH-assisted method [109], which involves the addition of a citrate-HCl buffer (pH = 3). The process diagram is depicted in Figure 3-7(a). Figure 3-7(b) shows the normalized UV-vis absorption spectra of AuNP before and after the P2-SH modification (termed as AuNP-P2). The presence of an oligonucleotide absorption peak at 260 nm in the absorption spectrum of AuNP-P2 indicates the successful attachment of oligo on the surface of AuNP. In addition, the absorption peak of AuNP at 518 nm is slightly red-shifted to 526 nm after

the connection. Correspondingly, the aggregation of AuNPs also causes a change in the color of the solution from pink to light purple (inset of Figure 3-7(c), left: AuNPs, right: AuNP-P2). The mismatch of the absorption spectra and the observed alteration in the color of the solution can be attributed to the slight aggregation of AuNPs. Since the intense aggregation of AuNPs will affect the detection result, the aggregation of AuNPs has been minimized by adjusting the AuNP-to-oligonucleotide ratio and the concentration of citrate buffer. Moreover, the zeta potential of AuNP changed from -33.1 mV to -36.5 mV after being connected with the oligonucleotide P2-SH, which can be attributed to the replacement of citrate ligands on the surface of AuNP by P2-SH, as displayed in Figure 3-7(c). The surface potentials of csUCNP-P1 and AuNP-P2 are both negative; thus, there was no electronic attraction among the probes.

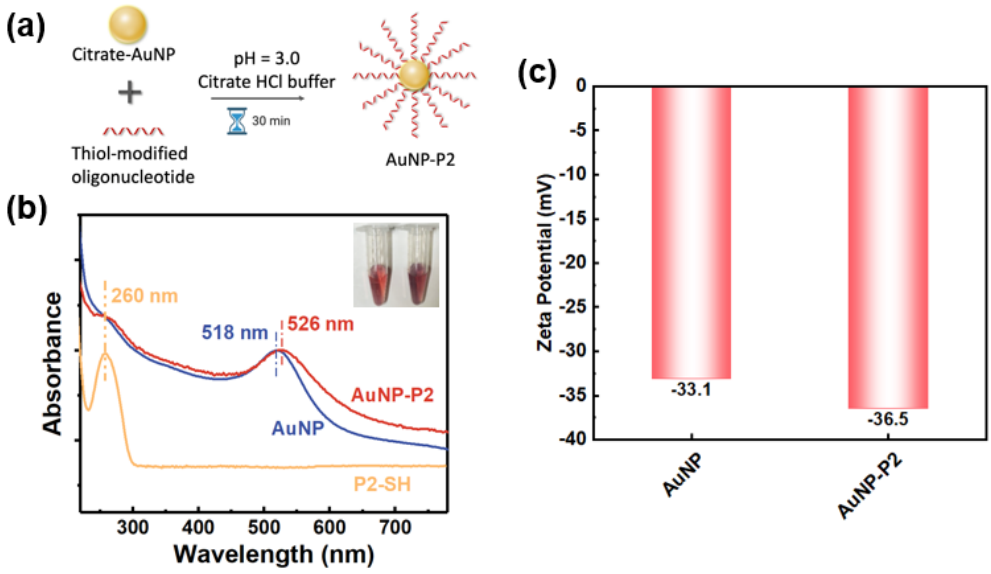

Figure 3-7 (a) Schematics of attaching thiol-modified oligonucleotide to AuNP (b) UV-vis spectra of P2-SH, AuNP and AuNP-P2 (inset are the photo of AuNP and AuNP-P2); (c) Zeta potential of AuNP and AuNP-P2.

3.4.4 SARS-CoV-2 RNA Detection

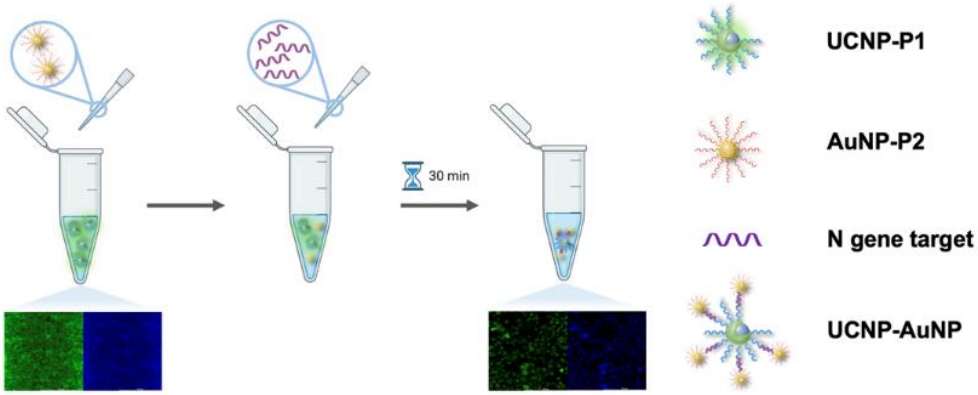

Figure 3-8 Schematic of the FRET biodetection procedure

Figure 3-8 shows the schematic of the biodetection procedure in this work. The csUCNP-P1 and AuNP-P2 probes were first added in a centrifuge tube and AuNP-P2 could partially suppress the upconversion emission of the UCNPs. With an increase in the amount of AuNPs, the emission of csUCNPs could be reduced to a greater extent. The quenching effect may be caused by the broad peak absorption of AuNPs, which can absorb a portion of the 980 nm excitation light, thus leading to the reduction of upconversion emission intensity. Therefore, the amount of csUCNPs and AuNPs was fixed while detecting the variation of N target sequence concentration. The insets of Figure 3-8 depicted the corresponding confocal microscopy images of csUCNP before and after the hybridization upon the 980 nm excitation (scale bar = 50 μm). The upconversion emission of Er^{3+} (green) and Tm^{3+} (blue) are apparently weaker after the hybridization with the N target sequences. It is worth noting that during the detection procedure, it is possible to disregard the variation in upconversion emission intensity

caused by the varying target concentration or solution volume (Figure 3-9). As P1 and P2 are complementary to the target N sequence, csUNCP-P1 and AuNP-P2 can be conjugated by the N target sequence. After the conjugation, the distance between csUNCPs and AuNPs became shorter, thus leading to an efficient FRET process and resulting in a significant quenching effect of upconversion emission.

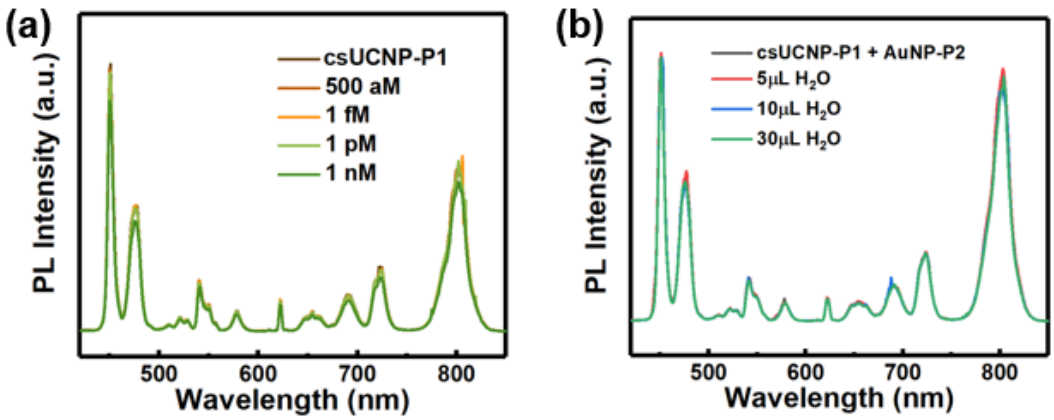

Figure 3-9 Change of upconversion emission intensity of csUCNP caused by (a) concentration or (b) volume.

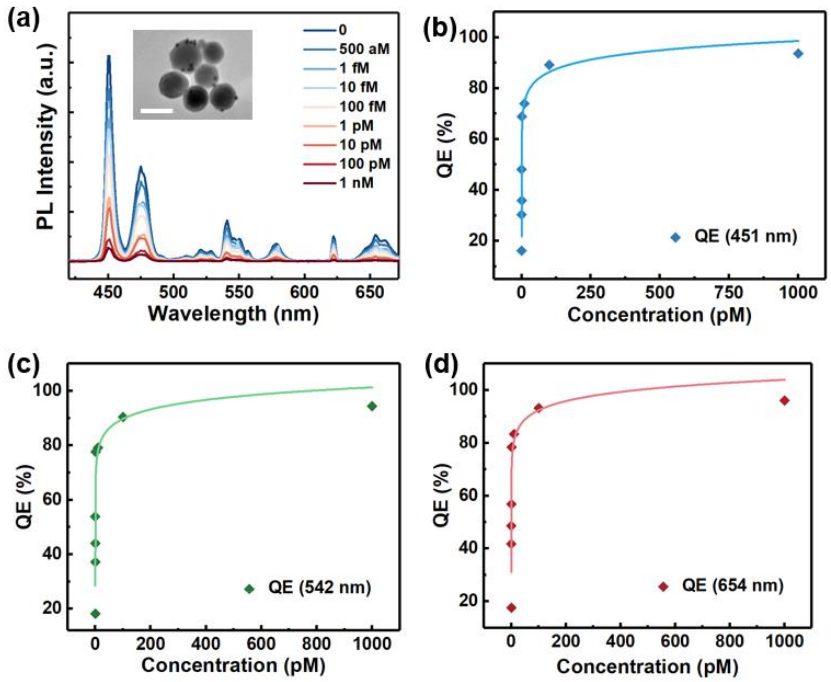

Figure 3-10 (a) Upconversion spectra of csUCNP probe with various concentrations of SARS-CoV-2 target sequence in the sandwich detection assay, the inset was the TEM image of the detection sample (scale bar = 50 nm); Quenching efficiency of three major upconversion emission peaks at (b) 451 nm, (c) 542 nm and (d) 654 nm with various concentration of SARS-CoV-2 target sequence.

The amount of AuNP attached to the surface of csUCNP increased with the increasing concentration of the N target sequence in the biodetection system, leading to an enhanced quenching effect with reference to the concentrations of the target sequence. As shown in Figure 3-10(a), the upconversion emission of csUCNP decreased significantly as the concentration of the N target sequence increased from 0 to 1 nM during the detection process. The inset of Figure 3-10(a) depicts the TEM image of the detection sample, in which csUCNP is surrounded by several AuNPs,

indicating the conjugation between AuNPs and csUCNP. Figure 3-10(b-d) shows the quenching efficiency of the upconversion emission peaks at 451 nm, 542 nm, and 654 nm, respectively. Apparently, the quenching efficiency significantly increased with the increase of the N target sequence. In addition, the quenching efficiency of csUCNP exceeds 90% with 1nM target oligo, which is much higher than that of the FRET biosensor based solely on Er^{3+} doped UCNP, as shown in Table 3-2.

Table 3-2 Comparison of common FRET biosensors based on UCNPs.

Type of UCNPs	**Accepter**	**Surface Functionalized**	**Target**	**LOD**	**Detection Range**
$NaYF_4$:Yb,Er [112]	Quantum dots	Streptavidin	biotin	5 nM	1 nM–1 μM
$NaYF_4$:Yb,Tm [113]	SYBR Green I	ssDNA1	ssDNA	3.2 nM	10 nM–200 nM
$NaYF_4$:Yb,Er [114]	AuNPs	Oligonucleotides	long-chain DNA sequence	3 nM	0-60 nM
$NaYF_4$:Yb,Er@$NaYF_4$ [115]	Cy3 dye	ssDNA	miR20a	30 pM	0.1–100 nM
$NaYF_4$:Yb,Er [116]	Gold Nanorods	ssDNA	DNA	7 pM	0-100 nM
$BaGdF_5$:Yb/Er [117]	AuNPs	Oligonucleotides	Ebola Virus RNA	300 fM	3–50 pM
$NaGdF_4$:Yb/Er@$NaGdF_4$ [118]	AuNPs	Oligonucleotides	SARS-CoV-2 RNA	11.46 fM	200 fM–10 nM
$NaGdF_4$:Yb/Tm@$NaYF_4$:Yb/Tm (**This work**)	AuNPs	Oligonucleotides	SARS-CoV-2 RNA	750 aM	1 fm–1 nM

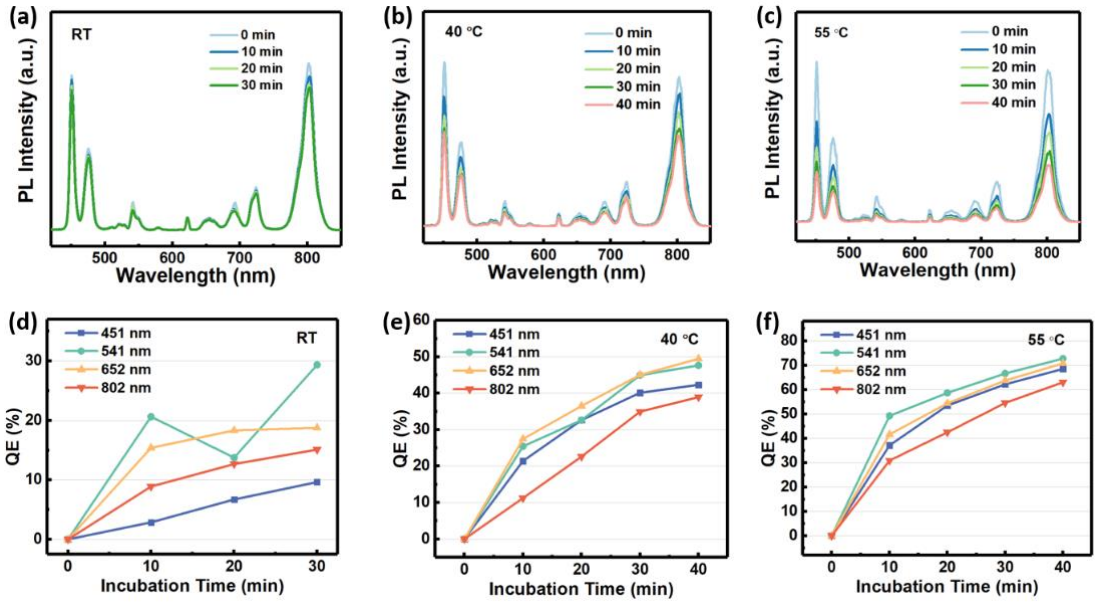

Figure 3-11 Upconversion emission spectra of csUCNP incubated at (a) room temperature; (b) 40 °C; (c) 55 °C. The target sequence concentration was 1pM; Corresponding quenching efficiency of different upconversion emission peaks.

To evaluate the optimal incubation condition, the biosensor based on Tm^{3+}/Er^{3+} co-doped csUCNP was evaluated at the N target sequence concentration of 1 pM with varying incubation temperatures. The incubation time varied from 10 to 40 minutes with a 10-minute interval, and three incubation temperatures at room temperature (20 °C), 40 °C and 55 °C were selected for comparison (Figure 3-11). As shown in Figure 3-11(f), the quenching efficiency of csUCNP reached a maximum of nearly 90% after 40 min incubation at 55 °C. For comparison, $NaYF_4$:Yb/Er probe and $NaGdF_4$:Yb/Tm probe were also constructed and applied for detection under the same incubation condition. In contrast, the quenching efficiency of $NaYF_4$:Yb/Er UCNP reached only 48% at the incubation temperature of 55 °C (Figure 3-12). Whereas the

upconversion emission intensity of $NaGdF_4$:Yb/Tm probe exhibits only a slight decrease (Figure 3-13). The enhanced quenching efficiency against the target sequence concentration leads to an enhanced sensitivity for biosensor. Consequently, such a comparative study indicated that the design of core-shell structure and the co-doping of Tm^{3+} and Er^{3+} can significantly improve the sensitivity of biosensor based on UCNP probes, hence a lower LOD can be further obtained.

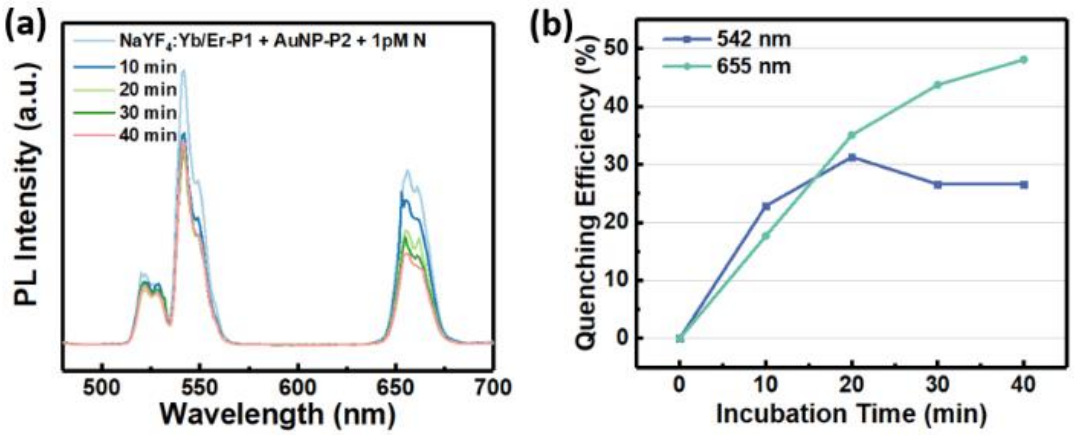

Figure 3-12 (a)Upconversion emission spectra of $NaYF_4$:Yb,Er-P1 incubated at 55 ℃. The target concentration is 1pM; (b) Corresponding quenching efficiency of different upconversion emission peaks.

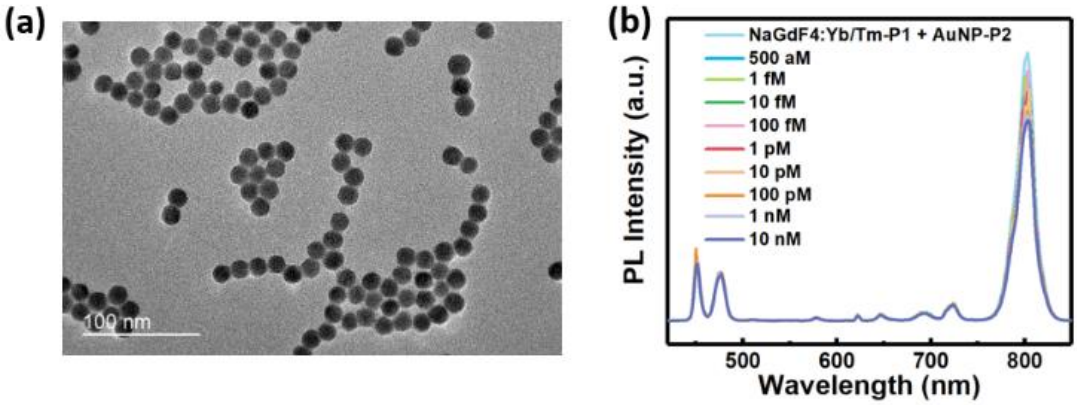

Figure 3-13 (a) TEM image of oligo functionalized UCNP $NaGdF_4$:Yb,Tm-P1; (b) Upconversion emission spectra of $NaGdF_4$:Yb/Tm probe with different concentrations of target sequence.

A possible cause of such high quenching efficiency is that the localized surface plasmons enhanced the energy transfer efficiency between energy pairs. The schematic of the mechanic in the PE-FRET biosensor based on oligo conjugated csUCNP-AuNP is displayed in Figure 3-14(a), and the energy migration processes of $Yb^{3+} \rightarrow Er^{3+}$ and $Yb^{3+} \rightarrow Tm^{3+}$ in the csUCNP under the excitation of 980 nm are exhibited in Figure 3-14(b). Specifically, Yb^{3+} is an ideal sensitizer for 980 nm excitation owing to the $^2F_{7/2} \rightarrow {}^2F_{5/2}$ transition, which well matches the electronic transitions of Er^{3+} and Tm^{3+}. The upconversion emission of Er^{3+} in the shell observed at 542 and 654 nm are ascribed to the $^2H_{11/2} \rightarrow {}^4I_{15/2}$ and $^4F_{9/2} \rightarrow {}^4I_{15/2}$ transitions. While the inner core upconversion emission of Tm^{3+} at 451 nm is attributed to $^1D_2 \rightarrow {}^3F_4$ transition. Furthermore, the core-shell structure enabled different doping concentrations for Yb^{3+}/Tm^{3+} and Yb^{3+}/Er^{3+}, respectively. Plenty of research have proved that metal nanostructures could induce

plasmon-enhanced upconversion emission, as the local electric field around metal nanostructures can promote the excitation rate of lanthanide sensitizer ions, leading to enhanced upconversion emission [119-122]. While there are additional studies demonstrating that surface plasmon could enhance FRET efficiency as well [123, 124]. Specifically, the energy transfer efficiency could be calculated by the following equation [125]:

$$E = 1 - \frac{F}{F_0} = \frac{{R_0}^6}{{R_0}^6 + r^6} \quad (1)$$

where F and F_0 are the upconversion emission intensities of UCNP before and after quenched by AuNP, r is the distance between the energy donor and the energy accepter, and R_0 is the Förster distance at which the 50% of energy is transferred. R_0 depends on a variety of factors, including the overlap of donor emission and acceptor absorption, donor quantum yield, and the orientation of transition dipole moments. Since LSPR will contribute to an increase in the Förster distance, the energy transfer efficiency would consequently increase [124, 126]. Therefore, the LSPR of AuNPs induced by Tm^{3+} upconversion emission improved the performance of the biosensor by enhancing the FRET efficiency, resulting in a higher detection sensitivity.

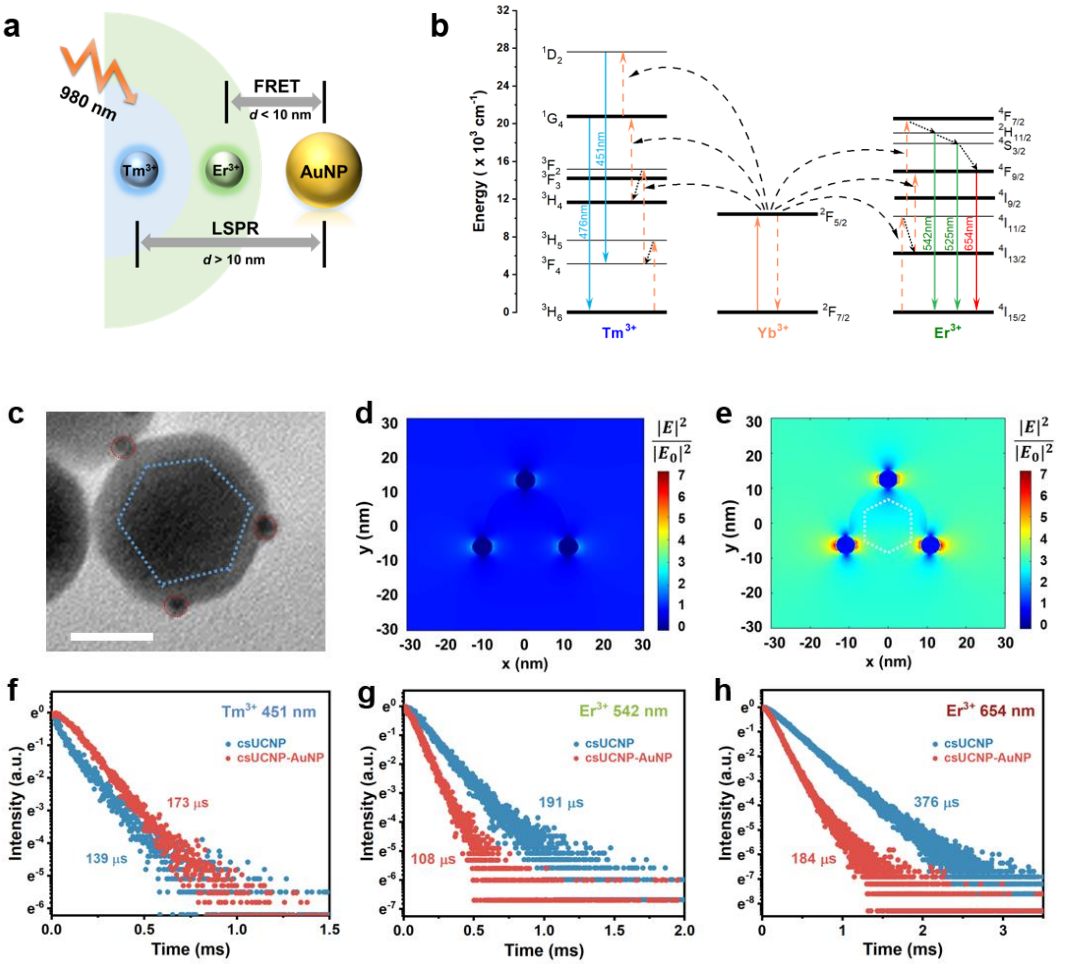

Figure 3-14 (a) Schematic of the mechanics in the PE-FRET biosensor based on csUCNP and AuNP; (b) Corresponding energy transfer routes of the csUCNP; (c) TEM image of oligo conjugated csUCNP-AuNP (scale bar = 20 nm); Simulated local electromagnetic field distribution of AuNPs by FDTD method (d) without the core emission; (e) with the core emission of Tm^{3+} at 451 nm. Luminescence decay curves of csUCNP and conjugated csUCNP-AuNP at (f) 451nm; (g) 542 nm; (h) 654 nm.

The electromagnetic field distribution of AuNPs under different situations were simulated by the Finite-Difference Time-Domain (FDTD) method and compared for

illustration. The simulation model was established according to TEM image of oligo conjugated csUCNP-AuNP composite in Figure 3-14(c). E/E_0 is utilized for demonstrating the variation of electromagnetic field intensity around gold nanoparticles with and without the core upconversion emission, where E is the value of local electromagnetic field and E_0 is the value of incident electric field. Figure 3-14(d) and (e) present the electromagnetic field intensities of AuNP around UCNP without and with the core upconversion emission of Tm^{3+}, respectively. The electromagnetic field intensities around AuNPs are obviously increased when Tm^{3+} upconversion emission in the core of csUCNP is present. According to previous research, the local electromagnetic field can influence the orientation of these dipoles, and thus influence the FRET efficiency [127]. Hence, the sensitivity of the presented PE-FRET biosensor was significantly enhanced by the design of core-shell structure and doping with Tm^{3+} in the inner core.

The decay times of the three main upconversion emission peaks (451 nm, 542 nm, 654 nm) were measured to further illustrate the energy transfer process between csUCNP and AuNP, as displayed in Figure 3-14(f-h). The decay curves could be well fitted by the following biexponential function (Equation (2)).

$$I(t) = A_1 \exp\left(-\frac{t}{\tau_1}\right) + A_2 \exp\left(-\frac{t}{\tau_2}\right) \quad (2)$$

$$\tau^* = \frac{A_1{\tau_1}^2 + A_2{\tau_2}^2}{A_1\tau_1 + A_2\tau_2} \quad (3)$$

where $I(t)$ is the photoluminescence intensity, A_1 and A_2 are corresponding

fitting constants, τ_1 and τ_2 are rapid and slow lifetimes of different exponential components. Then the average lifetime τ^* could be calculated by Equation (3). The average lifetimes of the upconversion emission peak of Er^{3+} at 542 nm and 654 nm decreased from 191 μs to 108 μs and from 376 μs to 184 μs, respectively. The significant decrease in lifetime of Er^{3+} indicates the high efficiency FRET process between the upconversion emission of Er^{3+} and AuNPs. However, the average lifetime of upconversion emission peak of Tm^{3+} at 451 nm exhibits negligible changes, indicating that FRET between the inner core of csUCNP and AuNP is either nonexistent or feeble. The slight decrease of lifetime of Tm^{3+} at 451 nm from 139 μs to 173 μs was probably caused by coupling with LSPR of AuNP.

3.4.5 Figure of Merit

The linear response, LOD, and specificity are three typical characteristics of biosensors. Therefore, to illustrate the excellent performance of co-doped csUCNP biosensor, the three typical characteristics of the biosensor based on Tm^{3+}/Er^{3+} co-doped csUCNP were discussed in this section.

As shown in Figure 3-10, the quenching efficiency of upconversion emission of csUCNP increased with the increase of N target sequence concentration. Therefore, a linear response could be found between the quenching efficiency and the concentration of target sequence. The linear fitting curve was displayed in Figure 3-15(a), with the linear equation of y= 10.3x + 37, indicating that the csUCNP was suitable to serve as the probe for constructing the FRET biosensor. The LOD of the biosensor could be

estimated by the following equation:

$$LOD = \frac{3\delta}{b} \quad (4)$$

where δ is the standard deviation and b is the slope of the linear fitting curve. Thereby, the LOD of csUCNP biosensor was calculated to be 750 aM, which was equivalent to 4.65 x 10^7 N target copies in 500 μL detection system volume. Compared to the reported biosensors based on Er-UCNPs, the doping of Tm^{3+} ions and the design of core-shell probes result in lower LODs of biological probes based on UCNPs.

The ability of the biosensor to recognize a particular target sequence is defined as specificity, and it is an essential component to consider when assessing the performance of the biodetection system. To examine the specificity of the biosensor based on csUCNP, a concentration of 1 pM of the N target sequence was selected for evaluation within the detection linear range. Two non-target gene sequences from the SARS and BAT viruses were subjected to comparative testing at the same concentration. According to the results of the specificity test in Figure 3-15(b), the non-target gene sequence has a significantly lower quenching efficiency than the SARS-CoV-2 virus oligo. This indicates that the constructed bioprobes based on csUCNP has high level of specificity for SARS-CoV-2 virus.

Based on the above demonstration, csUCNP-based biosensors in this work exhibit low LOD as well as high sensitivity and specificity for the detection of SARS-CoV-2. The design of core-shell structure of UCNP significantly enhanced the performance for the application of biodetection.

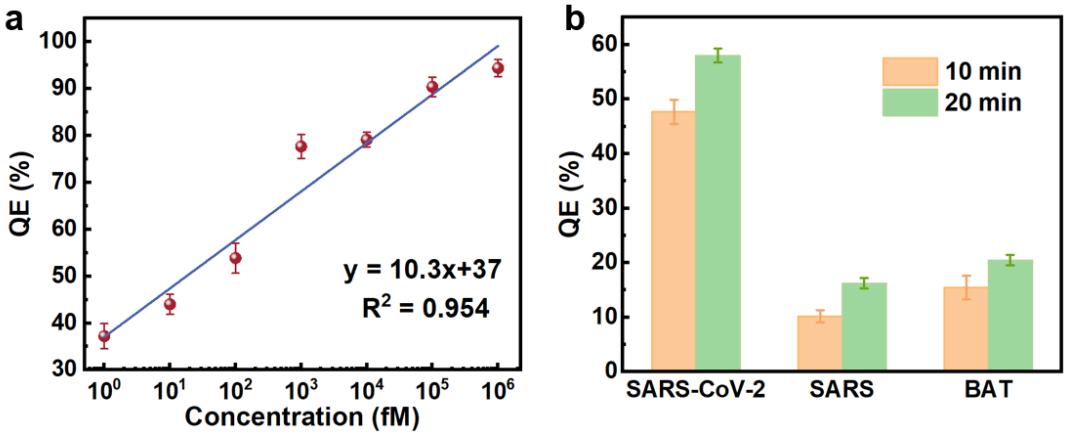

Figure 3-15 (a) Linear relationship of the sandwich assay based on csUCNP against different concentration of target sequence from 1 fM to 1 nM; (b) Specificity of the sandwich assay with the non-target oligonucleotide sequence concentration of 1 pM.

3.4.6 Detection of PCR-Validated Deactivated Clinical Sample

To further verify the feasibility of the csUCNP-based biosensor in clinical application, the performance of the biosensor on clinical sample detection was further tested. The RNA from inactivated SARS-CoV-2 virus sample used for clinical detection was obtained from the University of Hong Kong, Faculty of Medicine. Prior to the detection by csUCNP-based biosensor, RT-PCR was utilized to determine the concentration of the inactivated SARS-CoV-2 virus sample. A series of standard samples with different concentrations were running in the same RT-PCR procedure to generate the standard curve. The Ct value of the clinical sample was 23 (Figure 3-16(a)) and the concentration was determined to be 180 fM according to the standard curve. The clinical sample was diluted tenfold for detection by csUCNP-based biosensor. Figure 3-16(b) is the time varying luminescence spectrum of the csUCNP at the SARS-

CoV-2 RNA concentration of 18 fM. After incubation for 10 minutes, the fluorescence intensity decreased significantly and the relative quenching efficiency of the four upconversion emission peaks with respect to time was displayed in Figure 3-16(b). The quenching efficiency of the upconversion emission peaks reached up to 30% at such a low target sequence concentration. The results demonstrate that the csUCNP-based biosensor constructed for the detection of SARS-CoV-2 clinical samples performs admirably.

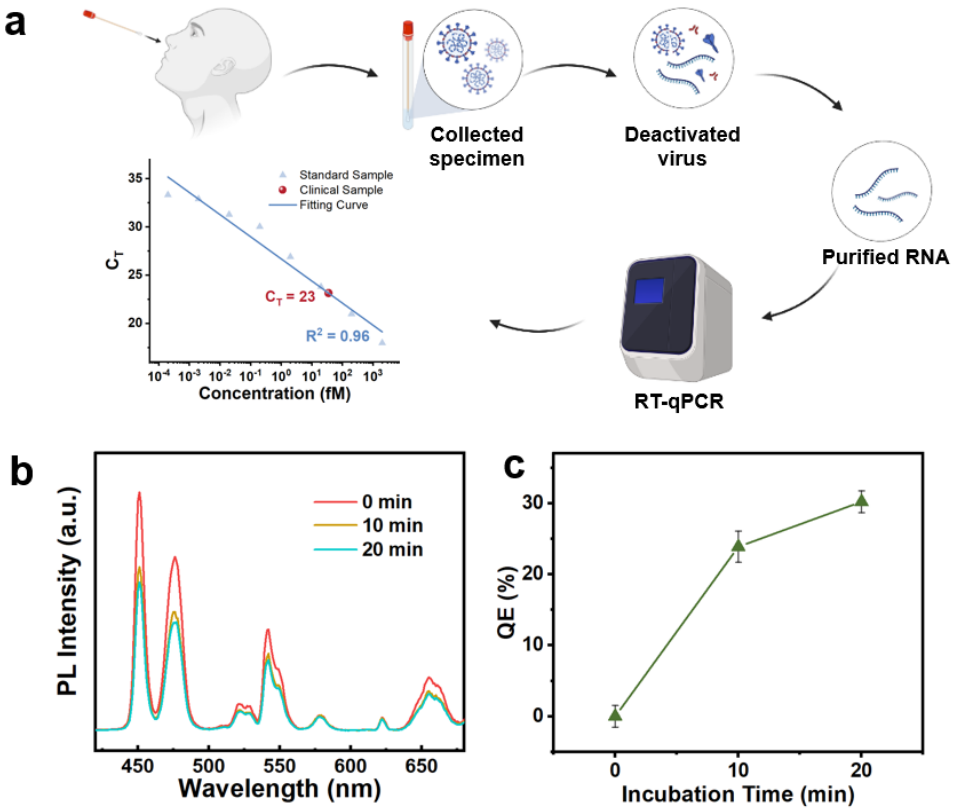

Figure 3-16 (a) Diagnostic testing through RT-PCR and the test results; (b) Upconversion emission spectra and (c) quenching efficiency of the detection of deactivated clinical SRAS-CoV-2 sample based on csUCNP FRET biodetection assay.

3.5 Conclusion

In summary, a plasmon-enhanced FRET biosensor based on UCNP with core-shell structure was proposed for ultrasensitive detection of SARS-CoV-2 viral RNA. After conjugation with the target sequence, the distance between csUCNPs and AuNPs was reduced, which activated the FRET process and effectively quenched upconversion emission. Simultaneously, the upconversion emission of Tm^{3+} in the inner core of csUCNP induced LSPR of AuNPs, leading to a significant increase of FRET efficiency. Consequently, the dual effect of LSPR and FRET results in higher sensitivity of biosensor based on csUCNP. The LOD of the PE-FRET biosensor was improved to 750 aM with decent linear response and good selectivity, which is much lower than that of biosensors based on Er-doped UCNP. In addition, the detection of RNA extracted from deactivated clinical sample using this biosensor was also performed with the LOD approaching femtomolar level, indicating the potential clinical application of the as-prepared biosensor. Overall, the results in this work illustrate that this plasmon-enhanced FRET biosensor based on csUCNP could be potential sensing platforms for instant and sensitive virus RNA detection.

Chapter 4 *In vitro* Sonodynamic Antibacterial Applications Based on Yb Doped Bi_2WO_6 Nanosheets

4.1 Introduction

For generations, the unmanageable and detrimental bacterial infection has presented a significant danger to both public health and the economy [128]. While standard antibiotic treatment effectively kills bacteria, its therapeutic efficacy is hindered by the emergence of antibiotic-resistant pathogens, resulting in the failure to remove these infections in clinical settings [128]. As bacteria evolve, they may develop enzymes that prevent antibiotics from entering their cells, modify their membrane barrier and permeability, or create drug efflux pumps to defend themselves from antibacterial drugs [129]. Conquering the difficulty of developing potent antibacterial methods and antibiofilm therapies that do not lead to drug tolerance is a significant objective in the scientific community. Of the several antibiotics-free and non-invasive methods, such as PDT, PTT, and SDT, SDT stands out as the most promising strategy for treating bacterial infections. This is because it has exceptional tissue-penetrating capabilities and is effective against drug-resistant bacteria, including those in biofilms [130].

According to the mechanism of SDT, the efficacy of SDT is highly depends on the amount of generated ROS under the US. Therefore, it is important to design and fabricate sonosensitizers with high ROS generation performance. Zhou et al. reported an oxygen vacancy (OV)-rich WO3−x nanosheets by disposing of metal single-atom

(SA) as a sonosensitizer for SDT [131]. The Cu-WO_{3-x} sonosensitizer has much greater efficacy in generating ROS by ultrasound stimulation compared to both WO_{3-x} and Cu SA-decorated WO_3. Following a modification with polyethylene glycol, the Cu-WO_{3-x} exhibits rapid cytotoxicity against cancer cells in laboratory conditions and successfully eliminates tumors in living organisms when exposed to ultrasound irradiation.

In Chapter 3, we discussed an ultrasensitive biosensor based on UCNPs, which provides an effective way to cut off the spread of infectious pathogens. To further eliminate the pathogens, effective sonodynamic antibacterial treatment is introduced in Chapter 4. This chapter introduces Yb-doped Bi_2WO_6 nanosheets as a sonosensitizer that exhibits excellent performance in generating ROS for antibacterial applications activated by ultrasound. We have effectively produced Bi_2WO_6 nanosheets (NSs) with varying concentrations of Yb doping. Among them, the Bi_2WO_6-10%Yb NSs notably enhanced the quality of reactive oxygen species (ROS) formed when stimulated by ultrasound (US). The DFT calculation further demonstrated that the Bi_2WO_6-10%Yb NSs have a unique structure that enabled the efficient separation of electrons (e^-) and holes (h^+) when exposed to ultrasonic (US) irradiation. Bi_2WO_6-10%Yb NSs, when exposed to ultrasound irradiation, exhibit remarkable in vitro inhibition rates against both gram-negative and gram-positive bacteria. This suggests that they possess a wide range of effectiveness in sonodynamic antibacterial activity. In addition, the process of sonodynamic antibacterial action was extensively examined at the transcriptome level. The Bi_2WO_6-10%Yb NSs discussed in this research are expected to be used in other in vivo sonodynamic antibacterial domains.

4.2 Experimental

4.2.1 Materials

$Bi(NO_3)_3•5H_2O$ (99.99%), $Na_2WO_4•2H_2O$ (ACS, 99.0-101.0%), $Yb(NO_3)_3•5H_2O$ (99.99%), Cetyltrimethylammonium bromide (CTAB), and Glutaraldehyde were obtained from Aladdin. Dimethylsulfoxide (DMSO), 5,5-dimethyl-1-pyrroline-*N*-oxide (DMPO), 2,2,6,6-tetramethylpiperidine (TEMP), and 1,3-diphenylisobenzofuran (DPBF) were purchased from Sigma-Aldrich. LB medium was bought from Beyitime Biotech, Inc. The 2',7'-dichlorodihydrofluorescein diacetate (DCFH-DA) ROS Detection Fluorometric Assay Kit was purchased from Abbkine, Inc. The Live/Dead Bacterial Staining Kit was purchased from BestBio Co., Ltd. All the chemicals were used in their original state without undergoing further purification. The US was DJO Ultrasonic therapy apparatus 2766.

4.2.2 Synthesis of Bi_2WO_6 Nanosheets

Bi_2WO_6 nanosheets were synthesized using the hydrothermal method (Figure 4-1). In a typical synthesis, 25 mg CTAB and 1 mmol of $Bi(NO_3)_3•5H_2O$ were dissolved in 30 ml distilled water before mixing with 10 mL aqueous solution of 165 mg $Na_2WO_4•2H_2O$ (0.5 mmol). Then, the solution was stirred for 30 min and transferred into a 50 mL Teflon liner with the autoclave maintained at 160 ℃ for 20 h. After the autoclave naturally cooled down to room temperature, the precipitates were centrifuged and washed with water and alcohol three times and dried at 60 ℃ for 12 h. For the synthesis of Yb doped Bi_2WO_6 nanosheets, the $Bi(NO_3)_3•5H_2O$ were replaced by

certain molar ratio (1%, 2%, 5%, 10%, 20%) of $Yb(NO_3)_3 \cdot 5H_2O$.

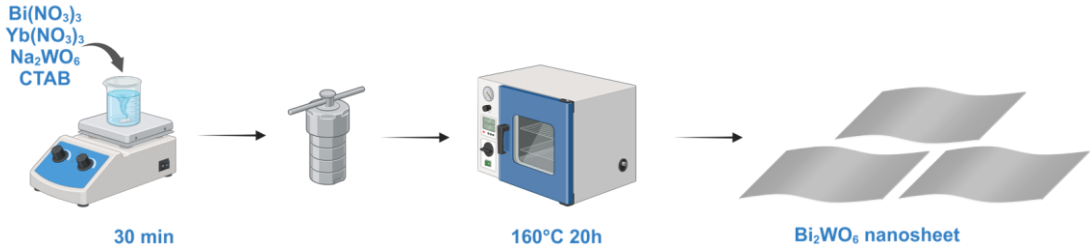

Figure 4-1 Illustration of the synthesize route of BWO-x%Yb NSs.

4.2.3 Preparation of Bacteria Suspension

The MRSA was obtained from the Hong Kong University and the *E. Coli* was obtained from the Hong Kong Polytechnic University Shenzhen Research Institute. The MRSA or *E. Coli* discrete colony was separated from the LB agar plate and incubated in LB medium at 37 °C, 250 rpm overnight, as shown in Figure 4-2. The bacteria cells were collected with the centrifuge (10000 × g, 10 min) and resuspended in PBS for further experiments. The concentration of the bacteria was evaluated using a plate reader and plate counting method (OD_{600}~0.2, 10^8 CFU/mL).

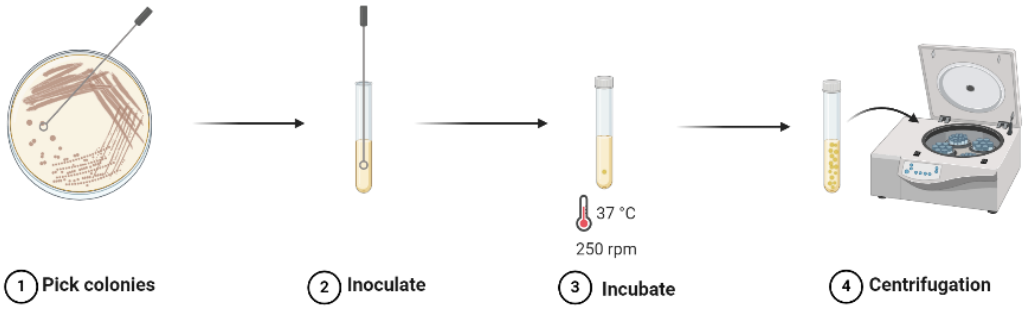

Figure 4-2 The procedure of preparing bacteria suspension.

4.2.4 Detection of ROS

The DPBF was developed as a selective probe to detect and quantify singlet oxygen ($^1O_2$) due to its ability to react with $^1O_2$ in samples and display a decreased absorbance at 420 nm. Briefly, DPBF was dissolved in DMSO to obtain the stock solution at a concentration of 100 μM. Then, 80 μL of sample and 20 μL of DPBF stock solution were added to each well of 96-well plate to obtain a DPBF working concentration of 20 μM. The mixture was balanced in the dark for 10 min and then the 96-well plate was treated with US (1.0 MHz, 1.5 W cm^{-2}, 50% duty cycle). The absorption of DPBF at 420 nm was detected using a plate reader for every 2-minute interval.

An ESR spectrometer was also employed to detect the production of ROS. TEMP was used as a $^1O_2$ trapping agent to assess the generation of $^1O_2$. 30 μL of BWO-10%Yb NSs solution (1 mg mL^{-1}) was added to 30 μL of TEMP (100 mM) solution and subjected to 5 min of US (1.0 MHz, 1.5 W cm^{-2}, 50% duty cycle) and evaluated by ESR spectrometer. For •OH and $•O_2^-$ generation detection, 30 μL of BWO-10%Yb NSs solution (1 mg mL^{-1}) was added to 30 μL of DMPO (100 mM in DI water/methyl alcohol). The mixture was treated with US for 5 min and evaluated by ESR spectrometer.

The in vitro oxidative stress of MRSA cells after US treatment with sonosensitizers was determined by a DCFH-DA ROS Detection Fluorometric Assay. DCFH-DA is a probe that can pass readily across cell membranes, making it ideal for detecting ROS levels inside cells. Once within the cell, the nonfluorescent DCFH-DA will undergo hydrolysis by cellular esterase into DCFH, which could oxidize by ROS to produce

fluorescent DCF. Fluorescence intensity could be detected by flow cytometry, microplate readers, or confocal microscopy and provides insight into the intracellular ROS level. In a typical ROS detection procedure, MRSA cells in PBS and incubated with 10 μM DCFH-DA in the dark for 30 min to load the probe. After that, MRSA cells loaded with DCFH-DA were washed with PBS three times and were resuspended in PBS to obtain a suspension with a concentration of ~10^8 CFU/mL (OD600 = 0.2). Then 100 μL of MRSA suspension was added to 100 μL of PBS, or 100 μL of Bi_2WO_6-10%Yb NSs (1 mg mL^{-1}). The mixture was treated without or with US (1.0 MHz, 1.5 W cm^{-2}, 50% duty cycle) for 5 min. Then 5 μL of the resuspension was placed on a glass slide and examined using a Nikon AXE LASER Confocal microscope. The relative fluorescence at 525 nm was detected with an excitation wavelength of 488 nm.

4.2.5 In Vitro Antibacterial Test

The antibacterial activity of Bi_2WO_6-10%Yb NSs against MRSA and *E. Coli* was evaluated using a plate counting method. First, 50 μL of bacteria suspension (10^6 CFU/ mL) in PBS was added to 50 μL of PBS or Bi_2WO_6-10%Yb NSs (1 mg mL^{-1}). Then the mixture was treated with or without US (1.0 MHz, 1.5 W/cm^2, 50% duty cycle) for 5 min. Bacteria treated with PBS were set as the control group, termed as Control US(-), and Control US(+)), while the bacteria treated with Bi_2WO_6-10%Yb NSs are termed as Bi_2WO_6-10%Yb US(-) and Bi_2WO_6-10%Yb US(+), respectively. After different treatments, the bacteria suspensions were diluted with PBS (1:1000) and 100 μL of the diluent was evenly coated on an LB agar plate and cultured at 37 °C for 24 h.

The antibacterial ratio was evaluated by the number of colonies formed and calculated using the following formula:

$$\text{Antibacterial ratio}(\%) = (A - B) * 100 / A \quad (1)$$

"A" represented the number of colonies formed on the LB agar plate in the control group, while "B" represented the number of colonies in the experimental group.

4.2.6 SEM of Bacteria Morphology

In addition, the SEM was used to observe the integrity of the treated bacterial membrane. Briefly, the preliminary treatment procedure was the same as the plate counting method. The treated MRSA cells in each group the treated MRSA cells were collected by centrifugation at 10,000 × g for 10 minutes and then fixed with 2.5% glutaraldehyde for 2 h and dehydrated continuously in gradient ethanol solution (30%, 50%, 70%, 90%, and 100%) for 15 min each. Finally, the samples were air-dried and observed under SEM.

4.2.7 Live/Dead Staining

Live/dead staining for MRSA was performed according to the protocols of a commercial BBcellProbe N01/PI staining kit. The preliminary treatment procedure was the same as the in vitro antibacterial test. The treated MRSA cells were collected by centrifugation at 10,000 × g for 10 minutes and washed with 0.85% NaCl 3 times. Then the MRSA cells were resuspended in 100 μL of staining working solution and incubated in the dark for 15 min. After washed and resuspend in 0.85% NaCl, 5 μL of the

resuspension was placed on a glass slide and examined using a Nikon AXE LASER Confocal microscope. The Excitation/Emission wavelength for live and dead bacteria was 488/525 nm and 540/620 nm, respectively.

4.3 Characterization of Yb-doped Bi_2WO_6 Nanosheets

BWO-x%Yb NSs with different Yb doping concentrations (1%, 2%, 5%, 10%, and 20%) were fabricated by varying the initial feeding ratio of $Yb(NO_3)_3$, named as BWO-1%Yb, BWO-2%Yb, BWO-5%Yb, BWO-10%Yb, and BWO-20%Yb, respectively. Herein, the morphology and structures of the BWO and BWO-10%Yb NSs were examined using TEM, SEM, and XRD for representation. The TEM image demonstrates that the prepared BWO (Figure 4-3(a)) and BWO-10%Yb NSs (Figure 4-3(b)) both process a consistent nanosheet morphology with a dimension ranging from 100 to 200 nm. The high-resolution TEM (HRTEM) image of the BWO-10%Yb NSs displays a continuous lattice fringe, proving conclusive confirmation of its single crystalline structure, as shown in Figure 4-4(a). The determined lattice distance is approximately 0.27 nm, especially corresponding to the (2 0 0) planes of the orthorhombic phase of BWO crystal. In addition, the single-crystalline nature of BWO-10%Yb nanosheets was further verified by the selected area electron diffraction (SAED) pattern (Figure 4-4(b)). The images of element mapping in Figure 4-4(c) also confirmed that Bi, W, O, and Yb were evenly distributed throughout the BWO-10%Yb NSs, providing evidence of the successful doping of Yb. The SEM image revealed that BWO and BWO-10%Yb NSs exhibited a characteristic two-dimensional nanosheet structure,

with the majority of the nanosheets displaying rectangular shapes. (Figure 4-5). Moreover, XRD analysis showed that all the characteristic diffraction patterns were well consistent with the orthorhombic phase of Bi_2WO_6 (PDF#39-0256) (Figure 4-6). The peaks of the BWO-x%Yb NSs were slightly shifted to a smaller angle when compared to the undoped BWO NSs. The shift grew more pronounced with increasing Yb doping concentration, suggesting that the addition of Yb to the BWO lattice raised the lattice constant since the atomic radius of Yb is larger than Bi. The surface element chemical state of BWO and BWO-10%Yb NSs was analyzed by X-ray photoelectron spectroscopy (XPS). The survey XPS spectra of BWO-10%Yb NSs confirmed the existence of Bi, W, O, and Yb elements (Figure 4-7(a)), the peak at 188.18 eV in the inset of Figure 4-7(a) was assigned to the binding energy of Yb 4d. The high-resolution XPS spectra of Bi 4f, O 1s, and W 4f with fitted curves are displayed in Figure 4-7(b-d). The XPS high-resolution spectra of O 1s in Bi_2WO_6 NS exhibited two major peaks at 529.81 eV and 530.94 eV, attributed to the lattice oxygen and bridging hydroxyls, respectively (Figure 4-7(c)).[132] . Besides, the peaks of Bi 4f (Bi $4f_{7/2}$ 159.15 ev and Bi $4f_{5/2}$ 164.46 eV) and W 4f (W $4f_{5/2}$ 35.43 ev and W $4f_{7/2}$ 37.57 eV) of BWO-10%Yb NS slightly shifted to higher energy compared with pure Bi_2WO_6 NS, because Yb might change the chemical environment of Bi and W in Bi_2WO_6 NS.

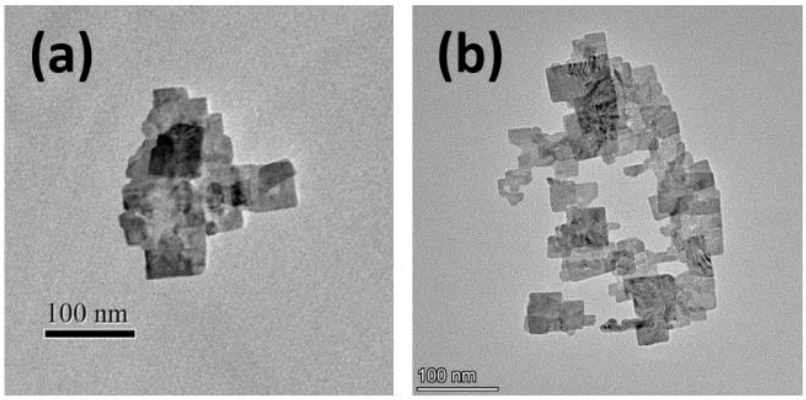

Figure 4-3 TEM image of (a) BWO NSs; (b) BWO-10%Yb NSs.

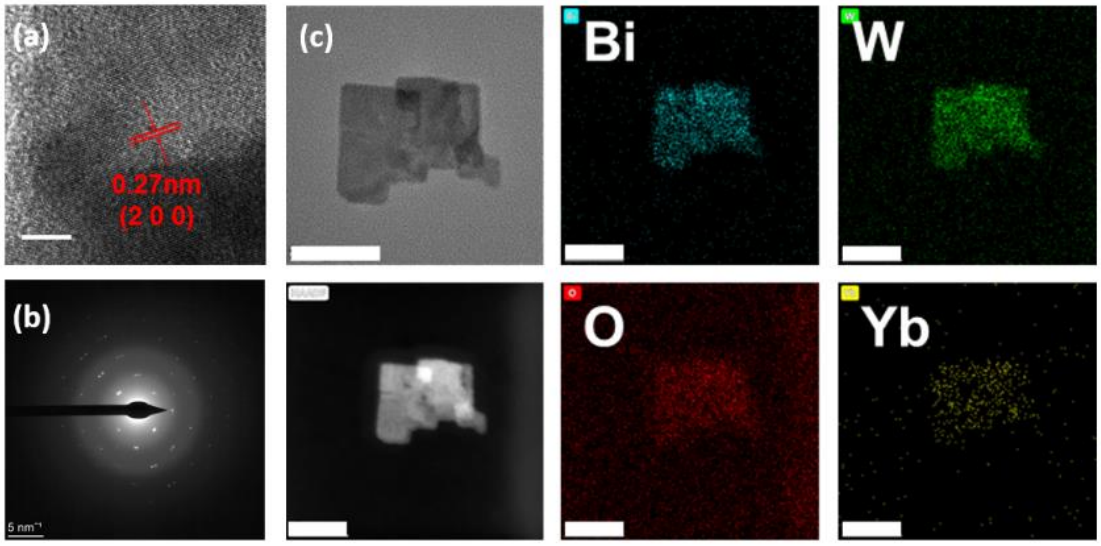

Figure 4-4 (a) HRTEM image of BWO-10%Yb NSs, scale bar: 5 nm; (b) Selected area electron diffraction (SAED) pattern; (c) corresponding element mapping images (Bi, W, O, and Yb) of BWO-10%Yb NSs.

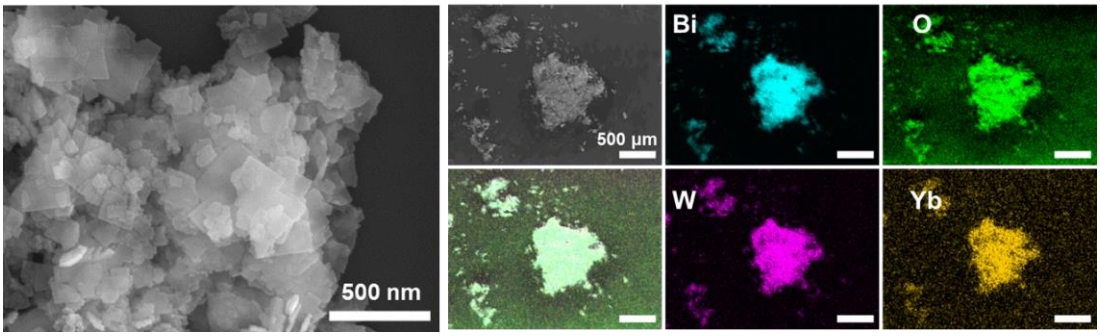

Figure 4-5 SEM image of BWO-10%Yb NSs and the corresponding EDX element mapping.

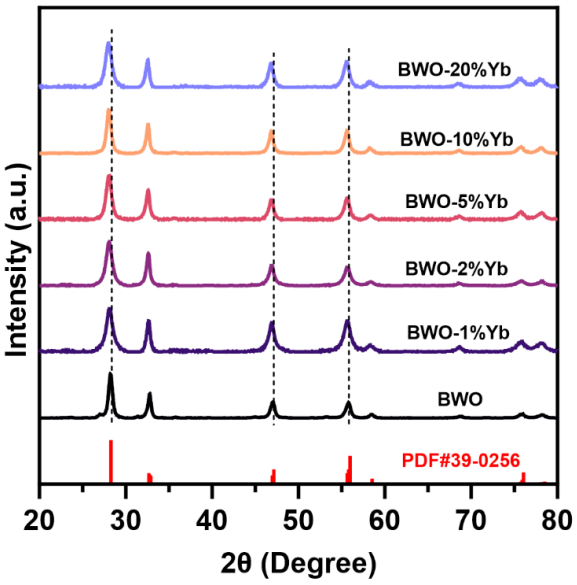

Figure 4-6 XRD spectrum of BWO NSs and BWO-x%Yb NSs.

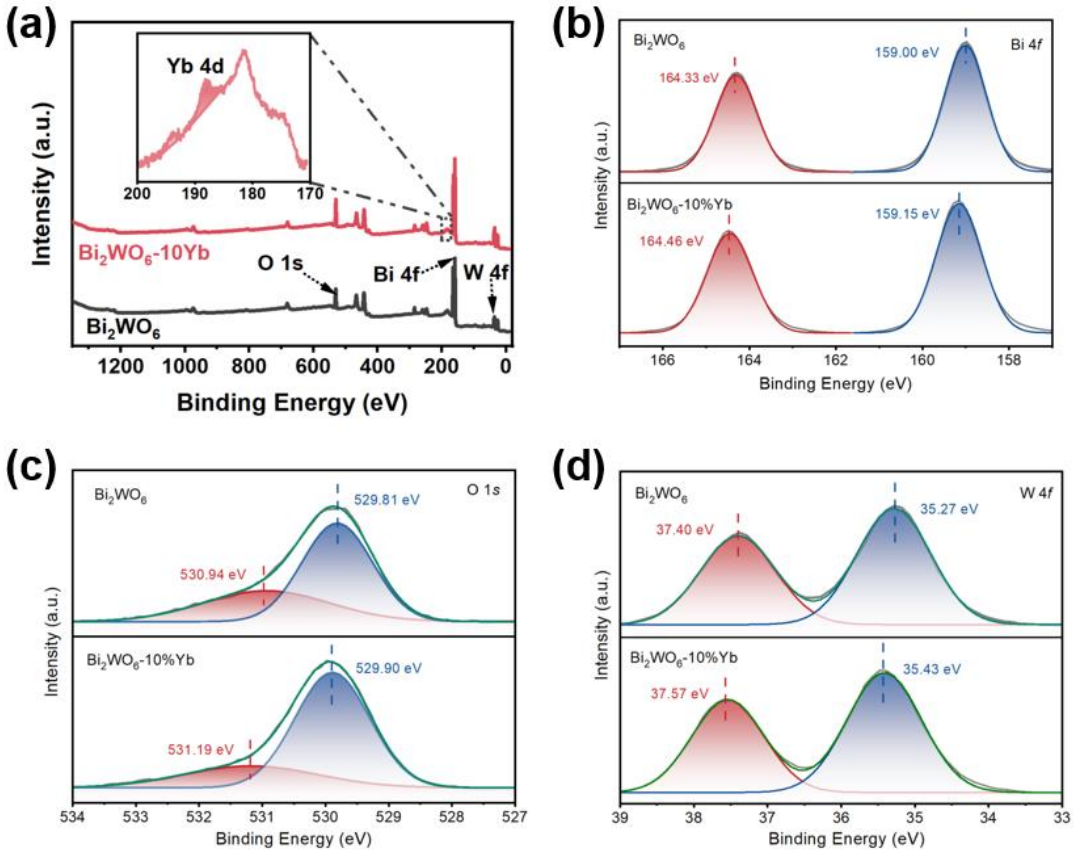

Figure 4-7 (a) XPS spectra of BWO and BWO-10%Yb NSs. The inset is the high-resolution XPS spectra of Yb 4d. High-resolution XPS spectra of BWO and BWO-10%Yb NSs, b) Bi 4*f*, c) O 1*s*, d) W 4*f*.

The oxygen defect was further investigated using electron spin resonance (ESR) spectroscopy. As displayed in Figure 4-8Figure 4-8 ESR spectra of BWO and BWO-10%Yb NSs.. Both BWO and BWO-10%Yb NSs are distinguished by their symmetrical ESR signal at g = 2.003, indicating electron trapping at OVs. The ESR results demonstrate that both BWO and BWO−x%Yb NSs possess few OVs.

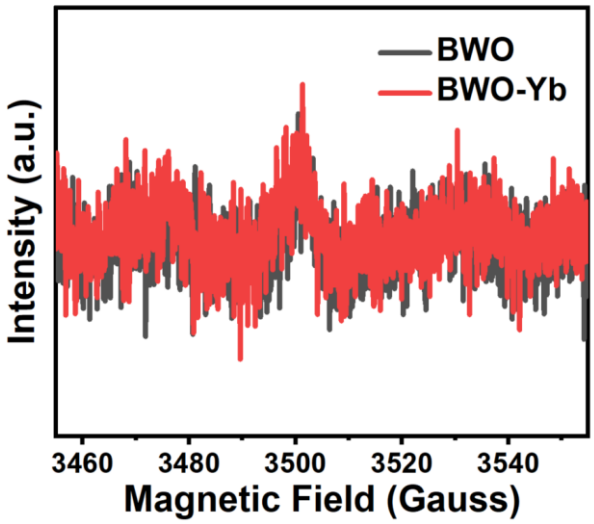

Figure 4-8 ESR spectra of BWO and BWO-10%Yb NSs.

4.4 The ROS Generation Performance and Mechanism

The catalytic activities of BWO and BWO−x%Yb NSs as sonosensitizers for generating reactive oxygen species (ROS) under US treatment (1.5 W/cm^2, 50% duty cycle, 1 MHz) were first examined using 1,3-Diphenylisobenzofuran (DPBF) as singlet oxygen ($^1O_2$) probe. It was anticipated that the presence of $^1O_2$ would result in a reduction in the absorption of DPBF at 420 nm. As shown in Figure 4-9(a) and (b), the groups exposed to US irradiation exhibited a more pronounced and rapid decline in the absorption at 420 nm compared to the groups that were not exposed to the US, suggesting the production of $^1O_2$ occurred at a higher rate in the US-triggered groups. Significantly, BWO−10%Yb NSs demonstrate the most rapid decline, with a fall of more than 50% within 10 minutes of ultrasound irradiation (Figure 4-9(b)), which indicates that BWO-10%Yb NSs possess a greater capacity to generate $^1O_2$ compared

to BWO and other BWO-x%Yb NSs. Therefore, the doping of Yb at a concentration of 10% can significantly enhance the SDT performance of the sonosensitizer. Subsequently, the DPBF probe was also employed to investigate the optimized concentration of BWO-10%Yb NSs for generating ROS under US irradiation. The concentration of BWO-10%Yb NSs at 200 μg/mL, 500 μg/mL, 1 mg/mL, and 2 mg/mL are compared here. Figure 4-9(d) demonstrates that a significant reduction in absorption at 420 nm occurred after 10 minutes of US irradiation at the BWO-10%Yb NSs concentration of 500 μg/mL, indicating the BWO-10%Yb NSs produced the highest amount of $^1O_2$ at this particular concentration. Therefore, 500 μg/mL of BWO-10%Yb NSs was used as the sonosensitizer for further sonodynamic antibacterial investigations.

Furthermore, the generation of the specific ROS, •OH, $^1O_2$, and O_2^-, were confirmed by ESR spectroscopy (Figure 4-10) using 2,2,6,6-tetramethyl-4-piperidone (TEMP) and 5,5-Dimethyl-1-Pyrroline-N-Oxide (DMPO) as spin-trapping agents. The results revealed that BWO-10%Yb NSs demonstrated a robust •OH signal and somewhat lower signals for $^1O_2$ and O_2^- when exposed to US irradiation, while no signal was detected without US irradiation, indicating excellent sonodynamic performance for generating ROS. Therefore, the above-mentioned findings demonstrate the solid capacity of BWO-10%Yb NSs as a sonosensitizer to generate ROS when exposed to US irradiation and its significant potential for sonodynamic therapy.

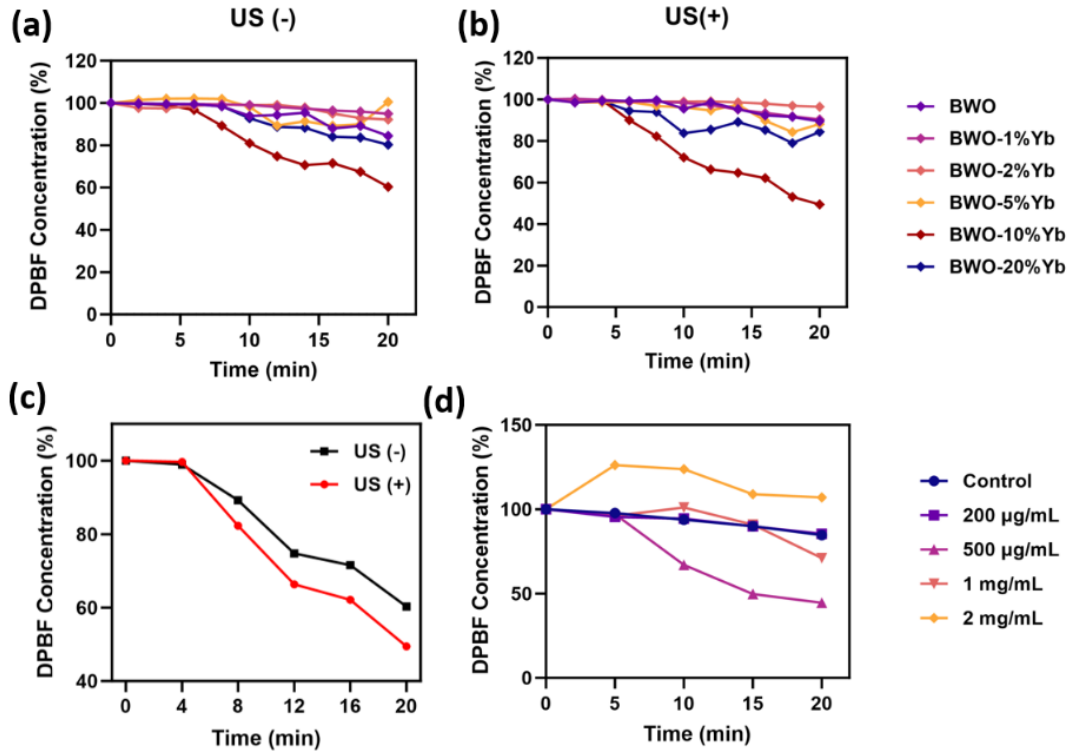

Figure 4-9 Absorption intensity changes of DPBF in BWO-x%Yb NSs (a) without and (b) with the US irradiation. (c) Absorption intensity changes of DPBF in BWO-10%Yb NSs. (d)Absorption intensity of DPBF with different concentrations of BWO-10%Yb NSs under the US irradiation.

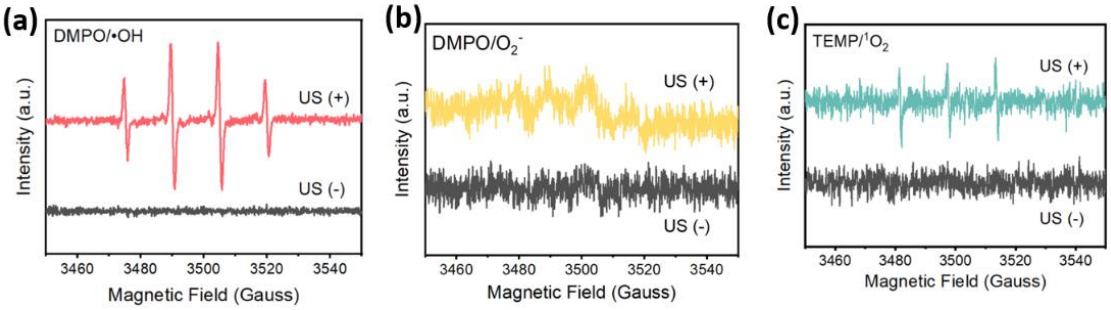

Figure 4-10 ESR spectra of (a) •OH and (b) $\bullet O_2^-$ trapped by DMPO, (c) $^1O_2$ trapped by TEMP of BWO-10%Yb NSs.

In order to obtain physical insights onto the enhanced SDT performance of BWO upon Yb-doping, DFT simulation was then carried out. First, the preferential occupation of Yb into the BWO lattice is investigated by comparing the defect formation energy:

$$E^f[X^q] = E_{tot}[X^q] - E_{tot}[bulk] - \sum n_i\mu_i + qE_F + E_{corr}$$

where $E^f[X^q]$ is the defect formation energy of the defect with P charged. $E_{tot}[X^q]$ and $E_{tot}[bulk]$ represent the total energy of the doped structure and the pristine lattice, respectively. μ_i is the chemical potential, which is derived from the corresponding substance in conventional phases, *i.e., fcc* Yb for μ_{Yb}, R-3m Bi for μ_{Bi}, bcc W for μ_W and oxygen molecule for μ_O. E_F is the Fermi level. E_{corr} is the finite-size correction energy. Based on a 2x2x1 supercell of BWO, in total 16 cases of different Yb-doping configuration were considered (Figure 4-11(a)), such as Yb incorporating Bi site (denoted as YbBi) or Yb substituted a W atom and generate one VO for charge compensation (denoted as YbW-VO). All the cases agree on an energetically preferred Yb-Bi substitution despite the different doping concentration. Following the doping configuration with the lowest formation energy, it is then found that such Yb-Bi substitution can effectively reduce the bandgap of pristine BWO as compared in Figure 4-11(b). Further increasing the Yb-doping concentration (two Yb replacing two Bi atoms, yielding a 12.5 at.% doping concentration) cause little reduction, yet it leads to further band splitting in the conduction band (CB) minimum. A widened CB may potentially facilitate the absorption of a wider energy range during the SDT process. In summary, the introduction of Yb into energetically favored Bi site

leads to the reduced band gap and widened CB, ascribing to a better SDT performance.

Furthermore, we discovered that Yb substitution is beneficial to the SDT process in terms of better H_2O adsorption. The preliminary calculation shows that Yb tends to be incorporated at the surficial Bi-O layers of the BWO NSs with relatively large local distortion, which agrees with similar reports in doped nanosheets. The surface energies (γ) of H_2O adsorbed on different surface sites (models schematically shown in Figure 4-11(d)) of BWO NS were then calculated as follow:

$$\gamma = \frac{E_{slab} - NE_{bulk} - E_{H_2O}}{2A}$$

Where E_{slab} is the total energy of the surface model and E_{bulk} is the total energy for the corresponding bulk structure, N is the supercell number, E_{H_2O} is the energy of water, and A is the surface area of the structure.

As summarized in Figure 4-11(e), the lowest γ value was obtained from the case where H_2O is intentionally adsorbed on the surface Yb. All other cases also show a clear trend where the γ become larger as H_2O was adsorbed away from Yb. Such a global minimum spot of H_2O adsorption means not only an easier way for BWO to capture H_2O and trigger the SDT process but also an optimized mass transmission pathway over the BWO surface. The CCD can provide a closer insight into the enhanced bonding interaction between H_2O and Yb rather than Bi. Four representative adsorption schemes were selected, and the CCD diagrams were plotted based on the following equation:

$$\rho_{diff} = \rho(BWO \cdot H_2O) - \rho(BWO) - \rho(H_2O)$$

Where $\rho(BWO \cdot H_2O)$, $\rho(BWO)$, and $\rho(H_2O)$ are the charge density of the

H_2O-adsorbed BWO, empty BWO, and H_2O structure, respectively. These CCD figures are shown in Figure 4-11 and Figure 4-12.

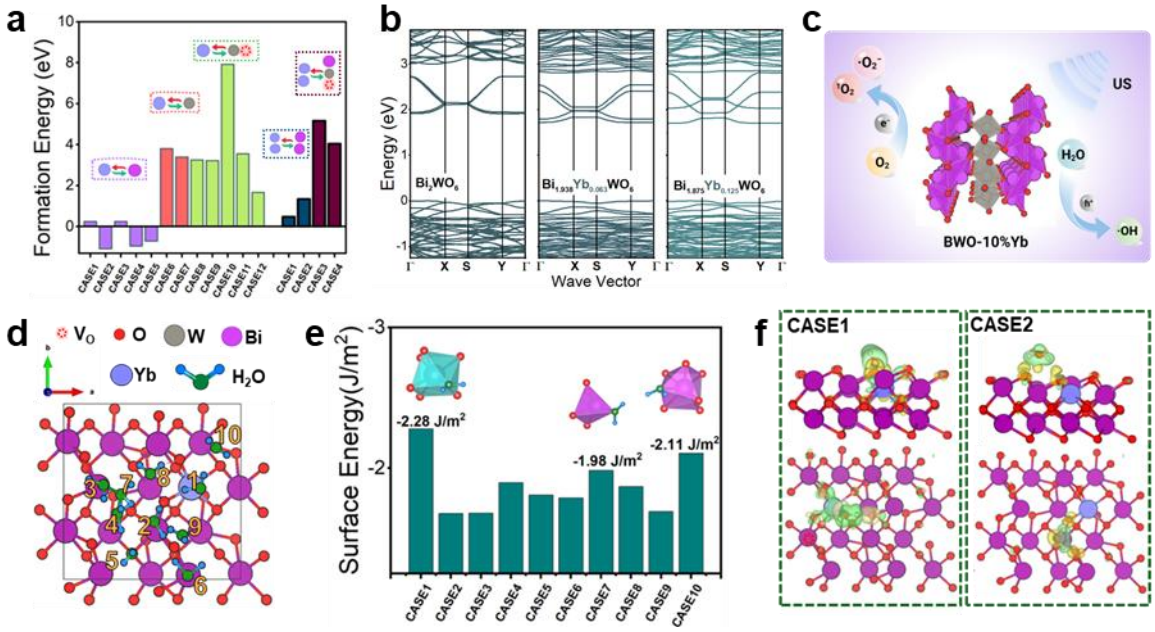

Figure 4-11 a) Defect formation energy of different Yb-doping configurations in BWO, the involved ion substitution in each calculation is marked. b) Evolution of electronic band structure upon Yb doping. c) Schematic illustration of the generation of ROS by US-triggered BWO-10%Yb NSs. d) Crystal structure of BWO-Yb NSs and the surface H_2O absorption sites, viewing along the *c* axis. e) The surface energy of H_2O absorbed at different surface sites. f) The calculated CCD diagram of H_2O absorbed on surface site 1 and 2 of BWO-Yb as indicated in (d), the yellow and green regions depict the electron accumulation and depletion, respectively.

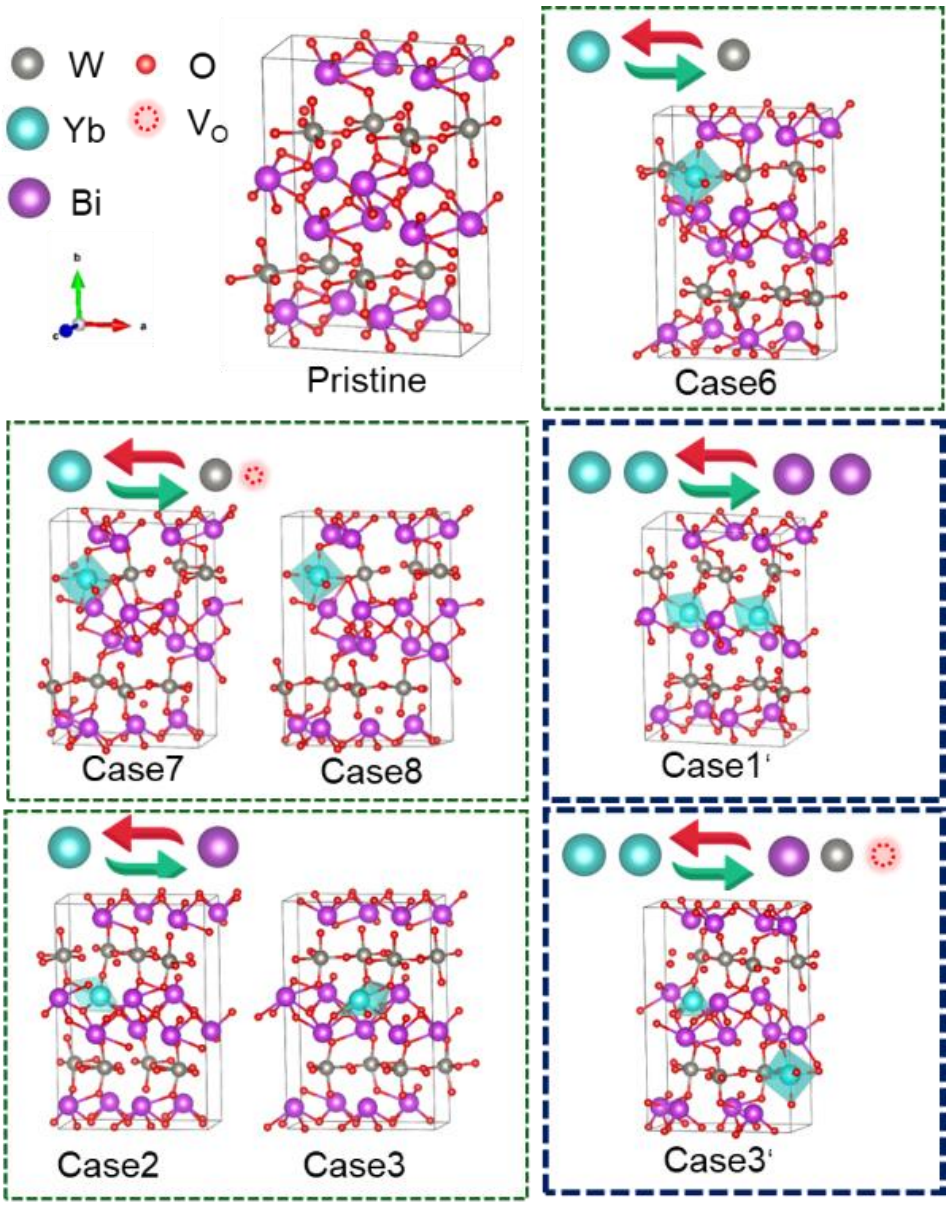
W
O
Yb
V_O
Bi
Pristine
Case6
Case7
Case8
Case1'
Case2
Case3
Case3'

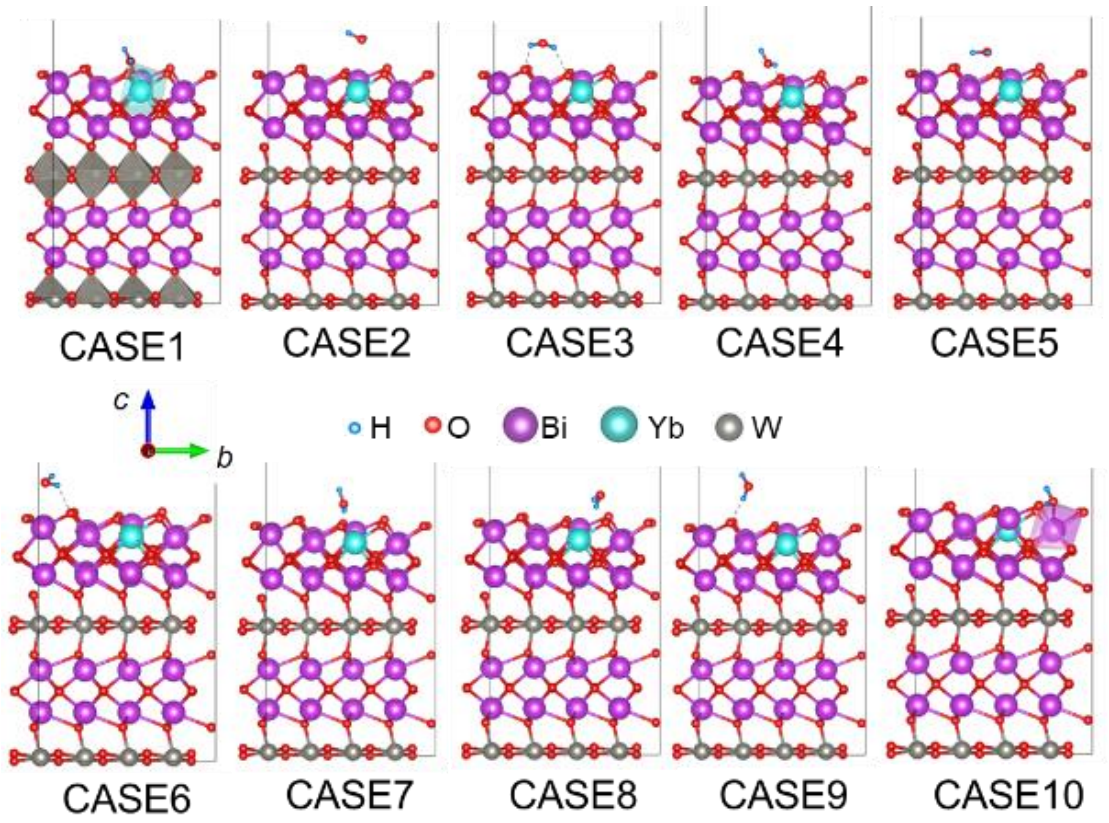

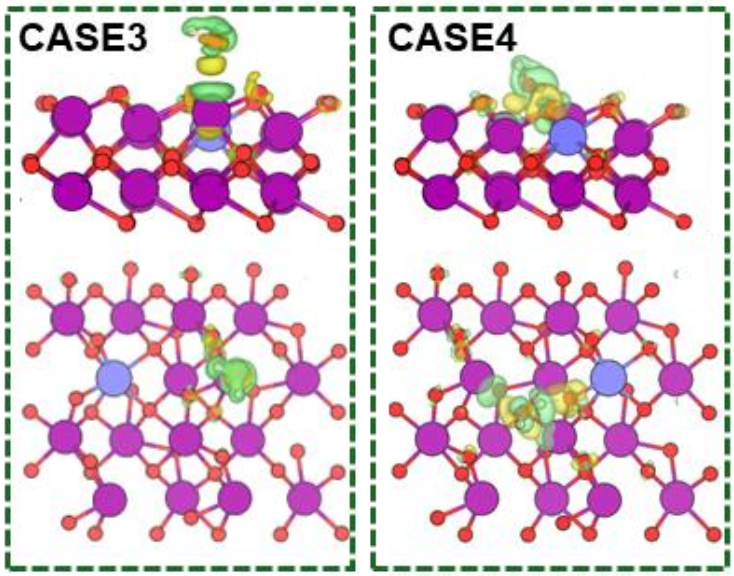

Figure 4-12 CDD diagram of different configurations.

4.5 In vitro Sonodynamic Antibacterial Performance

The sonodynamic bactericidal performance of BWO-x%Yb NSs as sonosensitizer was determined by counting the bacteria colony forming units (CFU) spread on the LB agar plate after different treatments. The concentration of bacteria in each group is 10^6 CFU/mL and the suspensions after different treatments were diluted in the same multiple before spread on the plate. The US power applied in all the in vitro antimicrobial experiments is 1.5 W/cm^2, 50% duty cycle, 1 MHz. The sonodynamic bactericidal performance of BWO NSs and BWO-10%Yb NSs as sonosensitizer was first examined using the time-dependent plate counting assay, with US irradiation performed 0, 2, 4, 6, 8, and 10 minutes respectively (Figure 4-13). The number of MRSA cells on the plate before exposure to US (0 min) is similar in both BWO NS and BWO-10%Yb NS groups, suggesting that the initial concentration of MRSA cells remains comparable in both groups. After being exposed to 6 minutes of US irradiation, the group of BWO-10%Yb NSs as sonosensitizer achieved a 100% antibacterial rate against MRSA, while the BWO NSs as sonosensitizer required 10 minutes in comparison (Figure 4-13). This provides evidence that 10%Yb-doped BWO NSs demonstrates a superior sonodynamic bactericidal performance compared to BWO NSs owing to the greater production of ROS.

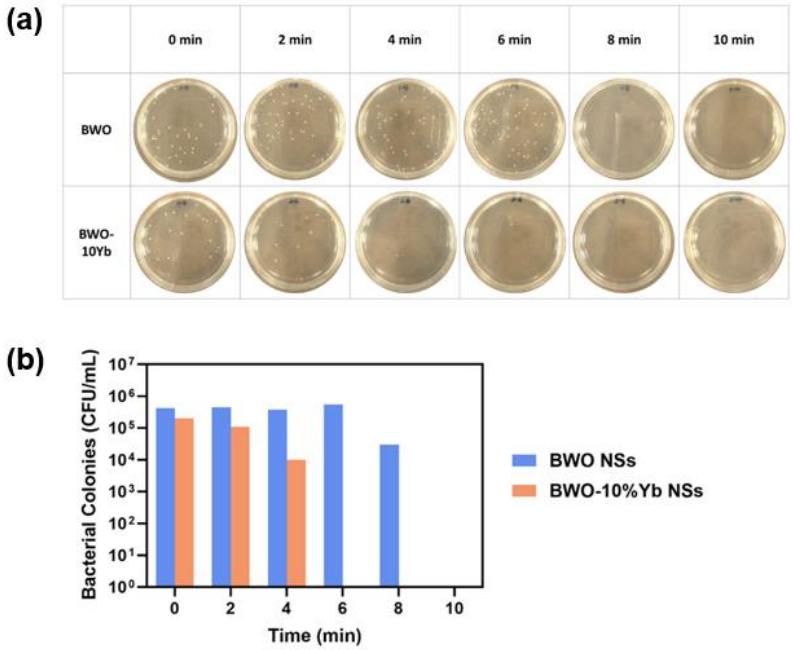

Figure 4-13 Time-dependent sonodynamic bactericidal performance of BWO and BWO-10%Yb NSs as sonosensitizer. (a) Picture of plates with MRSA cells after exposure to different times of US. (b) Corresponding bacteria colonies in different groups.

Subsequently, the broad-spectrum sonodynamic bactericidal performance of BWO-10%Yb NSs as sonosensitizer was examined on gram-positive and gram-negative bacteria. Herein, the Methicillin-resistant *Staphylococcus aureus* (MRSA) was chosen as the representative gram-positive bacteria and *Escherichia coli* (E. coli) was the representative gram-negative model, respectively. The US irradiation time for gram-positive MRSA is 5 minutes, whereas for gram-negative *E. coli* it is 10 minutes, owing to the distinct structures of the bacteria. Figure 4-14(a) demonstrates that there were no discernible bactericidal effects in any of the control groups (C US(-), C US(+), and

BWO-10%Yb US (-)), as evidenced by the presence of visible colonies of MRSA and *E. coli* cells on the LB agar plate. Nevertheless, both MRSA and *E. coli* were eliminated in the groups subjected to BWO-10%Yb NSs and US (BWO-10%Yb US (+)). The concentration of MRSA and *E. coli* remained constant at 10^6 CFU/mL in the control groups and reduced to 0 CFU/mL in the presence of BWO-10%Yb NSs and US (Figure 4-14(b)). The results confirmed the exceptional antibacterial efficacy of BWO-10%Yb NSs as a sonosensitizer in the treatment of both gram-positive and gram-negative bacteria.

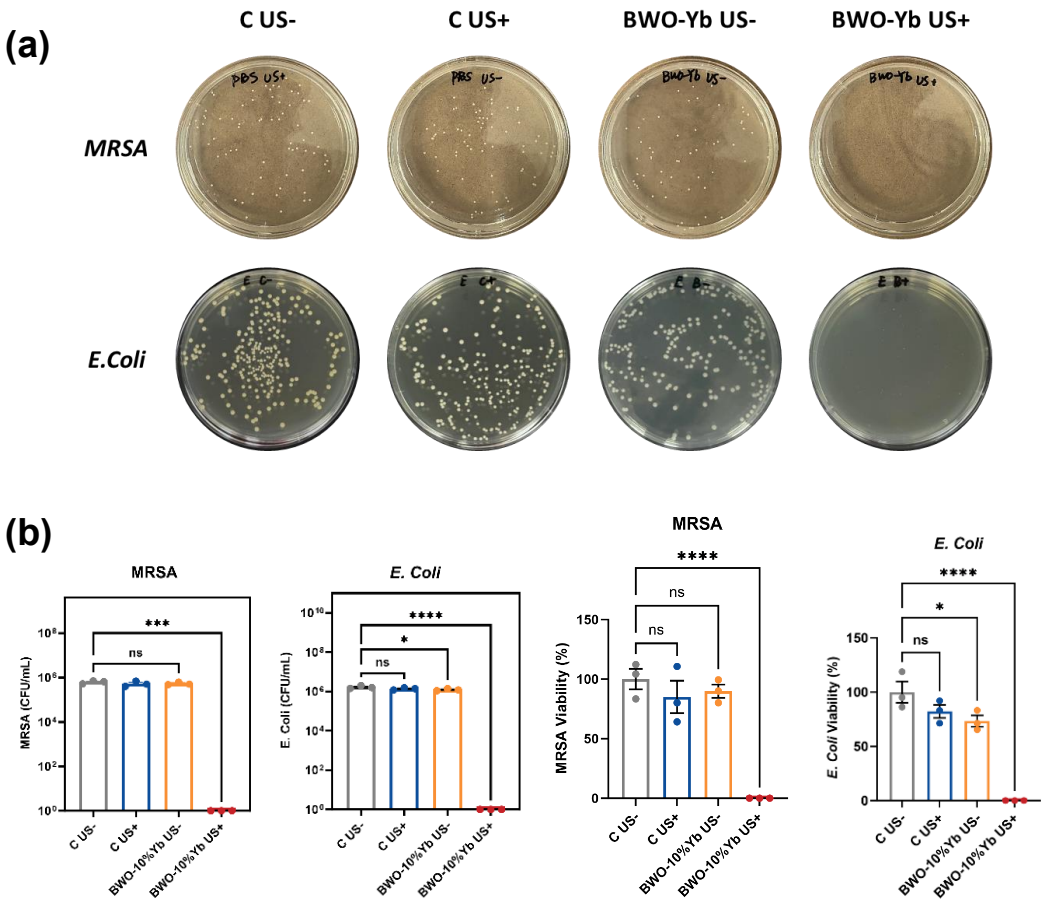

Figure 4-14 Sonodynamic bactericidal performance of BWO-10%Yb NSs. a) Pictures

of MRSA (first row) and *E. coli* (second row) colonies coated on LB-agar plates after different treatments. Corresponding bacterial colonies of MRSA (b) and *E. Coli* (c) in different groups. Corresponding with bacterial viability of MRSA (d) and *E. Coli* (e) in different groups. The error bars indicate mean ± SEM. The statistical analysis was performed using one-way ANOVA with Tukey's multiple-comparisons test: *$p < 0.05$, **$p < 0.01$, ***$p < 0.001$, and ****$p < 0.0001$; ns: not significant ($p > 0.05$).

Then the antibacterial efficacy of BWO-10%Yb NSs under US irradiation was evaluated by conducting live/dead dual-color fluorescent staining and observed through a confocal laser scanning microscope (CLSM) (Figure 4-15(a)). Most of the MRSA cells treated with PBS, US only, and BWO-10%Yb NSs only were able to remain alive (green), with quantitative analysis indicating survival rates of 90.8%, 84.5%, and 83.4%, respectively (Figure 4-15(b)). On the contrary, the majority of MRSA cells exposed to BWO-10%Yb NSs and US were nonviable (red), with a significantly reduced survival rate of merely 33.3%. These findings were consistent with the results obtained from the spread plate counting analysis.

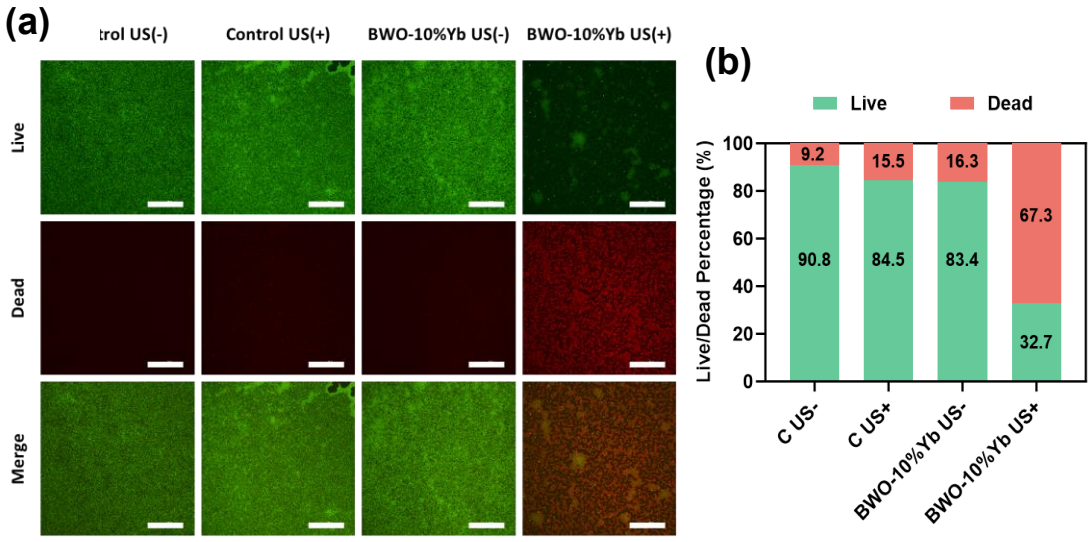

Figure 4-15 (a) Fluorescent images of live (green) and dead (red) MRSA after treatment by different samples without (US (−)) or with (US (+)) US. Scale bars: 50 μm. (b) Corresponding quantitative analysis of live/dead fluorescent intensity.

In addition, the MRSA cells in different groups were fixed after treatment and their morphology was investigated with SEM (Figure 4-16(a)). The morphology of MRSA in the control group treated without US (C US(-)) possessed a typical spherical morphology and smooth appearance, while in the group treated with US only (C US (+)), MRSA cells remained undamaged but processed a tiny indentation on the surface, indicating minimal mechanical damage caused by US irradiation. Similarly, the MRSA bacteria treated solely with BWO-10%Yb NSs (BWO-10%Yb US (-)) preserve their structural integrity, with BWO-10%Yb NSs adhering to their surface. As for the MRSA treated with BWO-10%Yb NSs and US (BWO-10%Yb US (+)), the bacteria exhibited a far more pronounced wrinkling and concave shape, and some membranes were entirely fragmented (red arrows). The high-resolution SEM images of MRSA treated

with BWO-10%Yb NSs and US were also captured and displayed in Figure 4-16(b). the HRTEM image of the MRSA cells clearly demonstrates the broken cell membrane with BWO-10%Yb NSs attached on the surface.

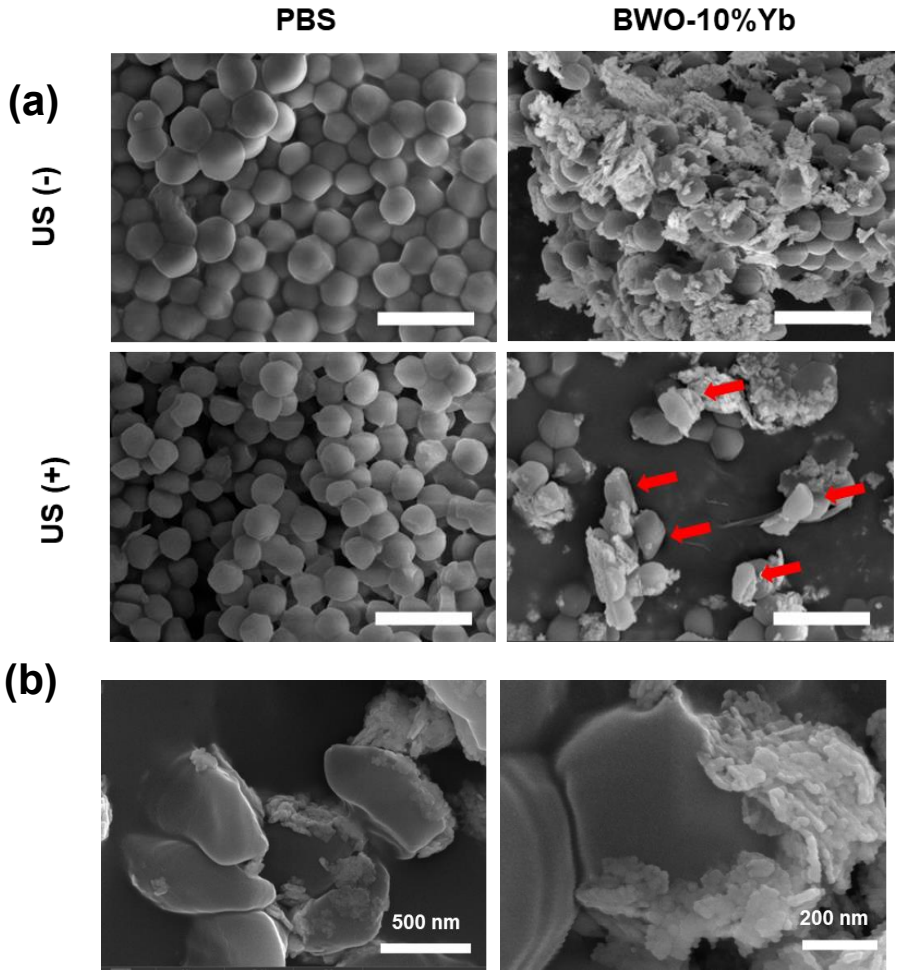

Figure 4-16 (a) SEM images of MRSA cells after different treatments. Scale bars: 2 μm. Red arrows denote morphological damage in MRSA. (b) High-resolution SEM of MRSA cells in BWO-10%Yb NSs US(+) group.

To further verify the ROS-induced bacterial mortality, the ROS generation was evaluated in vitro by a ROS detection assay 2',7'-Dichlorodihydrofluorescein diacetate

(DCFH-DA). In a typical ROS detection assay, DCFH-DA was loaded into living MRSA cells and hydrolyzed by intracellular esterase to produce DCFH. After subjecting MRSA cells to different treatments, the ROS can oxidize non-fluorescent DCFH to fluorescent 2′7′-dichlorofluorescein (DCF). The fluorescent intensity of DCF serves as an indicator of ROS level. From Figure 4-17, the groups treated with PBS, US only and BWO-10%Yb NSs exhibit feeble signals, whereas the group treated with BWO-10%Yb NSs and US exhibited intensive green fluorescent signal of DCF, demonstrating the high ROS generation efficiency of BWO-10%Yb NSs under US irradiation.

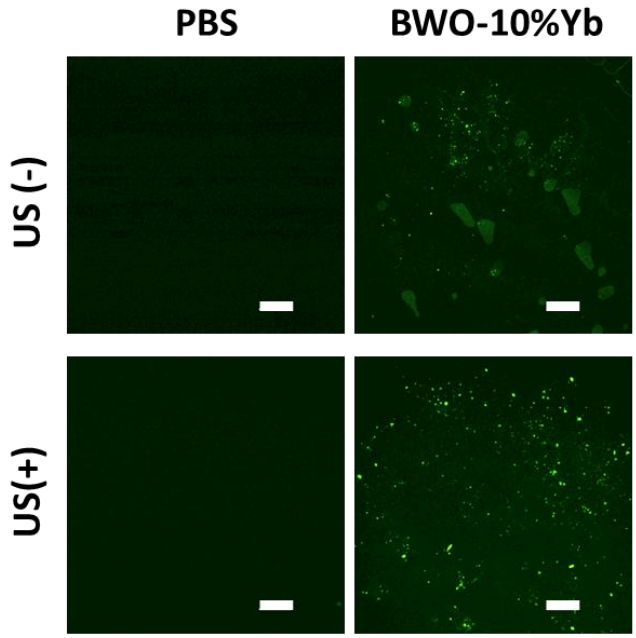

Figure 4-17 The fluorescence image of MRSA stained with DCFH-DA in different groups. Scale bars: 200 μm.

Therefore, the SEM and ROS detection result provided significant evidence that

the excessive ROS generated by the combination of US and BWO-10%Yb NSs sonosensitizer triggered lipid peroxidation and led to the disruption of the bacterial membrane.

4.6 RNA Sequencing

The RNA sequencing transcriptome analysis was conducted with MRSA treated with PBS (Control) and BWO-10%Yb NSs + US to acquire further understanding of the biological mechanism of the sonodynamic antimicrobial activities. Figure 4-18(a) reveals that out of 2470 genes that were co-expressed in the control and BWO-10%Yb NSs + US groups, 24 genes were present only in the control group, and 98 genes were expressed mainly in the treatment group, revealing that the BWO-10%Yb NSs + US significantly affected gene expression compared to the control group. In addition, the Volcano Plot in Figure 4-18(b) demonstrates the statistical significance ($|\log_2 \text{FoldChange}| > 1$, p-adjust < 0.05) in gene expression levels in the two groups. A total of 245 differentially expressed genes (DEGs) were identified in the control and BWO-10%Yb NSs + US groups, consisting of 130 up-regulated genes and 115 down-regulated genes, indicating a rather substantial cellular response in BWO-10%Yb NSs + US group. The heatmap of all the DEGs is shown in Figure 4-18(c). To determine the specific functions of these DEGs, gene ontology (GO) term classification analysis was carried out across biological processes (BP), cellular components (CC), and molecular function (MF) terms (Figure 4-19). Significant changes in biological processes include the organic substance metabolic process, primary metabolic process, and cellular

metabolic process. Significant cellular components from GO terms included the membrane, cytoplasm as well as the extracellular region. Significant molecular functions from GO terms included heterocyclic compound binding, ion binding, transferase activity, and catalytic activity.

Then the enrichment analysis of the Kyoto Encyclopedia of Genes and Genomes (KEGG) pathways was conducted and the top 20 KEGG pathways of the up-regulated and down-regulated genes are depicted in Figure 4-20. The up-regulated DEGs are allocated to pyrimidine metabolism, fatty acid degradation and so on. The downregulated DEGs are enriched in pyruvate metabolism, glycerolipid metabolism, two-component system and so on. Notably, the downregulated two-component signal transduction system (TCS) governs a variety of bacterial physiological processes, strongly related to bacterial metabolism and pathogenicity.

Moreover, the heatmap of the genes involved in these pathways demonstrated strong consistency across the samples within the group, and a significant distinction between the BWO-10%Yb NSs + US and the control group (Figure 4-21) and the heatmap of all the DEGs is shown in Figure 4-18(c). These results suggest that the expressions of MRSA genes are considerably affected by BWO-10%Yb NSs + US.

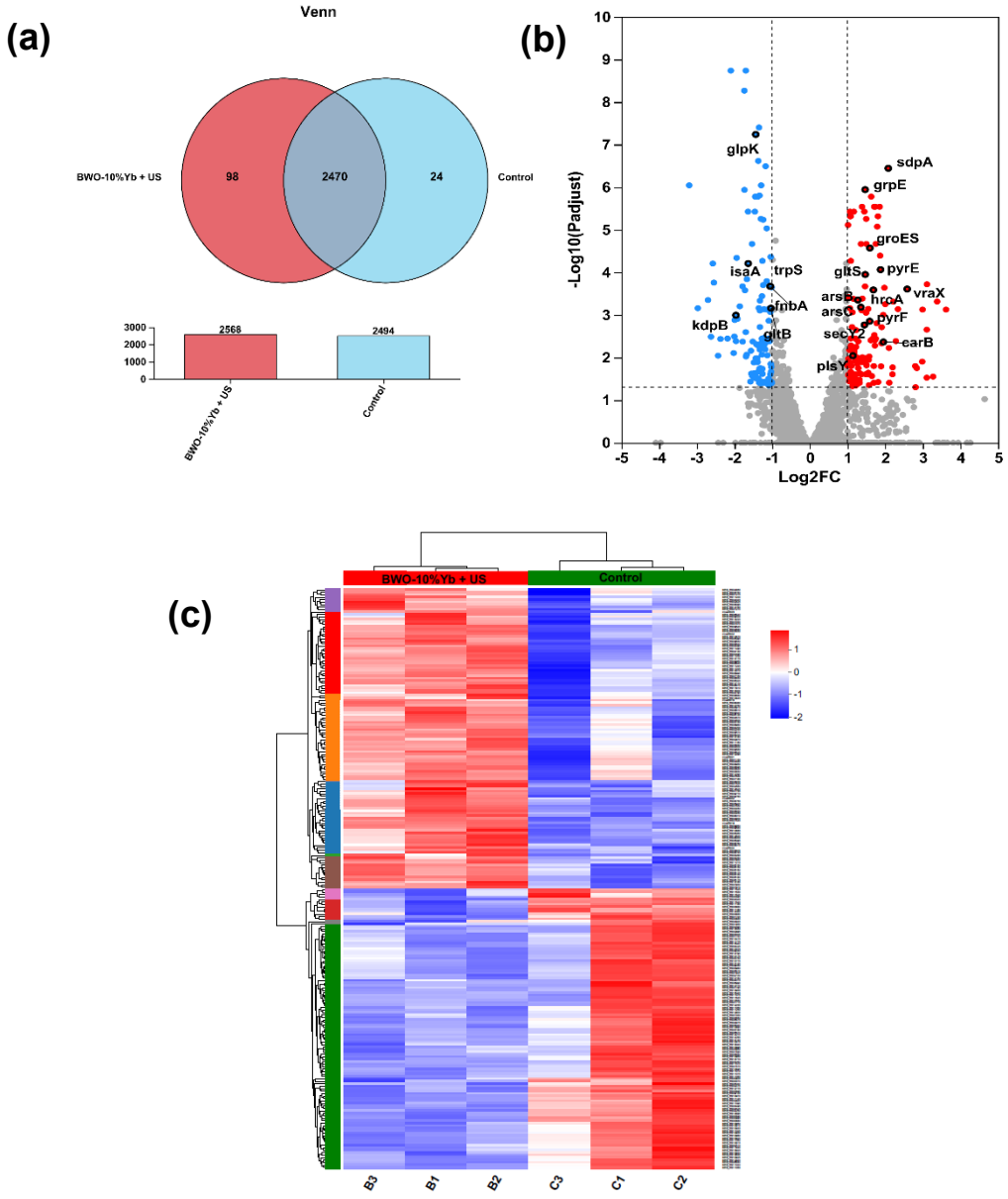

Figure 4-18 (a) Venn diagram of the identified differentially expressed genes in different groups. (b) Volcano plot showing 245 differentially expressed genes of MRSA in BWO-10%Yb+US group compared the control group. Differentially expressed genes were defined as a threshold with fold changes >2 and p adjust < 0.05. (c) The heatmap

of the top 30 highest-ranked genes

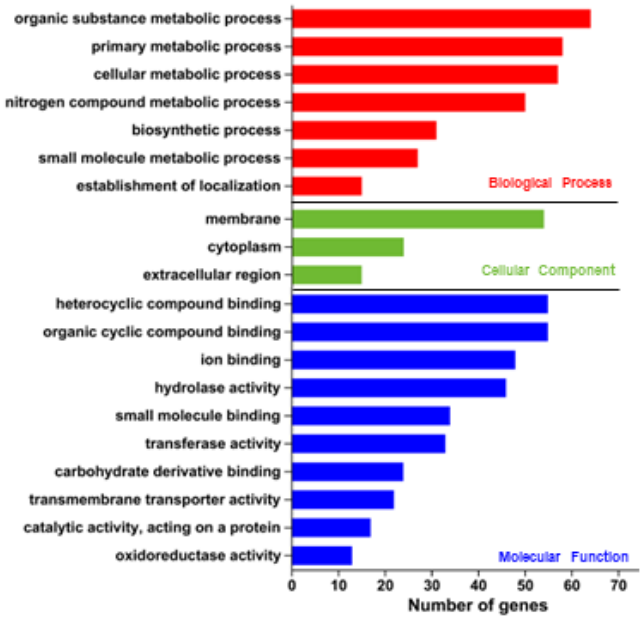

Figure 4-19 Gene ontology (GO) term classification analysis based on the DGEs.

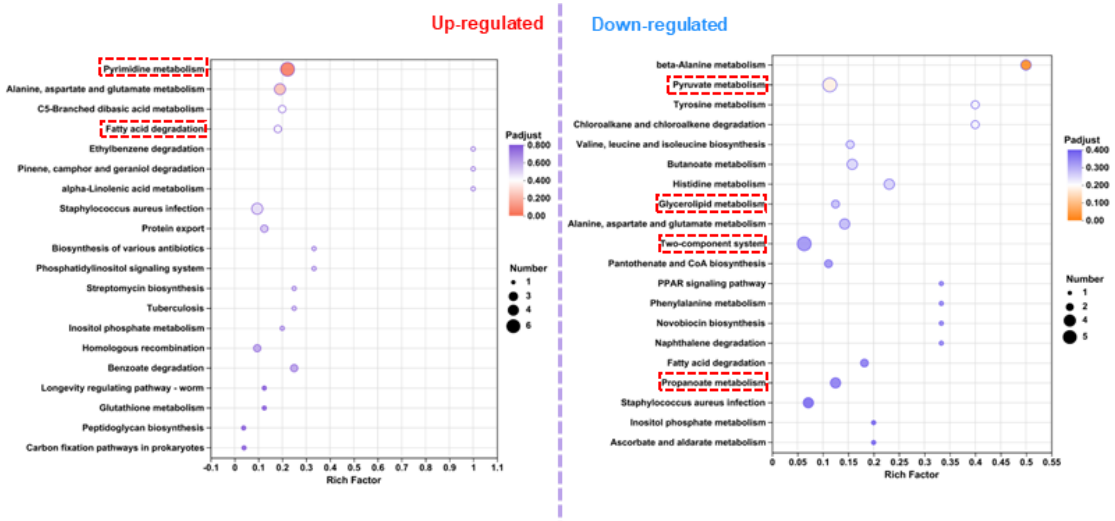

Figure 4-20 The KEGG pathways enriched by the up-regulated and down-regulated DEGs.

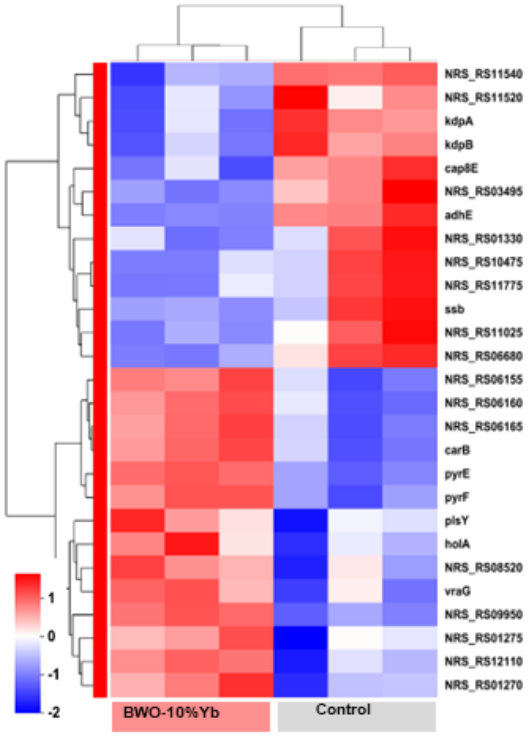

Figure 4-21 Heatmap of the DEGs involved in the ROS-related pathways.

4.7 Conclusion

In this chapter, we present Yb-dopped Bi_2WO_6 NSs as sonosensitizer with high ROS generation performance for US triggered antibacterial application. We have successfully synthesized Bi_2WO_6 NSs with different Yb doping concentrations, in which the Bi_2WO_6-10%Yb NSs significantly improved the quality of ROS generated under the trigger of US. The DFT calculation also proved the Bi_2WO_6-10%Yb NSs had a special structure that facilitated the separation of e^- and h^+ under US irradiation. Bi_2WO_6-10%Yb NSs under US irradiation present excellent in vitro inhibition rates against both gram-negative and gram-positive bacteria, indicating capable of broad spectrum of sonodynamic antibacterial. Furthermore, the mechanism of sonodynamic

antibacterial was deeply investigated at transcriptome level. It is anticipated that the Bi_2WO_6-10%Yb NSs presented in this paper would be extended to additional in vivo sonodynamic antibacterial applications domains.

Chapter 5 *In vivo* Sonodynamic Antibacterial Therapy Based on Bi_2WO_6 Nanosheets Modified Hydrogel

5.1 Introduction

The skin plays a crucial function in maintaining bodily homeostasis by shielding it from harmful substances that can lead to various diseases and significant discomfort [133]. The increasing resistance of wounds to treatment has emerged as a significant clinical obstacle, resulting in substantial global economic burden. Due to the intricate nature of wound repair, particularly in cases of severe wounds, it is necessary to develop multifunctional healing techniques that can effectively address all four stages of the wound healing process: hemostasis, inflammation, proliferation, and remodeling [134]. Virous biomaterial-based systems have been developed for wound healing through biological alteration of the above-mentioned stages [135-137]. The introduction of SDT with novel designed sonosensitizer displays desirable impacts on all stages of wound healing process [138-141]. For example, an Ag-decorated multivariate metal-organic frameworks (MOF) for enhanced SDT of bacterial infected wound healing was fabricated [138]. The silver nanoparticles (AgNPs) co-catalysts enhance the rate of electron transfer and enhance the efficiency of carrier usage. As a result, the modified MOF composition significantly enhances the production of electron-hole pairs when exposed to ultrasonic (US) stimulation, leading to a faster healing process in bacterial infected wounds.

Nevertheless, the potential toxicity of the inorganic sonosensitizer poses a significant obstacle to the advancement of its use in in vivo wound healing applications. In chapter 4, we designed BWO-10%Yb NSs with significant ROS generation performance with the irradiation of US. Although BWO-10%Yb NSs demonstrated great promise as a sonodynamic antibacterial sonosensitizer, biocapacity remains a significant challenge for in vivo applications. Recently, facile fabrication and low-cost hydrogel for antibacterial, hemostasis, and wound healing applications are widely developed [142-145]. Huang et. al developed an innovative microporous hydrogel dressing that has antibacterial and anti-inflammatory properties, aiming to enhance the healing process of wounds [146]. The synthesis of carboxymethyl agarose (CMA) included the cross-linking of agarose by hydrogen bonding, resulting in the formation of a supramolecular hydrogel. Subsequently, the hydroxy groups in the CMA molecules underwent complexation with Ag^+ ions, therefore facilitating the creation of a hydrogel. This hydrogel composite exhibits pH-responsiveness and temperature-responsiveness and releases Ag^+, an antibacterial agent, over a prolonged period of time. Furthermore, this hydrogel has exceptional compatibility with both cells and blood. Both laboratory and live animal studies show that the hydrogel has improved ability to kill germs and reduce inflammation. Additionally, it may greatly speed up the process of regenerating skin tissue and closing wounds. Remarkably, hydrogel may expedite the onset of the inflammatory process and reduce its duration compared to a typical procedure.

Therefore, we present a novel combination of inorganic sonosensitizers with hydrogel to reduce the cytotoxicity and maintain the superior ROS generation

performance in the meantime. Hence, before conducting *in vivo* sonodynamic antibacterial tests, the BWO-10%Yb NSs were incorporated with Polyvinyl alcohol (PVA) hydrogel to enhance their biocompatibility. Sonodynamic treatment was used for the healing of infected wounds by using the BWO-10%Yb NSs sonosensitizer in combination with a PVA hydrogel substrate. The cytotoxicity test demonstrates that the coalescence of BWO-10%Yb NSs and PVA hydrogel greatly enhances the ability of the sonosensitizer to destroy cells. Furthermore, the B-PVA hydrogel, as it is made, has commendable antibacterial properties when tested in a controlled laboratory environment. Subsequently, the B-PVA hydrogel was administered to the in vivo model of MRSA-infected wound healing and subjected to ultrasound treatment. The statistical analysis of the wound area revealed that the application of US irradiation resulted in a significant acceleration of the wound healing process when using the B-PVA hydrogel. Furthermore, the histological investigation and the standard blood test validated that the B-PVA hydrogel facilitated sonodynamic therapy (SDT), resulting in a significant enhancement of the wound healing process. Hence, the amalgamation of BWO-10%Yb NSs sonosensitizer with PVA hydrogel, showcasing exceptional antibacterial properties and little harm to cells, presents a very encouraging prospect for sonodynamic antibacterial treatment.

5.2 Experimental

5.2.1 Materials

Poly(vinyl alcohol) (PVA) was purchased from Aladdin. Dulbecco's Modified

Eagle Medium (DMEM) and fetal bovine serum (FBS) were brought from Gibco. Cell counting kit-8 (CCK8) was obtained from Abbkine, Inc. Paraformaldehyde (4%) was purchased from Sihe, Inc.

5.2.2 Preparation for Bi_2WO_6 Nanosheets Modified Hydrogel

Figure 5-1 illustrates the procedure for synthesizing BWO-10%Yb NSs doped PVA hydrogel, abbreviated as B-PVA hydrogel. In order to prepare the B-PVA hydrogel, the Polyvinyl alcohol was dissolved in 500 ug/mL of Bi_2WO_6 NSs solution (with a mass ratio of 1:5) and then heated to 95 ℃ for 1 hour under magnetic stirring. To guarantee the ability to produce enough ROS, the concentration of BWO-10%Yb NSs in the hydrogel is maintained at 500 μg/mL throughout the synthesis. For the purpose of blank comparison, pure PVA hydrogel was also made using DI water. After that, the as-synthesized PVA and B-PVA hydrogel was placed into a mold prior to solidification to form a 2-cm-diameter piece, which is for attaching to the back of the mice in the in vivo antibacterial test. The inset of Figure 5-1 is 2-cm-diameter piece of B-PVA hydrogel.

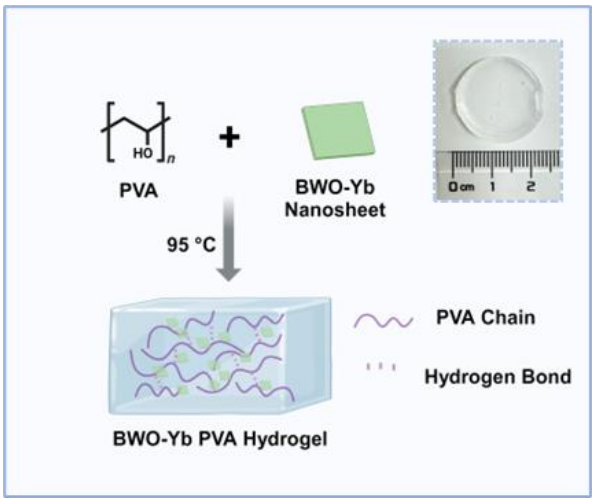

Figure 5-1 Illustration of the synthesis procedure of B-PVA hydrogel (inset is the photograph of 2 cm B-PVA hydrogel).

5.2.3 Cytotoxicity test

To compare the cytotoxicity of BWO-10%Yb NSs before and after the combination of the PVA hydrogel, the cytotoxicity test was conducted on RAW 264.7 (mouse macrophage; ATCC) cells using a CCK8 assy. For the cytotoxicity test of BWO-10%Yb NSs, the RAW cells were seeded into 96-well plates at a density of 10^5 cells per well and cultured in DMEM containing 10% FBS and 1% AA. The cells were put into the incubator with 5% CO_2 and 100% humidity at 37 ℃ overnight to adhere to the wall of a 96-well plate. Then, the culture medium was replaced by fresh culture medium containing different concentrations of BWO-10%Yb NSs (0 μg/mL, 100 μg/mL, 200 μg/mL, 500 μg/mL, each concentration set six paralleled wells). After incubating for another 24 h, the medium in each well was replaced by 100 μL of fresh medium

containing 10 μL CCK-8 and incubated for an additional 1 h. Finally, the absorbance at 450 nm was evaluated using a microplate reader.

For the cytotoxicity test of PVA and B-PVA hydrogel, the hydrogel was separately immersed in the DMEM for 24 h and 72 h to obtain the leaching liquor of PVA-24 h, PVA-72 h, B-PVA-24 h and B-PVA-72 h (each group set six paralleled wells). The RAW cells were seeded into 96-well plates and 100 μL of the DMEM leaching liquor with 10% FBS and 1% AA were added into each well (each sample set six paralleled wells). The cells were put into the incubator with 5% CO_2 and 100% humidity at 37 ℃ overnight. Then 10 μL of CCK-8 was added to each well and cultured for another 1 h. Finally, the absorbance at 450 nm was evaluated using a microplate reader.

5.2.4 Preparing the SEM Sample of PVA and B-PVA Hydrogel

PVA and B-PVA hydrogel was freeze dried using a freeze dryer overnight and smashed in liquid nitrogen. The samples were observed on a conducting resin using Tescan CLARA Field-emission SEM.

5.2.5 In Vitro Antibacterial Test of B-PVA Hydrogel

The antibacterial activity of Bi_2WO_6-10%Yb NSs and B-PVA hydrogel against MRSA was evaluated using a plate counting method. First, 50 μL of bacteria suspension (10^6 CFU/ mL) in PBS was added to 50 μL of PBS, Bi_2WO_6-10%Yb NSs (1 mg mL^{-1}), and a piece of B-PVA hydrogel, respectively. Then the mixture was treated with or without US (1.0 MHz, 1.5 W/cm^2, 50% duty cycle) for 5 min. Bacteria treated with

PBS were set as the control group, termed as Control US(-), and Control US(+)), the bacteria treated with Bi_2WO_6-10%Yb NSs were termed as Bi_2WO_6-10%Yb US(-) and Bi_2WO_6-10%Yb US(+), while the bacteria treated with B-PVA hydrogel were termed as B-PVA hydrogel US(-) and B-PVA hydrogel US(+), respectively (each group set three parallel samples). After different treatments, the bacteria suspensions were gradient diluted with PBS (1:10, 1:100, 1:1000, 1:10000). Then 10 μL of each diluent was dropped on an LB agar plate and cultured at 37 °C for 24 h.

5.2.6 In vivo Wound Infection and Healing Test

The animal test was performed under approval of Animal Subjects Ethic Sub-committee of the Hong Kong Polytechnic University (Ref no. ARSA-24141-CRF-AP). All the animal tests involving bacteria were performed in an Animal Biosafety Level 2 (ABSL-2) laboratory.

30 Male Balb/c mice (6 weeks old, ~20 g in weight) were randomly divided into five groups (Control US(-), Control US(+), PVA US(+), B-PVA US(-), B-PVA US(+), n=6). To establish a MRSA infected wound healing model, a 6 mm diameter incision was created on the back of the mice and a suspension of MRSA (1×10^8 CFU mL^{-1}, 25 μL) was applied to the wound area (Day 0). Then the wound area was tightly wrapped with a bandage (3M) for 24 hours to ensure infection and the bandage was discarded before the treatments. The infected mice in Control US(+), PVA US(+), and B-PVA US(+) groups were treated with US (1.5 W/cm^2, 50% duty cycle, 1 MHz) for 5 min (Day 1). Then the weight of each mouse was recorded, and the wound area was

photographic recorded every two days (Day 2,4,6,8,10). After 10 days of feeding, all the mice were sacrificed, and the wound area was dissected and fixed in paraformaldehyde (4%) for H&E, Masson and Gram staining analysis (Day 10). The major organs of the mice were collected separately and fixed in paraformaldehyde (4%) for H&E staining analysis. In addition, the blood of the mice in each group (n = 3) was taken for blood routine tests (WBC, NEU, RBC, MCV, PLT, and MPV) through automatic blood cell analyzers (URIT-5160Vet 5-Part-Diff Hematology Analyzer).

5.2.7 Histological Analysis

For histopathological analysis of the healed wound area, the wound tissues of each mouse were dissected and fixed in 4% paraformaldehyde solution for 48 h. Subsequently, the tissues of the wound were subjected to dehydration and then embedded in paraffin to get a continuous cross section. The cross sections were stained with hematoxylin and eosin (H&E), Masson, and Gram to analyze the inflammatory infiltration, collagen density and residual bacteria in the wound area. Furthermore, the H&E staining was also employed to assess the histological state of major organs (heart, liver, spleen, lung, kidney). The slices after staining were observed using a Nikon Inverted Fluorescent Microscope.

5.3 Properties of Bi_2WO_6 Nanosheets Modified Hydrogel

To evaluate the improvement in biocapacity after the combination of BWO-10%Yb NSs and PVA hydrogel, the in vitro cytotoxicity of BWO-10%Yb NSs, PVA and B-PVA

hydrogel was assessed on RAW cells using CCK-8 assay. Given that the PVA hydrogel has the potential to absorb water from the cell culture medium, the hydrogel was immersed in the cell culture medium for 24 h and 72 h beforehand, and the leaching solution of the hydrogel was used to conduct the cell viability test. The result of the cell viability of BWO-10%Yb NSs with increasing concentration and leaching solution of the hydrogel are displayed in Figure 5-2. The cell viability of RAW cells incubated with BWO-10%Yb NSs decreased dramatically as the concentration of BWO-10%Yb NSs increased, as compared to the control groups (Figure 5-2, left). When RAW cells were exposed to a concentration of 500 μg/mL BWO-10%Yb NSs, the cell viability dropped to 25%, indicating that BWO-10%Yb NSs exhibited considerable cytotoxicity. In comparison, after 24 hours of incubation with the PVA and B-PVA hydrogel leaching solution, the cell viability did not exhibit any significant change compared to the blank group (Figure 5-2, right). Therefore, the as-synthesized B-PVA hydrogel effectively enhanced the biocompatibility of BWO-10%Yb NSs and provided the possibility for in vivo sonodynamic antibacterial applications.

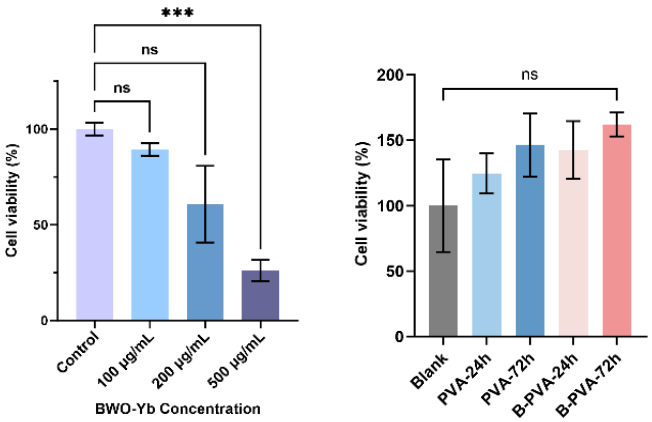

Figure 5-2 Cell viability of BWO-10%Yb NSs (left), and PVA and B-PVA hydrogel (right).

To ensure a satisfactory mixture of BWO-10%Yb NSs in PVA hydrogel, the structure of B-PVA hydrogel was further evaluated with SEM. The hydrogel was freeze-dried and fractured in liquid nitrogen to investigate the cross-section of B-PVA hydrogel. The SEM images in Figure 5-3 illustrate the porous structure in the internal composition of B-PVA hydrogels from a cross-sectional view. In addition, the EDX mapping further reveals the effective integration of BWO-10%Yb NSs into the B-PVA hydrogel.

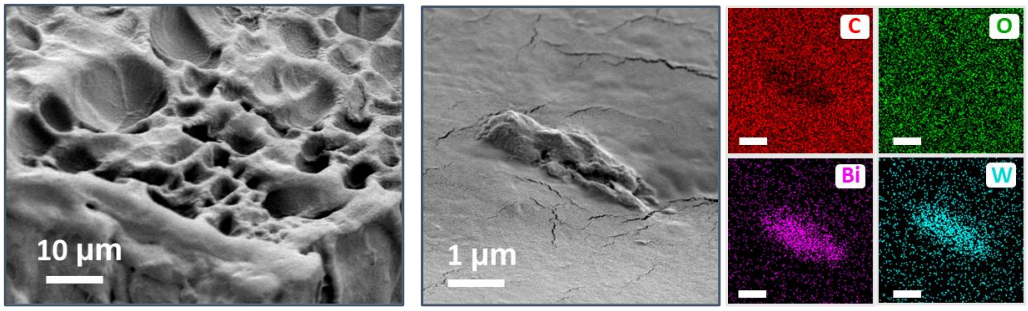

Figure 5-3 SEM and the EDX mapping image of B-PVA hydrogel.

5.4 B-PVA Hydrogel Sonodynamic Antibacterial Performance

The sonodynamic antibacterial capability of B-PVA hydrogel is also evaluated using a plate counting analysis. The suspensions of MRSA after different treatments (Control US(-), Control US(+), BWO-10%Yb US(-), BWO-10%Yb US(+), B-PVA US(-), B-PVA US(+)) were continuously diluted from an initial concentration of 10^6 CFU/mL to a final concentration of 10^2 CFU/mL. Subsequently, 10 μL of the diluent was dropped on an LB agar plate and cultured for 20h. As shown in Figure 5-4(a), there

is no significant difference between the groups treated without US irradiation and the US-only group. A 100% reduction in MRSA was seen after being treated with BWO-10%Yb NSs and US (BWO-10%Yb NSs US (+)), whereas the concentration of MRSA treated by B-PVA and US (B-PVA US (+)) is two orders of magnitude lower, as shown in Figure 5-4(b). Therefore, although the sonodynamic antibacterial capability of B-PVA hydrogel is inferior to bare BWO-10%Yb NSs, it still demonstrates considerable potential for in vivo sonodynamic antibacterial applications.

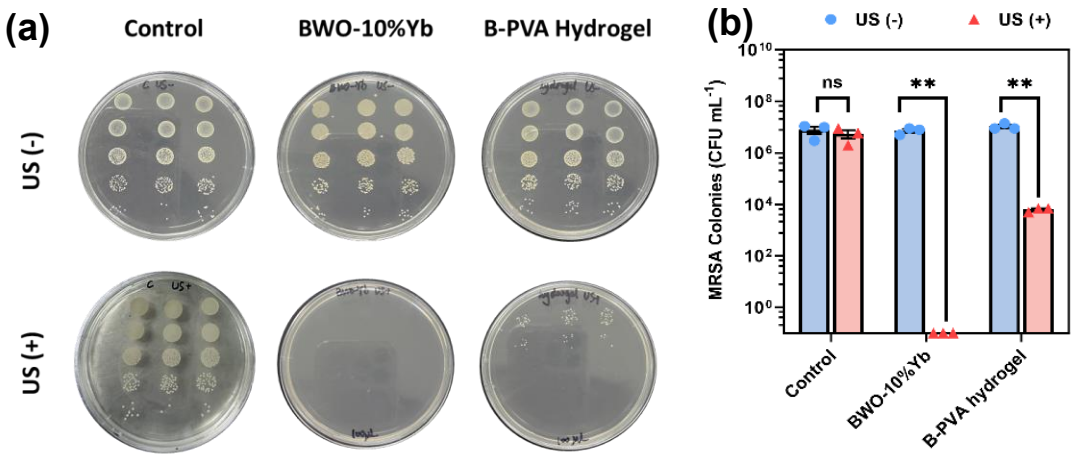

Figure 5-4 (a) Photograph of MRSA colonies after different treatments with continuous dilution ratio coating on the LB agar plate. (b) Corresponding MRSA-killing abilities of BWO-10%Yb NSs and B-PVA hydrogel. The error bars indicate mean ± SEM. The statistical analysis was performed using one-way ANOVA with Tukey's multiple-comparisons test: *$p < 0.05$, **$p < 0.01$, ***$p < 0.001$, and ****$p < 0.0001$; ns: not significant ($p > 0.05$).

5.5 In vivo Sonodynamic Therapy Based on Bi_2WO_6 Nanosheets Modified Hydrogel

Building upon the impressive antibacterial efficacy of the in vitro BWO-10%Yb NSs-mediated SDT, the antibacterial impact *in vivo* was assessed. A wound infection model was created on the back of the 6-week-old BALB/C mouse by making a 6 mm diameter incision and applying a suspension of MRSA (1×10^8 CFU mL^{-1}, 25 μL) to the wound area. The wound area was then tightly wrapped with a bandage for 24 hours to ensure infection before the treatments. Afterward, the mice were randomly separated into 5 groups (n = 6) for different treatments, i.e. Control US (-), Control US (+), PVA US (+), B-PVA US (-), and B-PVA US (+). Given the viscosity and stretchability of PVA hydrogel, it can directly adhere to the back of the mice in the hydrogel treatment group to cover the wound region without any binding agent. The US irradiation power is 1.5 W/cm^2, 50% duty cycle, 1 MHz and the treatment duration is 5 min. Schematic illustration of MRSA-infected wound healing model and the treatment process is depicted in Figure 5-5.

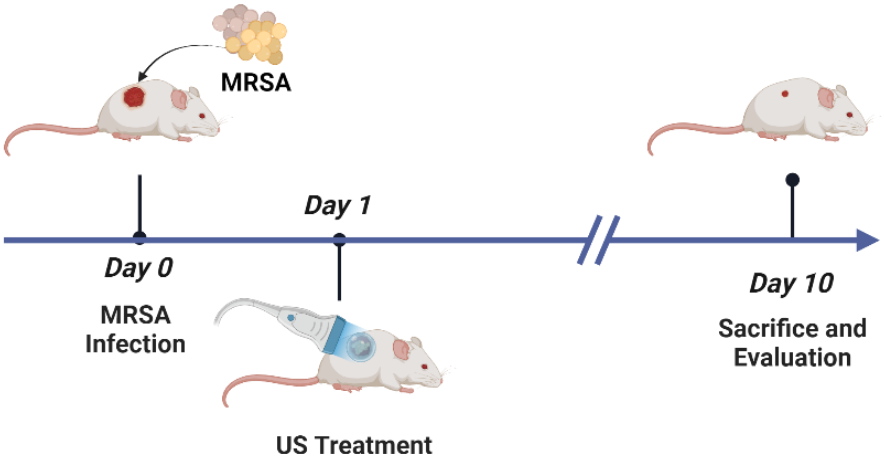

Figure 5-5 Schematic illustration of MRSA-infected wound healing model and the treatment process.

The body weight and wound closure of the mice in each group were monitored every two days after the therapy to evaluate the wound healing progress. As shown in Figure 5-6(a), the wound healing rates were comparable across the control (C US(-)), US only (C US (+)), and PVA US (+) groups. The wound sites of the mice in these three groups exhibited continuous festering from Day 1 to Day 10, indicating a severe infection of MRSA and inflammation in the wound area. The wound treated with B-PVA hydrogel but not exposed to the US showed a slightly accelerated wound-healing process. Nevertheless, the mice that received treatment with B-PVA hydrogel along with US irradiation demonstrated prevention of bacterial infection and a notable speed-up in scabbing. The relative wound area (%) was calculated by the following equation according to the photograph using ImageJ.

Relative Wound Area (%) = (Area (Day 1) − Area (Day 10)) / (Area (Day 1)) ×

100%.

According to the statistical analysis of the wound area measurements, the wound area of the mice in B-PVA US (+) group on day 10 decreased to only 25% of the initially infected wound area on Day 1 (Figure 5-6(b)). In contrast, the mice in other groups demonstrated no significant difference compared to the C US(-) group. Noticeably, the wound area of the mice in the C US(+) group was more severe than the control group throughout the healing process, which may be associated with the mechanical damage caused by US without the protection of the hydrogel. The body weight of the mice is also consistent with the wound-healing process. Figure 5-6(c) reveals that the body weight of the mice in all groups showed a declining tendency in the early infection stage (Day 0-Day 2) and a constant increase from Day 2 to Day 10, except the group exposed to US only. The US only group showed an apparent rise until Day 8, which might be attributed to severe bacterial infection and inflammation.

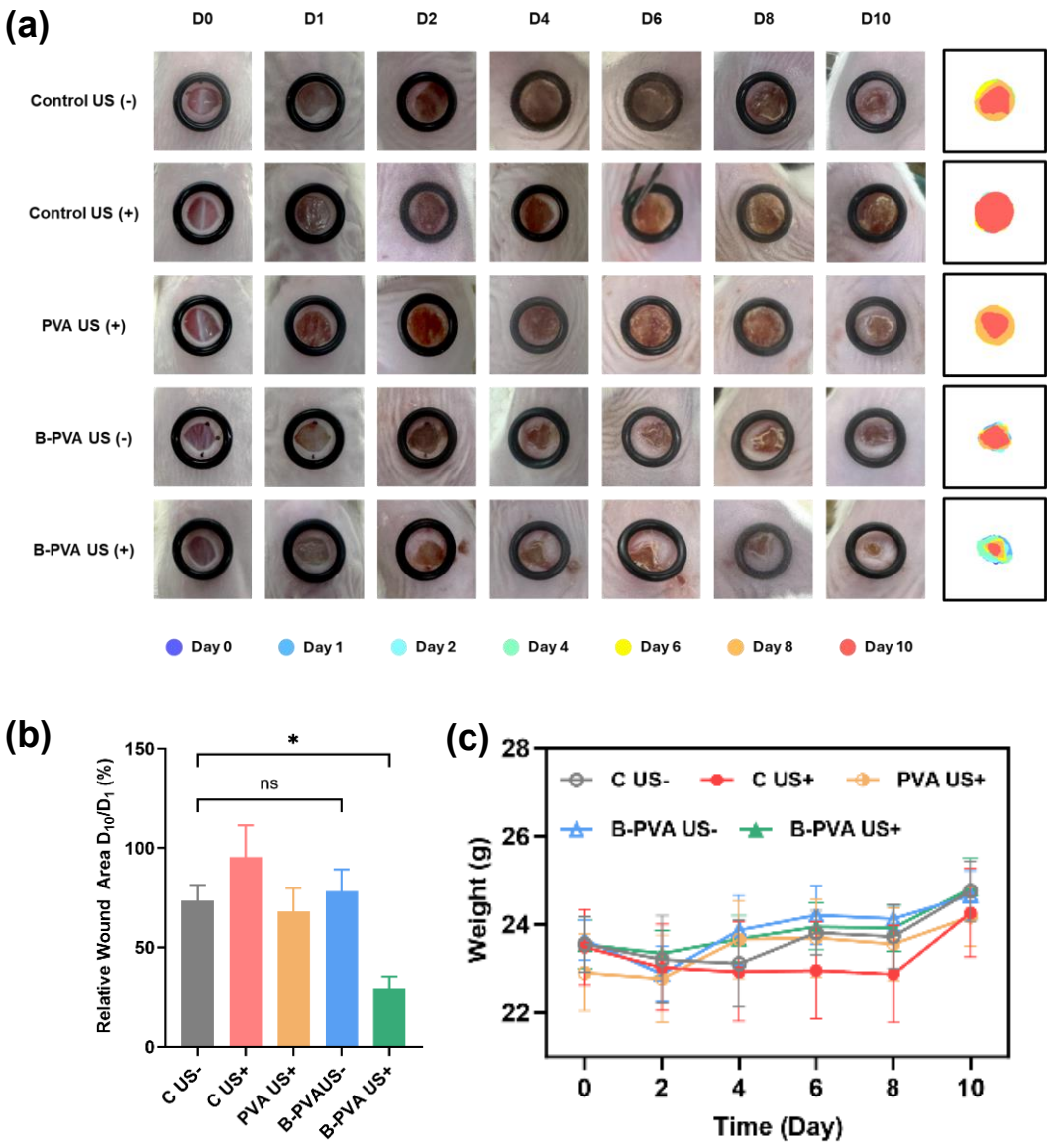

Figure 5-6 (a) Photographs of the infected wound area from Day 0 to Day 10 in each group. The last column is the skeleton map depicting the changes in the wound area. (b) Relative wound area (Day10/Day1) of the different groups. (c) Body weight changes of mice in different treatment groups.

The mice were sacrificed on the 10th day after the therapy, then the blood sample

of the mice in each group was collected, and the wound region and the major organs were also dissected for further evaluation.

Due to the fact that the bacterial infection always triggers an inflammatory response in the host, the inflammation in the infection models was assessed using standard blood examination, in which white blood cells and neutrophils are often used inflammation indicators to screen for the severity of bacterial infection. In addition, the red blood cells and the blood platelet also act as the indicators for wound healing process. The result of standard blood examination of white blood cells (WBC), neutrophils (NEU), red blood cells (RBC), mean corpuscular volume (MCV), platelet count (PLT), mean platelet volume (MPV) are displayed in Figure 5-7 (the normal range is indicated by dashed rectangular lines). Compared with the B-PVA + US group, the numbers of WBCs and neutrophils in the Control US(-), C US(+), and B-PVA US(-) groups were much higher, suggesting that the inflammatory response caused by MRSA infection was obvious. While the WBCs and neutrophils in the PVA US(+) group is lower than the standard range. The red blood cells and the blood platelet count of the mice in each group are almost equal. As for the mean corpuscular volume (MCV) and mean platelet volume (MPV), the result in other four groups is much higher than that of the B-PVA US(+) group, indicating the mouse in other groups still have blood clotting process.

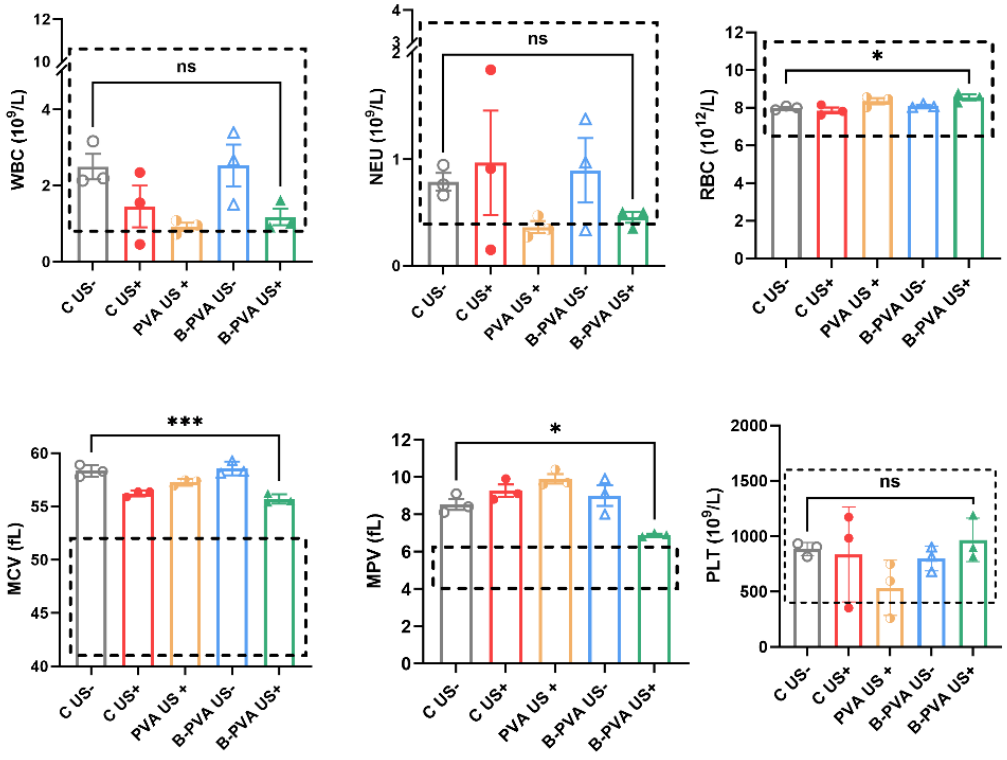

Figure 5-7 The result of WBC, NEU, RBC, MCV, PLT, and MPV in the blood of MRSA-infected mice after 10 days of treatments.

The dermal tissues around the wound area were dissected on Day 10 after the sacrifice for Histological. The H&E staining images of the mice in each group with different magnification views are displayed in Figure 5-8. Compared with the B-PVA US(+) group, the dermal tissues in other four groups were more vascular dilatation, congestion, and bleeding with more inflammatory cell infiltration (black arrows). While the B-PVA US(+) group showed no subcutaneous tissue defect and a reduced level of inflammatory cell infiltration.

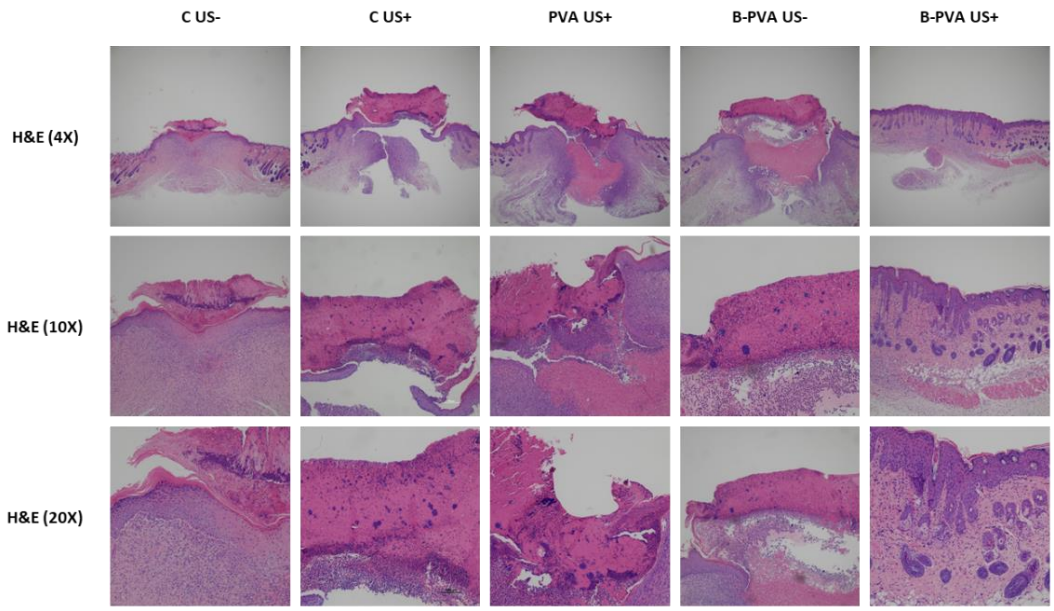

Figure 5-8 H&E staining images of the infected wound area after 10 days of treatment.

The major organs, i.e. heart, liver, spleen, lung, kidney, of the mice in each group were also collected and weighted to evaluate the impact of the US irradiation and bacterial infection. The H&E staining images and the weight of the organ are shown in Figure 5-9 and Figure 5-10, which demonstrate that the bacterial infection had no influence on the organ weights and histological structure of the major organs of mice throughout the wound healing duration.

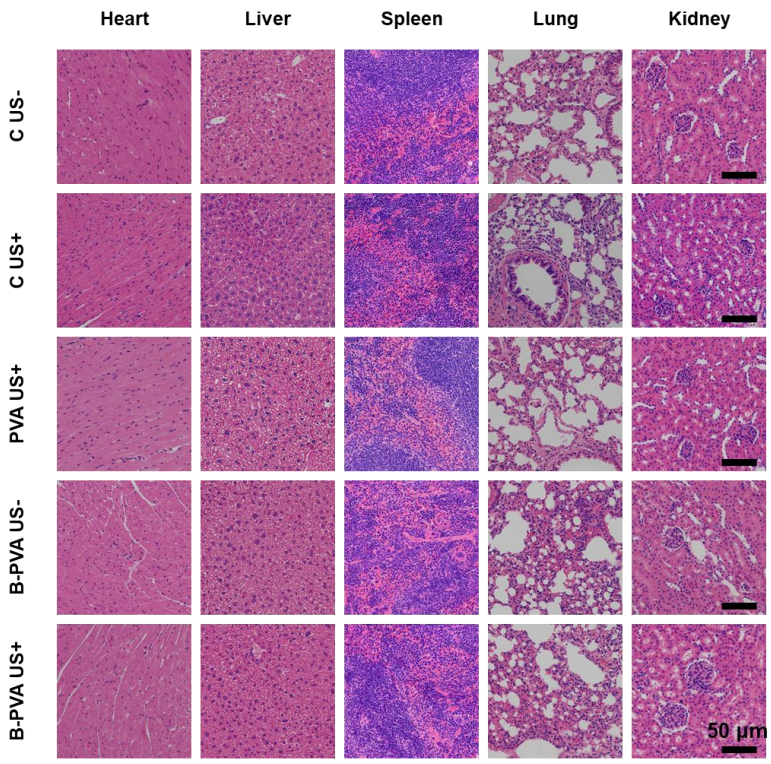

Figure 5-9 H&E staining images of the major organs of the mice in each group.

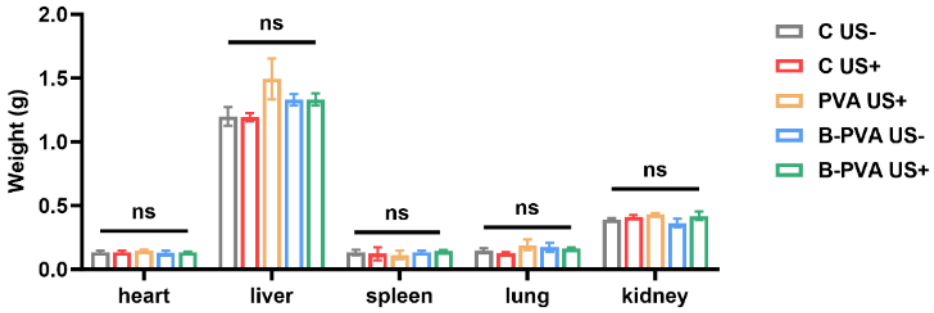

Figure 5-10 Organ weight of the mice in each group.

The Masson trichrome staining was conducted to assess the collagen accumulation at the wound region. Figure 5-11 depicts Masson staining images of the wound region.

All four control groups had necrotic scab tissues, and the epidermis of the wound region did not completely regenerate, with the regenerated collagen fibers poorly formed and loosely organized. In comparison to the control groups, the B-PVA US(+) group exhibited a dense arrangement of new collagen fibers, indicating the satisfactory healing of the treated wound region.

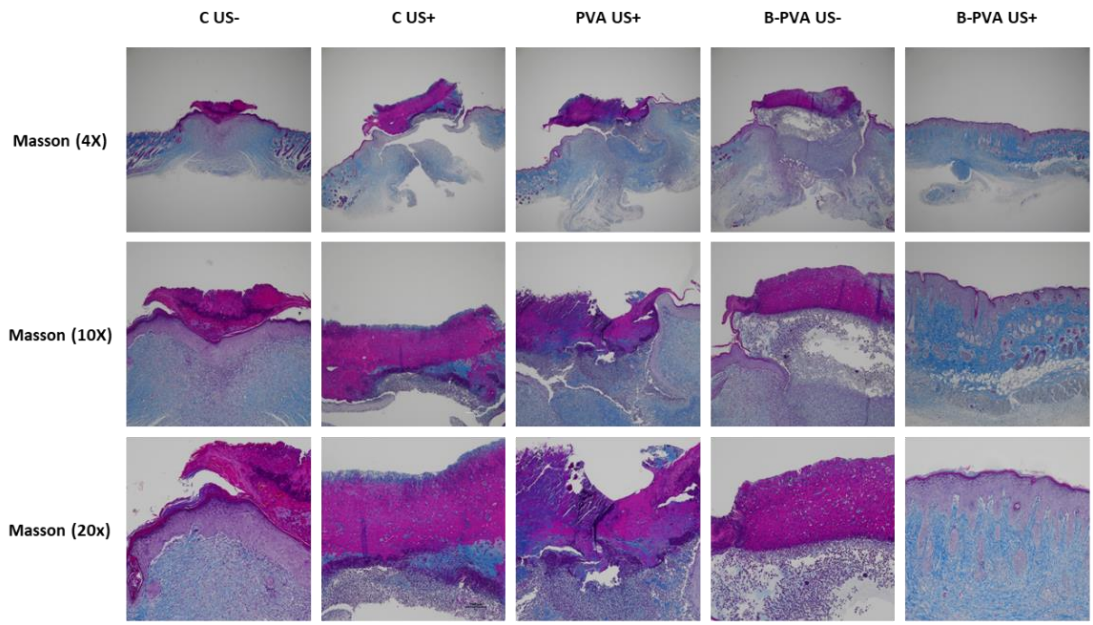

Figure 5-11 Masson staining images of the infected wound area after 10 days of treatment.

In addition, Gram staining was employed to further evaluate the remaining bacteria in the wound region on Day 10, as shown in Figure 5-12. The mice in the other treatment groups had a significant number of dark purple spots on their Gram stain section of skin (red circles in Figure 5-12), indicating that remnants of MRSA still existed in the wound area until Day 10. Conversely, the group treated with B-PVA

hydrogel and US had negligible spots. These findings provided conclusive evidence that SDT treatment based on B-PVA hydrogel may kill all bacteria inside the wound and speed up the healing process in an MRSA-infected wound model.

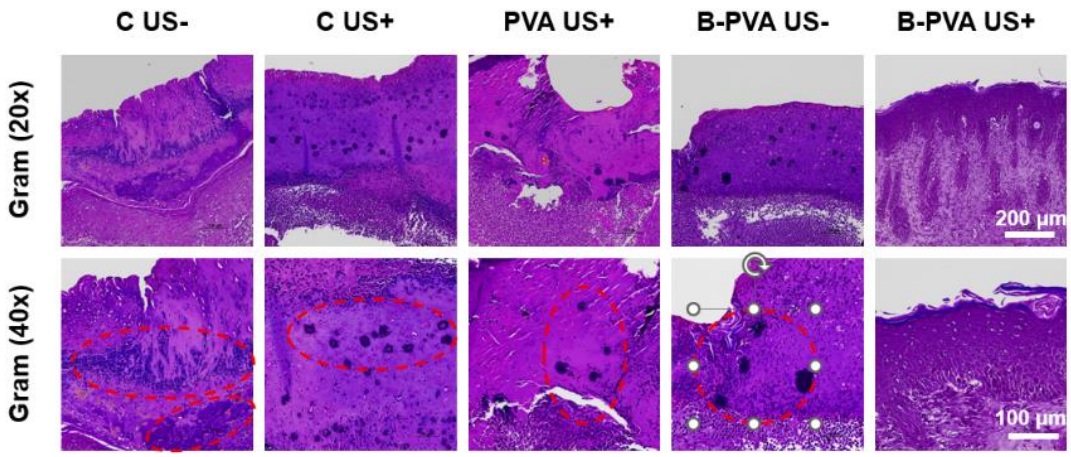

Figure 5-12 Gram staining images of the infected wound area after 10 days of treatment.

5.6 Conclusion

In this work, we successfully synthesized a novel sonosensitizer combined with PVA hydrogel platform for antibacterial infected wound healing via sonodynamic therapy. The cytotoxicity test reveals that the combination of BWO-10%Yb NSs and PVA hydrogel significantly improved the biocapacity of the sonosensitizer. In addition, the as-synthesized B-PVA hydrogel also possesses good antibacterial performance *in vitro*. Then the B-PVA hydrogel was applied to the *in vivo* MRSA-infected wound healing model and treated with US. The statistical analysis of the wound area demonstrated that under the US irradiation, the B-PVA hydrogel significantly accelerated the wound healing process. Moreover, the histological examination and the

standard blood test confirmed that the B-PVA hydrogel mediated SDT leading to a considerable acceleration of the wound healing process. Therefore, the combination of BWO-10%Yb NSs sonosensitizer with PVA hydrogel, which exhibits remarkable ability of antibacterial and low cytotoxicity, holds great promise for sonodynamic antibacterial therapy.

Chapter 6 Conclusions and Outlook

6.1 Conclusions

Public healthcare systems face a significant problem when harmful organisms, such as viruses and bacteria, experience outbreaks. To stop the spread of infectious diseases, early diagnosis and treatment are crucial. Since the fluorophore's luminous intensity changes with the approach or separation of the energy pairs, FRET has been widely employed for biosensing in biodetection assays. Consequently, this thesis develops a FRET biodetection assay for viral detection using upconversion nanoparticles (UCNPs) and gold nanoparticles. In terms of pathogen treatment, sonodynamic therapy (SDT) offers great promise for avoiding infections caused by bacteria that are resistant to several drugs. This is because SDT is non-invasive and does not rely on antibiotics, two factors that contribute to the issue of bacterial resistance. Therefore, Bi2WO6 nanosheets are used as a sonosensitizer for sonodynamic treatment, and an antibacterial application is carried out in both vitro and in vivo.

In the first part of the thesis, an ultrasensitive plasmon-enhanced fluorescence resonance energy transfer (FRET) biosensor based on core-shell upconversion nanoparticle (csUCNP) and gold nanoparticle (AuNP) for accurate detection of SARS-CoV-2 viral RNA is presented. In this biodetection assay, the Tm^{3+}/Er^{3+} co-doped csUCNP $NaGdF_4$:Yb/Tm@$NaYF_4$:Yb/Er acts as an energy donor and AuNP serves as an energy acceptor. An AuNP surface plasmon effect occurred simultaneously due to

the upconversion emission of Tm^{3+} and the core-shell structure's design. The FRET efficiency between Er^{3+} and AuNP was greatly improved by the localized surface plasmon resonance (LSPR) that resulted from the collective oscillations of free electrons. The incorporation of FRET and surface plasmon into a single biodetection assay considerably enhanced the biosensor's sensitivity, as shown by the as-prepared biosensor achieving a limit of detection (LOD) as low as 750 aM. Furthermore, clinical sample extracts are also used to verify the biosensor's efficacy. Hence, our novel plasmon-enhanced FRET biosensor comprised of csUCNP co-doped with Tm^{3+} and Er^{3+} should lead to more precise and speedier biodetection.

Bi_2WO_6 nanosheets (BWO NSs) were successfully synthesized through the hydrothermal method as the sonosensitizer, and varying concentrations of Ytterbium ions were doped (BWO-x%Yb, x=1,2,5,10,20) to improve the sonodynamic activity. The Yb ions were verified to occupy the position of Bi by both calculation and XRD characterization. The reactive oxygen species (ROS) produced by BWO-x%Yb under ultrasound (US) irradiation were examined. It was shown that at a concentration of 10% Yb, the nanosheets generated the highest amount of ROS. ROS has the ability to cause oxidation of lipids in the bacterial cell membrane, resulting in the deterioration of membrane integrity. This can result in the release of intracellular substances and ultimately lead to cellular demise. In vitro experiments have verified that the BWO-10%Yb NSs are capable of eliminating both Methicillin-resistant *Staphylococcus aureus* (MRSA) and Escherichia coli (E. coli) through ROS generation. For a better grasp of how BWO-10%Yb NSs exert their sonodynamic antibacterial effects, RNA

sequencing transcriptome study was performed using MRSA.

To enhance biocapacity for further in vivo antibacterial uses, the BWO-10%Yb NSs are mixed with polyvinyl alcohol (PVA) hydrogel in the third section of the thesis. The BWO-Yb-PVA hydrogel that was produced was also very effective in eliminating microorganisms. The BWO-Yb-PVA hydrogel sped up the healing of MRSA-infected lesions in the in vivo test. Sonosensitizer is a new kind of antibiotic that we developed to aid in wound healing and sonodynamic bacterial eradication.

6.2 Suggestions for Future Work

Because of its simplicity, affordability, and speed, this FRET biosensor using UCNPs in chapter 3 has the potential to be transformed into a point-of-care biosensor for detecting SARS-CoV-2. The biosensor may be enhanced with additional biomarkers that are specifically tailored to recognize certain diseases. The occurrence of this binding event may be converted into an electrochemical signal that is detectable. This biosensor, based on UCNP (upconversion nanoparticle), has a high potential for detecting SARS-CoV-2 with great sensitivity. Its use may significantly reduce the amount of work required by medical professionals.

In chapter 4, the modification of BWO NSs by doping Yb significantly increases the amount of ROS generated under the trigger of US. Based on this results, further modification could be introduced to enhance the ROS generation performance.

In addition, the sonosensitizer introduced in chapter 4 and the combination with hydrogel in chapter 5 provide further potential for biocompatible inorganic

sonosensitizer. The PVA hydrogel could be altered by injectable hydrogel and combined with the inorganic sonosensitizer for the sonodynamic treatment of internal infections, such as osteomyelitis, lung infections, or even brain infections.

References

[1] K. Jain; J. Ahmad, *Nanotheranostics for treatment and diagnosis of infectious diseases*. Academic Press: **2022**.

[2] E. A. Masters; B. F. Ricciardi; K. L. d. M. Bentley; T. F. Moriarty; E. M. Schwarz; G. Muthukrishnan, *Nat. Rev. Microbiol.* **2022,** *20* (7), 385-400. DOI 10.1038/s41579-022-00686-0.

[3] S. E. Randolph; D. J. Rogers, *Nat. Rev. Microbiol.* **2010,** *8* (5), 361-371. DOI 10.1038/nrmicro2336.

[4] C. J. Megli; C. B. Coyne, *Nat. Rev. Microbiol.* **2022,** *20* (2), 67-82. DOI 10.1038/s41579-021-00610-y.

[5] N. I. Nii-Trebi, *Biomed Res. Int.* **2017,** *2017* (1), 5245021. DOI https://doi.org/10.1155/2017/5245021.

[6] H. Heesterbeek; R. M. Anderson; V. Andreasen; S. Bansal; D. De Angelis; C. Dye; K. T. D. Eames; W. J. Edmunds; S. D. W. Frost; S. Funk; T. D. Hollingsworth; T. House; V. Isham; P. Klepac; J. Lessler; J. O. Lloyd-Smith; C. J. E. Metcalf; D. Mollison; L. Pellis; J. R. C. Pulliam; M. G. Roberts; C. Viboud; I. N. I. I. Collaboration, *Science* **2015,** *347* (6227), aaa4339. DOI doi:10.1126/science.aaa4339.

[7] WHO COVID-19 dashboard. https://data.who.int/dashboards/covid19/deaths?n=c. (accessed 11 Aug 2024).

[8] M. M. Lamers; B. L. Haagmans, *Nat. Rev. Microbiol.* **2022,** *20* (5), 270-284. DOI 10.1038/s41579-022-00713-0.

[9] K. G. Andersen; A. Rambaut; W. I. Lipkin; E. C. Holmes; R. F. Garry, *Nat. Med.* **2020,** *26* (4), 450-452. DOI 10.1038/s41591-020-0820-9.

[10] P. Zhou; X.-L. Yang; X.-G. Wang; B. Hu; L. Zhang; W. Zhang; H.-R. Si; Y. Zhu; B. Li; C.-L. Huang; H.-D. Chen; J. Chen; Y. Luo; H. Guo; R.-D. Jiang; M.-Q. Liu; Y. Chen; X.-R. Shen; X. Wang; X.-S. Zheng; K. Zhao; Q.-J. Chen; F. Deng; L.-L. Liu; B. Yan; F.-X. Zhan; Y.-Y. Wang; G.-F. Xiao; Z.-L. Shi, *Nature* **2020,** *579* (7798), 270-273. DOI 10.1038/s41586-020-2012-7.

[11] J. van Beek; M. de Graaf; H. Al-Hello; D. J. Allen; K. Ambert-Balay; N. Botteldoorn; M. Brytting; J. Buesa; M. Cabrerizo; M. Chan; F. Cloak; I. Di Bartolo; S. Guix; J. Hewitt; N. Iritani; M. Jin; R. Johne; I. Lederer; J. Mans; V. Martella; L. Maunula; G. McAllister; S. Niendorf; H. G. Niesters; A. T. Podkolzin; M. Poljsak-Prijatelj; L. D. Rasmussen; G. Reuter; G. Tuite; A. Kroneman; H. Vennema; M. P. G. Koopmans, *Lancet Infect. Dis.* **2018,** *18* (5), 545-553. DOI 10.1016/S1473-3099(18)30059-8.

[12] S. T. Jacob; I. Crozier; W. A. Fischer; A. Hewlett; C. S. Kraft; M.-A. d. L. Vega; M. J. Soka; V. Wahl; A. Griffiths; L. Bollinger; J. H. Kuhn, *Nat. Rev. Dis. Primers* **2020,** *6* (1), 13. DOI 10.1038/s41572-020-0147-3.

[13] S. Rewar; D. Mirdha, *Annals of Global Health* **2014,** *80* (6), 444-451. DOI https://doi.org/10.1016/j.aogh.2015.02.005.

[14] L. A. Denny; S. Franceschi; S. de Sanjosé; I. Heard; A. B. Moscicki; J. Palefsky, *Vaccine* **2012,** *30*, F168-F174. DOI https://doi.org/10.1016/j.vaccine.2012.06.045.

[15] Z. A. Memish; S. Perlman; M. D. Van Kerkhove; A. Zumla, *The Lancet* **2020,** *395*

(10229), 1063-1077. DOI 10.1016/S0140-6736(19)33221-0.

[16]R. E. Baker; A. S. Mahmud; I. F. Miller; M. Rajeev; F. Rasambainarivo; B. L. Rice; S. Takahashi; A. J. Tatem; C. E. Wagner; L.-F. Wang; A. Wesolowski; C. J. E. Metcalf, *Nat. Rev. Microbiol.* **2022,** *20* (4), 193-205. DOI 10.1038/s41579-021-00639-z.

[17]L. Ferrucci; E. Fabbri, *Nat. Rev. Cardiol.* **2018,** *15* (9), 505-522. DOI 10.1038/s41569-018-0064-2.

[18]M. G. Lazzaroni; S. Piantoni; S. Masneri; E. Garrafa; G. Martini; A. Tincani; L. Andreoli; F. Franceschini, *Blood Reviews* **2021,** *46*, 100745. DOI https://doi.org/10.1016/j.blre.2020.100745.

[19]S. Cobey, *Science* **2020,** *368* (6492), 713-714. DOI doi:10.1126/science.abb5659.

[20]K. S. Ikuta; L. R. Swetschinski; G. Robles Aguilar; F. Sharara; T. Mestrovic; A. P. Gray; N. Davis Weaver; E. E. Wool; C. Han; A. Gershberg Hayoon, *The Lancet* **2022,** *400* (10369), 2221-2248. DOI 10.1016/S0140-6736(22)02185-7.

[21]S. L. Percival; C. Emanuel; K. F. Cutting; D. W. Williams, *International Wound Journal* **2012,** *9* (1), 14-32. DOI https://doi.org/10.1111/j.1742-481X.2011.00836.x.

[22]P. Baral; B. D. Umans; L. Li; A. Wallrapp; M. Bist; T. Kirschbaum; Y. Wei; Y. Zhou; V. K. Kuchroo; P. R. Burkett; B. G. Yipp; S. D. Liberles; I. M. Chiu, *Nat. Med.* **2018,** *24* (4), 417-426. DOI 10.1038/nm.4501.

[23]L. Le Guennec; M. Coureuil; X. Nassif; S. Bourdoulous, *Cell Microbiol* **2020,** *22* (1), e13132. DOI https://doi.org/10.1111/cmi.13132.

[24]R. Nau; F. Sörgel; H. Eiffert, *Clin. Microbiol Rev.* **2010,** *23* (4), 858-883. DOI doi:10.1128/cmr.00007-10.

[25] K. Lalchhandama, *Wiki Journal of Medicine* **2021,** *8* (1), 1-16.

[26] E. S. R. Darley; A. P. MacGowan, *J. Antimicrob. Chemother.* **2004,** *53* (6), 928-935. DOI 10.1093/jac/dkh191.

[27] R. Wilson; S. Sethi; A. Anzueto; M. Miravitlles, *J. Infect.* **2013,** *67* (6), 497-515. DOI https://doi.org/10.1016/j.jinf.2013.08.010.

[28] S. Basak; P. Singh; M. Rajurkar, *J. Pathog.* **2016,** *2016* (1), 4065603. DOI https://doi.org/10.1155/2016/4065603.

[29] H. Nikaido, *Annu. Rev. Biochem.* **2009,** *78* (Volume 78, 2009), 119-146. DOI https://doi.org/10.1146/annurev.biochem.78.082907.145923.

[30] WHO bacterial priority pathogens list, 2024. https://www.who.int/publications/i/item/9789240093461. (accessed 13 Aug 2024).

[31] Ten threats to global health in 2019. https://www.who.int/news-room/spotlight/ten-threats-to-global-health-in-2019. (accessed 13 Aug 2024).

[32] N. Ravi; D. L. Cortade; E. Ng; S. X. Wang, *Biosens. Bioelectron.* **2020,** *165*, 112454. DOI https://doi.org/10.1016/j.bios.2020.112454.

[33] D. Wen; S. Yang; G. Li; Q. Xuan; W. Guo; W. Wu, *J. Mol. Diagn.* **2021,** *23* (6), 665-670. DOI https://doi.org/10.1016/j.jmoldx.2021.02.010.

[34] T. Nolan; R. E. Hands; S. A. Bustin, *Nat. Protoc.* **2006,** *1* (3), 1559-1582. DOI 10.1038/nprot.2006.236.

[35] B. Ince; M. K. Sezgintürk, *TrAC, Trends Anal. Chem.* **2022,** *157*, 116725. DOI https://doi.org/10.1016/j.trac.2022.116725.

[36] H. Sohrabi; M. R. Majidi; M. Fakhraei; A. Jahanban-Esfahlan; M. Hejazi; F.

Oroojalian; B. Baradaran; M. Tohidast; M. d. l. Guardia; A. Mokhtarzadeh, *Talanta* **2022,** *243*, 123330. DOI https://doi.org/10.1016/j.talanta.2022.123330.

[37]S. I. Owen; C. T. Williams; G. Garrod; A. J. Fraser; S. Menzies; L. Baldwin; L. Brown; R. L. Byrne; A. M. Collins; A. I. Cubas-Atienzar; M. de Vos; T. Edwards; C. Escadafal; D. M. Ferreira; T. Fletcher; A. Hyder-Wright; G. A. Kay; K. Kontogianni; J. Mason; E. Mitsi; T. Planche; J. A. Sacks; J. Taylor; S. Todd; C. Tully; L. E. Cuevas; E. R. Adams, *J. Infect.* **2022,** *84* (3), 355-360. DOI https://doi.org/10.1016/j.jinf.2021.12.007.

[38]Q. Wang; Q. Du; B. Guo; D. Mu; X. Lu; Q. Ma; Y. Guo; L. Fang; B. Zhang; G. Zhang; X. Guo, *J. Clin. Microbiol.* **2020,** *58* (6), 10.1128/jcm.00375-20. DOI doi:10.1128/jcm.00375-20.

[39]Z. Zhang; P. Ma; R. Ahmed; J. Wang; D. Akin; F. Soto; B.-F. Liu; P. Li; U. Demirci, *Adv. Mater.* **2022,** *34* (1), 2103646. DOI https://doi.org/10.1002/adma.202103646.

[40]A. A. Patil; P. Kaushik; R. D. Jain; P. P. Dandekar, *ACS Infect. Dis.***2023,** *9* (1), 9-22. DOI 10.1021/acsinfecdis.2c00449.

[41]A. Shaheen; R. Arshad; A. Taj; U. Latif; S. Z. Bajwa, Biosensor Applications for Viral and Bacterial Disease Diagnosis. In *Nanobiosensors*, 2020; pp 117-148.

[42]F. Zhang; J. Liu, *Anal. Sens.* **2021,** *1* (1), 30-43. DOI https://doi.org/10.1002/anse.202000023.

[43]P. Moitra; M. Alafeef; K. Dighe; M. B. Frieman; D. Pan, *ACS Nano* **2020,** *14* (6), 7617-7627. DOI 10.1021/acsnano.0c03822.

[44]E. Cesewski; B. N. Johnson, *Biosens. Bioelectron.* **2020,** *159*, 112214. DOI

https://doi.org/10.1016/j.bios.2020.112214.

[45]J. Wu; H. Liu; W. Chen; B. Ma; H. Ju, *Nat. Rev. Bioeng.* **2023,** *1* (5), 346-360. DOI 10.1038/s44222-023-00032-w.

[46]C. H. Gayathri; P. Mayuri; K. Sankaran; A. S. Kumar, *Biosens. Bioelectron.* **2016,** *82*, 71-77. DOI https://doi.org/10.1016/j.bios.2016.03.062.

[47]M. Zhang; X. Li; J. Pan; Y. Zhang; L. Zhang; C. Wang; X. Yan; X. Liu; G. Lu, *Biosens. Bioelectron.* **2021,** *190*, 113421. DOI https://doi.org/10.1016/j.bios.2021.113421.

[48]H. Zhang; X. Ma; Y. Liu; N. Duan; S. Wu; Z. Wang; B. Xu, *Biosens. Bioelectron.* **2015,** *74*, 872-877. DOI https://doi.org/10.1016/j.bios.2015.07.033.

[49]H. Chen; S.-G. Park; N. Choi; J.-I. Moon; H. Dang; A. Das; S. Lee; D.-G. Kim; L. Chen; J. Choo, *Biosens. Bioelectron.* **2020,** *167*, 112496. DOI https://doi.org/10.1016/j.bios.2020.112496.

[50]J. Deng; S. Zhao; Y. Liu; C. Liu; J. Sun, *ACS Appl. Bio Mater.* **2021,** *4* (5), 3863-3879. DOI 10.1021/acsabm.0c01247.

[51]A. A. Ansari; V. K. Thakur; G. Chen, *Coord. Chem. Rev.* **2021,** *436*, 213821. DOI https://doi.org/10.1016/j.ccr.2021.213821.

[52]F. Auzel, *Chem. Rev.* **2004,** *104* (1), 139-174. DOI 10.1021/cr020357g.

[53]L. M. Wiesholler; F. Frenzel; B. Grauel; C. Würth; U. Resch-Genger; T. Hirsch, *Nanoscale* **2019,** *11* (28), 13440-13449. DOI 10.1039/C9NR03127H.

[54]F. Pini; L. Francés-Soriano; V. Andrigo; M. M. Natile; N. Hildebrandt, *ACS Nano* **2023,** *17* (5), 4971-4984. DOI 10.1021/acsnano.2c12523.

[55]J. Wu; J. Wu; W. Wei; Y. Zhang; Q. Chen, *Small* **2024,** *20* (29), 2311729. DOI https://doi.org/10.1002/smll.202311729.

[56]Y. Ma; M. Song; L. Li; X. Lao; Y. Liu; M.-c. Wong; M. Yang; H. Chen; J. Hao, *Biosens. Bioelectron.* **2024,** *243*, 115778. DOI https://doi.org/10.1016/j.bios.2023.115778.

[57]X. Lao; Y. Liu; L. Li; M. Song; Y. Ma; M. Yang; G. Chen; J. Hao, *Aggregate* **2024,** *5* (2), e448. DOI https://doi.org/10.1002/agt2.448.

[58]J. Chen; W. K. H. Ho; B. Yin; Q. Zhang; C. Li; J. Yan; Y. Huang; J. Hao; C. Yi; Y. Zhang; S. H. D. Wong; M. Yang, *Biosens. Bioelectron.* **2024,** *248*, 115969. DOI https://doi.org/10.1016/j.bios.2023.115969.

[59]G. Liu, *Chem. Soc. Rev.* **2015,** *44* (6), 1635-1652. DOI 10.1039/C4CS00187G.

[60]Q. Zhao; P. Du; X. Wang; M. Huang; L.-D. Sun; T. Wang; Z. Wang, *ACS Omega* **2021,** *6* (23), 15236-15245. DOI 10.1021/acsomega.1c01491.

[61]B. Jin; S. Wang; M. Lin; Y. Jin; S. Zhang; X. Cui; Y. Gong; A. Li; F. Xu; T. J. Lu, *Biosens. Bioelectron.* **2017,** *90*, 525-533. DOI https://doi.org/10.1016/j.bios.2016.10.029.

[62]L. Liu; H. Zhang; Z. Wang; D. Song, *Biosens. Bioelectron.* **2019,** *141*, 111403. DOI https://doi.org/10.1016/j.bios.2019.111403.

[63]P.-Y. Xu; R. Kumar Kankala; S.-B. Wang; A.-Z. Chen, *Ultrason. Sonochem.* **2023,** *100*, 106617. DOI https://doi.org/10.1016/j.ultsonch.2023.106617.

[64]S. Chen; B. Huang; J. Tian; W. Zhang, *Adv. Healthcare Mater.*, 2401211. DOI https://doi.org/10.1002/adhm.202401211.

[65] R. Kushwaha; R. Rai; V. Gawande; V. Singh; A. K. Yadav; B. Koch; P. Dhar; S. Banerjee, *ChemBioChem* **2024,** *25* (2), e202300652. DOI https://doi.org/10.1002/cbic.202300652.

[66] X. Qi; Y. Xiang; E. Cai; X. Ge; X. Chen; W. Zhang; Z. Li; J. Shen, *Coord. Chem. Rev.* **2023,** *496*, 215426. DOI https://doi.org/10.1016/j.ccr.2023.215426.

[67] H. Wang; Y. Wu; H. Zou; Z. Song; Y. Wang; H. Wang; M. Zhou, *ACS Appl. Nano Mater.* **2023,** *6* (6), 4834-4843. DOI 10.1021/acsanm.3c00509.

[68] W. Xie; J. Chen; X. Cheng; H. Feng; X. Zhang; Z. Zhu; S. Dong; Q. Wan; X. Pei; J. Wang, *Small* **2023,** *19* (14), 2205941. DOI https://doi.org/10.1002/smll.202205941.

[69] C. He; P. Feng; M. Hao; Y. Tang; X. Wu; W. Cui; J. Ma; C. Ke, *Adv. Funct. Mater.* **2024,** *34* (38), 2402588. DOI https://doi.org/10.1002/adfm.202402588.

[70] F. Yang; J. Lv; W. Ma; Y. Yang; X. Hu; Z. Yang, *Small*, 2402669. DOI https://doi.org/10.1002/smll.202402669.

[71] X. Wang; X. Zhong; F. Gong; Y. Chao; L. Cheng, *Mater. Horiz.* **2020,** *7* (8), 2028-2046. DOI 10.1039/D0MH00613K.

[72] G.-Y. Wan; Y. Liu; B.-W. Chen; Y.-Y. Liu; Y.-S. Wang; N. Zhang, *Cancer Biology and Medicine* **2016,** *13* (3), 325-338. DOI 10.20892/j.issn.2095-3941.2016.0068.

[73] X. Cao; M. Li; Q. Liu; J. Zhao; X. Lu; J. Wang, *Small* **2023,** *19* (42), 2303195. DOI https://doi.org/10.1002/smll.202303195.

[74] D. Li; Y. Yang; D. Li; J. Pan; C. Chu; G. Liu, *Small* **2021,** *17* (42), 2101976. DOI https://doi.org/10.1002/smll.202101976.

[75] X. Xing; S. Zhao; T. Xu; L. Huang; Y. Zhang; M. Lan; C. Lin; X. Zheng; P. Wang,

Coord. Chem. Rev. **2021,** *445*, 214087. DOI https://doi.org/10.1016/j.ccr.2021.214087.

[76]J. Shi; J. Li; Y. Wang; C. Y. Zhang, *Chem. Eng. J.* **2022,** *431*, 133714. DOI https://doi.org/10.1016/j.cej.2021.133714.

[77]Y. Wang; Y. Sun; S. Liu; L. Zhi; X. Wang, *Ultrason. Sonochem.* **2020,** *63*, 104968. DOI https://doi.org/10.1016/j.ultsonch.2020.104968.

[78]Y. Qian; J. Wang; X. Geng; B. Jia; L. Wang; Y.-Q. Li; B. Geng; W. Huang, *Adv. Healthcare Mater.* **2024,** *n/a* (n/a), 2400659. DOI https://doi.org/10.1002/adhm.202400659.

[79]Z. Weng; Y. Xu; J. Gao; X. Wang, *Biomater. Sci.* **2023,** *11* (1), 76-95. DOI 10.1039/D2BM01460B.

[80]D. He; W. Wang; N. Feng; Z. Zhang; D. Zhou; J. Zhang; H. Luo; Y. Li; X. Chen; J. Wu, *ACS Appl. Mater. Interfaces* **2023,** *15* (12), 15140-15151. DOI 10.1021/acsami.2c23113.

[81]T. Ding; F. Liu; H. Xin; Y. Chen; L. Kong; J. Han; D. Ma; Y. Han; L. Zhang, *Nano Today* **2024,** *54*, 102069. DOI https://doi.org/10.1016/j.nantod.2023.102069.

[82]M. Sun; J. Wang; X. Huang; R. Hang; P. Han; J. Guo; X. Yao; P. K. Chu; X. Zhang, *Biomaterials* **2024,** *307*, 122532. DOI https://doi.org/10.1016/j.biomaterials.2024.122532.

[83]S. Cheng; L. Chen; F. Gong; X. Yang; Z. Han; Y. Wang; J. Ge; X. Gao; Y. Li; X. Zhong; L. Wang; H. Lei; X. Zhou; Z. Zhang; L. Cheng, *Adv. Funct. Mater.* **2023,** *33* (22), 2212489. DOI https://doi.org/10.1002/adfm.202212489.

[84] C. Mao; W. Jin; Y. Xiang; Y. Zhu; J. Wu; X. Liu; S. Wu; Y. Zheng; K. M. C. Cheung; K. W. K. Yeung, *Adv. Mater.* **2023,** *35* (9), 2208681. DOI https://doi.org/10.1002/adma.202208681.

[85] C. Yan; H. Zhao; D. F. Perepichka; F. Rosei, *Small* **2016,** *12* (29), 3888-3907. DOI https://doi.org/10.1002/smll.201601565.

[86] J. Epp, 4 - X-ray diffraction (XRD) techniques for materials characterization. In *Materials Characterization Using Nondestructive Evaluation (NDE) Methods*, Hübschen, G.; Altpeter, I.; Tschuncky, R.; Herrmann, H.-G., Eds. Woodhead Publishing: 2016; pp 81-124.

[87] L. Yuan; W. Lin; K. Zheng; S. Zhu, *Acc. Chem. Res.* **2013,** *46* (7), 1462-1473. DOI 10.1021/ar300273v.

[88] J. Yao; M. Yang; Y. Duan, *Chem. Rev.* **2014,** *114* (12), 6130-6178. DOI 10.1021/cr200359p.

[89] E. Lerner; T. Cordes; A. Ingargiola; Y. Alhadid; S. Chung; X. Michalet; S. Weiss, *Science* **2018,** *359* (6373), eaan1133. DOI doi:10.1126/science.aan1133.

[90] N. Melnychuk; S. Egloff; A. Runser; A. Reisch; A. S. Klymchenko, *Angew. Chem. Int. Ed.* **2020,** *59* (17), 6811-6818. DOI https://doi.org/10.1002/anie.201913804.

[91] A. Kaur; S. Dhakal, *TrAC, Trends. Anal. Chem.* **2020,** *123*, 115777. DOI https://doi.org/10.1016/j.trac.2019.115777.

[92] J. Guo; C. Mingoes; X. Qiu; N. Hildebrandt, *Anal. Chem.* **2019,** *91* (4), 3101-3109. DOI 10.1021/acs.analchem.8b05600.

[93] F. Wang; Y. Han; C. S. Lim; Y. Lu; J. Wang; J. Xu; H. Chen; C. Zhang; M. Hong;

X. Liu, *Nature* **2010,** *463* (7284), 1061-1065. DOI 10.1038/nature08777.

[94] J. F.-C. Loo; Y.-H. Chien; F. Yin; S.-K. Kong; H.-P. Ho; K.-T. Yong, *Coord. Chem. Rev.* **2019,** *400*, 213042. DOI https://doi.org/10.1016/j.ccr.2019.213042.

[95] Q. Liu; B. Wu; M. Li; Y. Huang; L. Li, *Adv. Sci.* **2022,** *9* (3), 2103911. DOI https://doi.org/10.1002/advs.202103911.

[96] S. Borse; R. Rafique; Z. V. P. Murthy; T. J. Park; S. K. Kailasa, *Analyst* **2022,** *147* (14), 3155-3179. DOI 10.1039/D1AN02170B.

[97] C. Severi; N. Melnychuk; A. S. Klymchenko, *Biosens. Bioelectron.* **2020,** *168*, 112515. DOI https://doi.org/10.1016/j.bios.2020.112515.

[98] Z. Li; S. Lu; X. Li; Z. Chen; X. Chen, *Adv. Opt. Mater.* **2023,** *11* (11), 2202386. DOI https://doi.org/10.1002/adom.202202386.

[99] S. Bhuckory; S. Lahtinen; N. Höysniemi; J. Guo; X. Qiu; T. Soukka; N. Hildebrandt, *Nano Lett.* **2023,** *23* (6), 2253-2261. DOI 10.1021/acs.nanolett.2c04899.

[100] K. Nejati; M. Dadashpour; T. Gharibi; H. Mellatyar; A. Akbarzadeh, *J. Cluster Sci.* **2022,** *33* (1), 1-16. DOI 10.1007/s10876-020-01955-9.

[101] Y. Ma; M. Song; L. Li; X. Lao; M.-C. Wong; J. Hao, *Exploration* **2022,** *2* (6), 20210216. DOI https://doi.org/10.1002/EXP.20210216.

[102] P. C. Ray; G. K. Darbha; A. Ray; J. Walker; W. Hardy, *Plasmonics* **2007,** *2* (4), 173-183. DOI 10.1007/s11468-007-9036-9.

[103] M. R. Jones; K. D. Osberg; R. J. Macfarlane; M. R. Langille; C. A. Mirkin, *Chem. Rev.* **2011,** *111* (6), 3736-3827. DOI 10.1021/cr1004452.

[104] M. Li; S. K. Cushing; N. Wu, *Analyst* **2015,** *140* (2), 386-406. DOI

10.1039/C4AN01079E.

[105] S. Hou; Y. Chen; D. Lu; Q. Xiong; Y. Lim; H. Duan, *Adv. Mat.* **2020,** *32* (8), 1906475. DOI https://doi.org/10.1002/adma.201906475.

[106] T. Zhao; T. Li; Y. Liu, *Nanoscale* **2017,** *9* (28), 9841-9847. DOI 10.1039/C7NR01562C.

[107] F. Wang; R. Deng; X. Liu, *Nat. Protoc.* **2014,** *9* (7), 1634-1644. DOI 10.1038/nprot.2014.111.

[108] J. Piella; N. G. Bastús; V. Puntes, *Chem. Mater.* **2016,** *28* (4), 1066-1075. DOI 10.1021/acs.chemmater.5b04406.

[109] X. Zhang; M. R. Servos; J. Liu, *J. Am. Chem. Soc.* **2012,** *134* (17), 7266-7269. DOI 10.1021/ja3014055.

[110] D. Kim; J. Y. Lee; J. S. Yang; J. W. Kim; V. N. Kim; H. Chang, *Cell* **2020,** *181* (4), 914-921.e10. DOI 10.1016/j.cell.2020.04.011.

[111] A. Wu; Y. Peng; B. Huang; X. Ding; X. Wang; P. Niu; J. Meng; Z. Zhu; Z. Zhang; J. Wang; J. Sheng; L. Quan; Z. Xia; W. Tan; G. Cheng; T. Jiang, *Cell Host Microbe* **2020,** *27* (3), 325-328. DOI 10.1016/j.chom.2020.02.001.

[112] L. Mattsson; K. D. Wegner; N. Hildebrandt; T. Soukka, *RSC Adv.* **2015,** *5* (18), 13270-13277. DOI 10.1039/C5RA00397K.

[113] B. Wu; Z. Cao; Q. Zhang; G. Wang, *Sensors Actuators B: Chem.* **2018,** *255*, 2853-2860. DOI https://doi.org/10.1016/j.snb.2017.09.103.

[114] Z. Liu; C. Shang; H. Ma; M. You, *Nanotechnology* **2020,** *31* (23), 235501. DOI 10.1088/1361-6528/ab776d.

[115] L. Francés-Soriano; N. Estebanez; J. Pérez-Prieto; N. Hildebrandt, *Adv. Funct. Mater.* **2022,** *32* (37), 2201541. DOI https://doi.org/10.1002/adfm.202201541.

[116] M. Wu; X. Wang; K. Wang; Z. Guo, *Chem. Commun.* **2016,** *52* (54), 8377-8380. DOI 10.1039/C6CC02674E.

[117] M.-K. Tsang; W. Ye; G. Wang; J. Li; M. Yang; J. Hao, *ACS Nano* **2016,** *10* (1), 598-605. DOI 10.1021/acsnano.5b05622.

[118] M. Song; M.-C. Wong; L. Li; F. Guo; Y. Liu; Y. Ma; X. Lao; P. Wang; H. Chen; M. Yang; J. Hao, *Biosens. Bioelectron.* **2023,** *222*, 114987. DOI https://doi.org/10.1016/j.bios.2022.114987.

[119] J. Dong; W. Gao; Q. Han; Y. Wang; J. Qi; X. Yan; M. Sun, *Rev. Phys.* **2019,** *4*, 100026. DOI https://doi.org/10.1016/j.revip.2018.100026.

[120] W. Park; D. Lu; S. Ahn, *Chem. Soc. Rev.* **2015,** *44* (10), 2940-2962. DOI 10.1039/C5CS00050E.

[121] D. Lu; S. K. Cho; S. Ahn; L. Brun; C. J. Summers; W. Park, *ACS Nano* **2014,** *8* (8), 7780-7792. DOI 10.1021/nn5011254.

[122] C. Clarke; D. Liu; F. Wang; Y. Liu; C. Chen; C. Ton-That; X. Xu; D. Jin, *Nanoscale* **2018,** *10* (14), 6270-6276. DOI 10.1039/C7NR08979A.

[123] Z. Qi; Q. Wang; Y. Zhai; J. Xu; Z. Tao; Y. Tu; W. Lei; J. Xia, *J. Phys. D: Appl. Phys.* **2016,** *49* (23), 235103. DOI 10.1088/0022-3727/49/23/235103.

[124] M. L.-Viger; D. Brouard; D. Boudreau, *J. Phys. Chem. C* **2011,** *115* (7), 2974-2981. DOI 10.1021/jp109993a.

[125] A. M. Kotulska; A. Pilch-Wróbel; S. Lahtinen; T. Soukka; A. Bednarkiewicz,

Light Sci. Appl. **2022,** *11* (1), 256. DOI 10.1038/s41377-022-00946-x.

[126] M. Lunz; V. A. Gerard; Y. K. Gun'ko; V. Lesnyak; N. Gaponik; A. S. Susha; A. L. Rogach; A. L. Bradley, *Nano Lett.* **2011,** *11* (8), 3341-3345. DOI 10.1021/nl201714y.

[127] H. Zong; X. Wang; X. Mu; J. Wang; M. Sun, *Chem. Rec.* **2019,** *19* (5), 818-842. DOI https://doi.org/10.1002/tcr.201800181.

[128] C. Deusenbery; Y. Wang; A. Shukla, *ACS Infect. Dis.* **2021,** *7* (4), 695-720. DOI 10.1021/acsinfecdis.0c00890.

[129] R. Canaparo; F. Foglietta; N. Barbero; L. Serpe, *Adv. Drug Del. Rev.* **2022,** *189*, 114495. DOI https://doi.org/10.1016/j.addr.2022.114495.

[130] R. Wang; Q. Liu; A. Gao; N. Tang; Q. Zhang; A. Zhang; D. Cui, *Nanoscale* **2022,** *14* (36), 12999-13017. DOI 10.1039/D2NR01847K.

[131] Z. Zhou; T. Wang; T. Hu; H. Xu; L. Cui; B. Xue; X. Zhao; X. Pan; S. Yu; H. Li; Y. Qin; J. Zhang; L. Ma; R. Liang; C. Tan, *Adv. Mat.* **2024,** *36* (23), 2311002. DOI https://doi.org/10.1002/adma.202311002.

[132] Y. Zhou; Y. Zhang; M. Lin; J. Long; Z. Zhang; H. Lin; J. C. S. Wu; X. Wang, *Nat. Commun.* **2015,** *6* (1), 8340. DOI 10.1038/ncomms9340.

[133] A. Tiwari; S. Udainiya; A. Dubey; V. Agrawal, Chapter 4 - Parasites in the integumentary system. In *Organ-Specific Parasitic Diseases of Dogs and Cats*, Rana, T., Ed. Academic Press: 2023; pp 89-111.

[134] B. Hawthorne; J. K. Simmons; B. Stuart; R. Tung; D. S. Zamierowski; A. J. Mellott, *J. Biomed. Mater. Res. B Appl. Biomater.* **2021,** *109* (12), 1967-1985. DOI

10.1002/jbm.b.34861.

[135] G. Kaur; G. Narayanan; D. Garg; A. Sachdev; I. Matai, *ACS Applied Bio. Mat.* **2022,** *5* (5), 2069-2106. DOI 10.1021/acsabm.2c00035.

[136] F. Piraino; Š. Selimović, *Biomed Res. Int.* **2015,** *2015* (1), 403801. DOI https://doi.org/10.1155/2015/403801.

[137] L. N. Kasiewicz; K. A. Whitehead, *Biomater. Sci.* **2017,** *5* (10), 1962-1975. DOI 10.1039/C7BM00264E.

[138] S. Sun; X. Meng; J. Xu; Z. Yang; X. Zhang; H. Dong, *Nano Today* **2024,** *55*, 102181. DOI https://doi.org/10.1016/j.nantod.2024.102181.

[139] J. Zhou; X. Ji; H. Wang; J. C. Hsu; C. Hua; X. Yang; Z. Liu; H. Guo; Y. Huang; Y. Li; W. Cai; X. Lin; D. Ni, *Nano Lett.* **2024,** *24* (26), 7868-7878. DOI 10.1021/acs.nanolett.4c00930.

[140] M. Wu; Z. Zhang; Z. Liu; J. Zhang; Y. Zhang; Y. Ding; T. Huang; D. Xiang; Z. Wang; Y. Dai; X. Wan; S. Wang; H. Qian; Q. Sun; L. Li, *Nano Today* **2021,** *37*, 101104. DOI https://doi.org/10.1016/j.nantod.2021.101104.

[141] Z. Zhu; X. Gou; L. Liu; T. Xia; J. Wang; Y. Zhang; C. Huang; W. Zhi; R. Wang; X. Li; S. Luo, *Acta Biomater.* **2023,** *157*, 566-577. DOI https://doi.org/10.1016/j.actbio.2022.11.061.

[142] Z. Yang; R. Huang; B. Zheng; W. Guo; C. Li; W. He; Y. Wei; Y. Du; H. Wang; D. Wu; H. Wang, *Adv. Sci.* **2021,** *8* (8), 2003627. DOI https://doi.org/10.1002/advs.202003627.

[143] X. Zhao; H. Wu; B. Guo; R. Dong; Y. Qiu; P. X. Ma, *Biomaterials* **2017,** *122*,

34-47. DOI https://doi.org/10.1016/j.biomaterials.2017.01.011.

[144] J. Qu; X. Zhao; Y. Liang; T. Zhang; P. X. Ma; B. Guo, *Biomaterials* **2018,** *183*, 185-199. DOI https://doi.org/10.1016/j.biomaterials.2018.08.044.

[145] L. Qiao; Y. Liang; J. Chen; Y. Huang; S. A. Alsareii; A. M. Alamri; F. A. Harraz; B. Guo, *Bioact. Mater.* **2023,** *30*, 129-141. DOI https://doi.org/10.1016/j.bioactmat.2023.07.015.

[146] W.-C. Huang; R. Ying; W. Wang; Y. Guo; Y. He; X. Mo; C. Xue; X. Mao, *Adv. Funct. Mater.* **2020,** *30* (21), 2000644. DOI https://doi.org/10.1002/adfm.202000644.